Title

Application of a Mobile Electrodynamic Balance for Studying Water Diffusion in Single Charged Aerosol

Author

Nadler, Katherine Adele

Publication Date

2018

Peer reviewed|Thesis/dissertation

UNIVERSITY OF CALIFORNIA SAN DIEGO

Application of a Mobile Electrodynamic Balance for Studying Water Diffusion in Single Charged Aerosol

A dissertation submitted in partial satisfaction of the
requirements for the degree of Doctor of Philosophy

in

Chemistry

by

Katherine Adele Nadler

Committee in charge:

Professor Robert Continetti, Chair
Professor Michael Galperin
Professor Elizabeth Komives
Professor Joel Norris
Professor Francesco Paesani

2018

The Dissertation of Katherine Adele Nadler is approved, and it is acceptable in quality and form for publication on microfilm and electronically:

_____

_____

_____

_____

_____
Chair

University of California San Diego

2018

DEDICATION

to my parents, Bob and Evelyn Nadler,

for always encouraging me to pursue my passions

and for instilling in me the values of happiness, joy, and love

to my sister, Genevieve,

for providing guidance and being an amazing role model

to my brother, Mark,

for always being proud of me

to my husband, Gabriele,

for pushing me to work hard but make time for fun

and not letting me give up

and to my family and friends

who have continued to encourage me, celebrate with me, and motivate me

EPIGRAPH

Here's to strong women.
May we know them.
May we be them.
May we raise them.

~Unknown

TABLE OF CONTENTS

LIST OF FIGURES

LIST OF TABLES

ACKNOWLEDGEMENTS

I would like to acknowledge Professor Robert Continetti for his continuous support as the chair of my committee. His guidance through the process of designing, building, and modifying the instrument and experimental procedure has been invaluable. I am greatly appreciative of the knowledge I have absorbed during my time in his laboratory. I am also thankful to the members of the Continetti lab for all of the great memories and learning moments including Ben Shen, Amelia Ray, Joel Rivera, Rico Otto, Yanice Benitez, and Katharine Lunny. I've especially enjoyed watching Morgan Miller develop over the years as a scientist and as a leader. My summer undergraduate, Joe Rempel, gave me great hope in the next generation of scientists with his inquisitive nature and careful attention to detail. I am grateful that Pyeongeun Kim will continue the work on MobQIT, knowing the machine will be fussy and likely cause some headache. Finally, to Joseph Taulane, who keeps us all moving forward on projects and has taught me how pay careful attention to the small, yet important, details.

Next, I would like to thank the officers of SWIGS, particularly Melissa Clark and Jessie Moreton who were outstanding presidents and make me proud to have had a part in developing the organization to what it is today. Through SWIGS I was able to explore my career curiosities and become a better public speaker. I owe a large part of my success in public speaking, resumes and interviews to the workshops and speakers hosted and co-hosted through SWIGS.

The UCSD cycling team and San Diego cycling community have become a huge part of my life over the last three years, and I could not have made it to the end of my PhD without the large number of scientist and doctorate friends who have been role models in various ways. Particularly Esther Walker, Kat Ellis, Lillian McCormick, and Alex Reich were part of the super-fast girls squad who helped spark my love of competitive cycling, and all of them have been examples of independent, intelligent, and confident women. There are many other former and current members of the cycling community who have fostered an inclusive and healthy community and provided a fun outlet during grad school.

I am grateful to my group of scientist girl-friends with whom many wine bottles have been drunk, including but not limited to Jamie Schiffer, Lydia Hernandez, Olivia Ryder, and Liora Mael. We manage to be both huge supporters and constructive critics for one another, which I believe is a crucial part of succeeding as a woman in science.

I would like to thank Gabriele Canzi for his endless support through the years. We have already experienced quite a number challenges through years of long-distance, the passing of important family members, and the stress of two PhD defenses. But we manage to make time for incredible trips, riding bicycles, and pulled off one of the best weddings ever! I'm appreciative of our shared love of sports and desire to socialize in a scientist sort-of way. I have received an immeasurable amount of advice that has directly impacted my success in school and beyond, and I am looking forward to this next chapter of our lives.

My sister, Genny, has also been a source of incredible support from her optimistic attitude and propensity to put the needs of others before her own. She is always willing to take time for a Facetime or phone call and catch up on the newest life events, and been an enormous source of support with wedding planning and general life advice. I wish that my brother, Mark, was still around to share in this time of celebration. One of his gifts was finding any excuse to party and even though he had no clue what I was working on, he would have been the first to congratulate. We all miss him every single day.

Finally, I would like to thank my parents for the enduring support during the most challenging times of my life so far. Not being scientists themselves, they often provided the much-needed outside perspective as a reminder of my big picture motivations. I attribute my passion for communicating science to the public to their curiosity of understanding my research; I've tested numerous versions of my "elevator speech" at family gatherings, tweaking it a bit for effectiveness. My parents never cease to show how proud they are, from getting excited with me even when they don't quite understand the source of excitement, and also as my never-ending sounding board during times of frustration. They have somehow mastered how to show support from the other side of the country during some of the greatest moments during graduate school, and for that I will be eternally grateful. As a family, we have withstood one of the most tragic of losses with the unexpected passing of my younger brother, but my parents have still managed to display each day what it means to be a family.

CHAPTER SPECIFIC ACKNOWLEDGEMENTS

Chapter 3, in full, has been submitted for publication of the material as it may appear in Physical Chemistry Chemistry Physics, 2018, Nadler, Katherine A.; Huang, Dao-Ling; Kim, Pyeongeun; Xiong, Wei; Continetti, Robert E. The dissertation author was the primary investigator and author of this paper.

Chapter 4, in part, is currently being prepared for publication of the material. Nadler, Katherine A.; Kim, Pyeongeun; Continetti, Robert E. The dissertation author was the primary investigator and author of this paper.

VITA

2012	Bachelor of Arts, Maryville College
2014	Master of Science, University of California San Diego
2018	Doctor of Philosophy, University of California San Diego

ABSTRACT OF THE DISSERTATION

Application of a Mobile Electrodynamic Balance for Studying Water Diffusion in Single Charged Aerosol

by

Katherine Adele Nadler

Doctor of Philosophy in Chemistry

University of California San Diego, 2018

Professor Robert E. Continetti, Chair

Aerosols are ubiquitous in the atmosphere and play a major role in balancing the incoming solar radiation directly through scattering and absorption, and indirectly by acting as seeds to nucleate clouds. The ability of an aerosol to uptake water is

fundamental to the condensational growth necessary for cloud formation, and additionally alters aerosol properties such as concentration, density, refractive index, and viscosity. The growth rate under particular relative humidity is dependent on the mobility of water molecules in the aerosol, reported as the water diffusion coefficient, and becomes extremely slow at high viscosity.

Ocean-derived sea spray aerosol (SSA) is one of the most abundant natural sources of atmospheric aerosol and exhibits complex chemical composition. SSA contains both inorganic and organic compounds, including inorganic salts (NaCl and $CaCl_2$) and saccharides. A number of recent studies revealed that model SSA organic compounds can achieve high-viscosity, semi-solid phase states at low humidity. The relationship between viscosity and diffusion based on the Stokes-Einstein (S-E) relation is used to estimate water diffusion coefficients in aerosol because of the supersaturated concentrations not accessible to bulk diffusion techniques. However, the S-E relation has been shown to under-predict water mobility by several orders of magnitude using recently developed single aerosol diffusion techniques. Only a few methods currently exist for measuring diffusion in single aerosol, limiting the database of concentration-dependent water diffusion coefficients necessary for improving the parameterization between viscosity and diffusion. In this thesis, a new method is presented for directly measuring the diffusion coefficient of water that applies the Raman spectroscopic isotope tracing method to single, charged viscous aerosols trapped in a newly built electrodynamic balance (EDB) under controlled humidity. The EDB Raman isotope

tracing method is validated by comparing results of the concentration-dependent water diffusion coefficient using sucrose as a model system. We then apply the method to directly measure the water diffusion coefficient in ternary sucrose-NaCl and sucrose-$CaCl_2$ mixtures for the first time, and model the results with a Vignes-type diffusion model. Further application of the EDB isotope tracing method will continue to clarify the role of chemical composition on aerosol physical properties.

CHAPTER 1: Introduction to Aerosols and Water Diffusion

1.1 Introduction to atmospheric aerosols

Atmospheric aerosols are liquid or solid particles ranging in size from 10 nm to 100 μm which are suspended in the air. Aerosols are emitted from a variety of sources such as volcanic eruptions,[1,2] biomass and fossil fuel combustion,[3–6] dust storms,[7–10] and ocean sea spray from bubble bursting mechanisms.[11,12] They are also formed through the nucleation of low volatility gas phase species, termed gas-to-particle conversion, which is often a result of photochemical and oxidation reactions with atmospheric gases.[13]

Once aerosols are emitted or formed in the atmosphere, they behave as microscopic chemical reactors, interacting with the surroundings and undergoing chemical and physical transformations over their lifetime.[14] For example, interactions with water vapor lead to condensational growth, evaporation, and moisture-induced phase changes called efflorescence and deliquescence. These physical transformations alter properties such as size, morphology,[15,16] as well as density and viscosity.[17,18] Reactions with reactive trace gases such as O_3, OH, and NO_x species can alter the chemical composition of the aerosol, which subsequently impacts its physical properties and lifetime.[19–22] This dissertation presents work which aims to better understand the

fundamental physicochemical properties of ~~aerosols~~ using model systems to examine the behavior under atmospherically-relevant humidity and temperature conditions.

Aerosols impact the radiative budget of the atmosphere by directly and indirectly interacting with incoming solar radiation. The balance between absorption of solar radiation and scattering influences the radiation budget, where a positive forcing is a net heating and a negative forcing is defined as net cooling.[23] For example, black carbon aerosols strongly absorb sunlight which leads to a positive forcing on the atmosphere.[5,6] However, aerosols also behave as cloud condensation nuclei, CCN, by providing a surface for water vapor to condense and activate into cloud droplets.[24,25] Depending on the number and size distribution of the droplets, as well as the phase (liquid, ice, or mixed), the cloud may have either a net positive or negative forcing.[26,27] Clouds composed of small water droplets are more optically reflective and therefore have a net cooling effect.[28] The accuracy in predicting the contributors of radiative forcing relies on the understanding of a number of atmospheric prcocesses, including cloud formation and precipitation which can be described using global climate models.[29–31] An analysis of the largest parameterization uncertainties in a global 3-D aerosol microphysics model shows that emissions-related parameters dominate the uncertainty in regions near aerosol sources, and in remote locations the aerosol microphysical properties are responsible for large uncertainty.[30] Improving the accuracy of global climate models requires a deep understanding of aerosol microphysical properties.[32–34]

One such property is the ability of an aerosol to absorb water described as hygroscopicity, where aerosols with a higher capacity to absorb water are termed *hygroscopic.*[35] Aerosol hygroscopic growth directly impacts the size, refractive index, and viscosity under given environmental conditions, with subsequent implications on cloud formation and droplet size distributions, which as mentioned earlier have enormous climate implications.[24] There is a strong correlation between the size of an aerosol and its capability to act as a CCN, or CCN activity, where the range between 80-150 nm are the most efficient. Numerous studies have investigated the CCN activity of ambient aerosols during field campaigns in forested regions, industrial areas, and over the remote ocean,[36,37] which provide direct measurements that are used to train aerosol models. Developments in aerosol analytical instrumentation have not only revealed the variation of size distributions, which can be used to predict CCN and cloud activity, but also the chemical composition.[38–41]

Aerosols are composed of a wide range of chemical compounds including inorganic and organic components. Inorganic compounds such as nitrates and sulfates, have been studied extensively due to their abundance in the troposphere sourced from fossil fuel combustion, coal emissions, and volcanic eruptions.[42–46] The response of inorganic salts to water vapor is characterized by deliquescence and efflorescence phase transitions, which are dependent on the solubility of the salt.[15,16,47] Organic components, on the other hand, generally exhibit continuous and reversible growth as a function of relative humidity. The extent of hygroscopic growth in binary mixtures of organics and

water varies widely, with large impacts due to the carbon chain length, saturation ratio, and branching.[25,43,46,48–54] Mixtures of organic and inorganic components exhibit a range of hygroscopic responses dependent on the molecular ratios of components and chemical identity.

Sea spray aerosol (SSA), produced *via* bubble bursting and wave breaking mechanisms in the ocean as shown in Figure 1.1, are one of the most abundant types of natural aerosols by mass in the atmosphere.[55] For a long time SSA was assumed to consist mostly of sea salt, which contains inorganic ions of sodium, calcium, magnesium, potassium, chlorine and other trace ions.[7,41,56–58] However, advances in field instrumentation have recently begun to unveil the chemical complexity of individual SSA, particularly the particle-to-particle variability which can not be captured using traditional filtration-based, mass loading techniques.[11,41,59] These efforts have challenged the traditional paradigm by showing that SSA contain mixtures of inorganic salts with organic matter and particulate biological material.[41,60,61] Field measurements conducted in remote marine regions suggest the organic fraction consists of insoluble, oxygen-rich species, and spectroscopy evidence show features characteristic of saccharides,[62] carboxylic acids,[62] and alkanes.[63] As mentioned previously, aerosols emitted into the atmosphere may undergo reactions changing their physical and chemical characteristics from the time of their original production even by trace amounts of reactive gases present in remote areas. In order to definitively measure nascent SSA from real seawater in the absence of pollutants, an enclosed wave channel equipped with a mechanical wave

breaking mechanism was employed to simulate a phytoplankton bloom cycle in a pristine marine environment. For the first time, nascent SSA were chemically analyzed during two controlled phytoplankton blooms which led to a new understanding of the size-resolved chemical complexity on a single-particle level as a function of seawater biology.[41] The SSA were found to contain a variety of organic species including a large fraction of mono and dicarboxylic acids of C_4 – C_{18} chain lengths, mono and polysaccharides, and siliceous material following cycles of phytoplankton growth and decay and the digestion of lipids and cellular material from heterotrophic bacteria.[59,64,65]

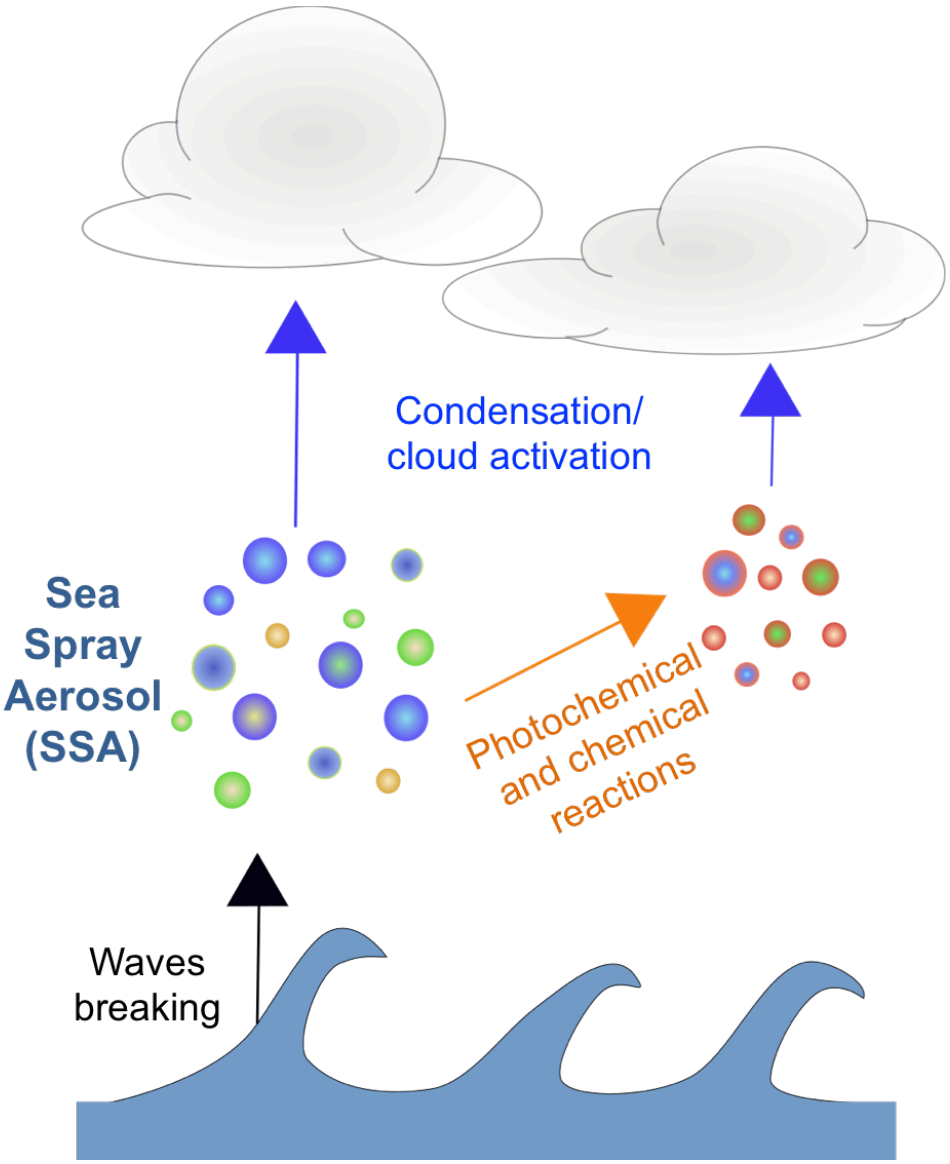

Figure 1.1. Sea spray aerosol are produced from ocean waves breaking and undergo transformations, such as photochemical and chemical aging, condensational growth and evaporation, and cloud activation, which affect their impacts on the climate.

As research efforts have continued to identify the specific molecules present in real SSA with varying seasons, location, and sea water chemistry, there has also been a

large push to study simplified proxies to SSA in the laboratory under a controlled environment.[32,55] During the contained phytoplankton bloom experiments, it was found that the average hygroscopicity of SSA changed over the course of a bloom,[11] however unavoidable gaps in our understanding of the specific contributions to this behavior remain due to the extreme complexity of the aerosols. Laboratory studies on model systems enable us to bridge the gap, and achieve an accurate representation the hygroscopic response, ice nucleating activity, and heterogeneous reactivity which is applied to more complex, realistic aerosols. Monitoring the response of an aerosol to external conditions, such as temperature and gas phase composition, can lead to a better understanding of the physicochemical properties of aerosols in phase states not accessible in the bulk.[66]

The equilibration size of an aerosol to changes in humidity is described by Köhler theory based on the combination of solute interactions, described by Raoult's law, and surface tension and curvature, expressed as the Kelvin term.[67] The theory predicts the change in size of an aerosol in the presence of a given RH as water vapor evaporates or condenses to establish equilibrium. The solute interactions can be predicted using thermodynamic models, which are trained using experimental data. These models include the Extended Aerosol Inorganic Model (E-AIM),[68,69] the Aerosol Inorganic-Organic Mixtures Functional groups Activity Coefficients (AIOMFAC),[44,70] and UmanSysProp.[71] Shown in Figure 1.2 are treatments for the mass fraction of sodium chloride with water activity, and in Figure 1.3 is a comparison of thermodynamic treatments for the mass

fraction solute with water activity for sucrose compared with empirical parameterizations. The models incorporate activity coefficients that account for nonideal interactions which are not accounted for in simple additivity models such as the Zandovii-Stokes relation.[72] Experimental data are used to inform models, such as the molecular composition to be incorporated, and motivate re-parameterizations, for example AIOMFAC to include semi-empirical parameterizations of inorganic-organic interactions, to improve agreement.[70,73] The accuracy has dramatically improved in well-studied systems, and shows promising results when applied as predictive theoretical tools when experimental data is lacking because of the versatility of functional group analysis. An advantage of the accuracy of the models to predict the equilibrium size for a variety of binary and ternary chemical systems is the application for studying a variety of other properties such as density, refractive index, and viscosity.[74]

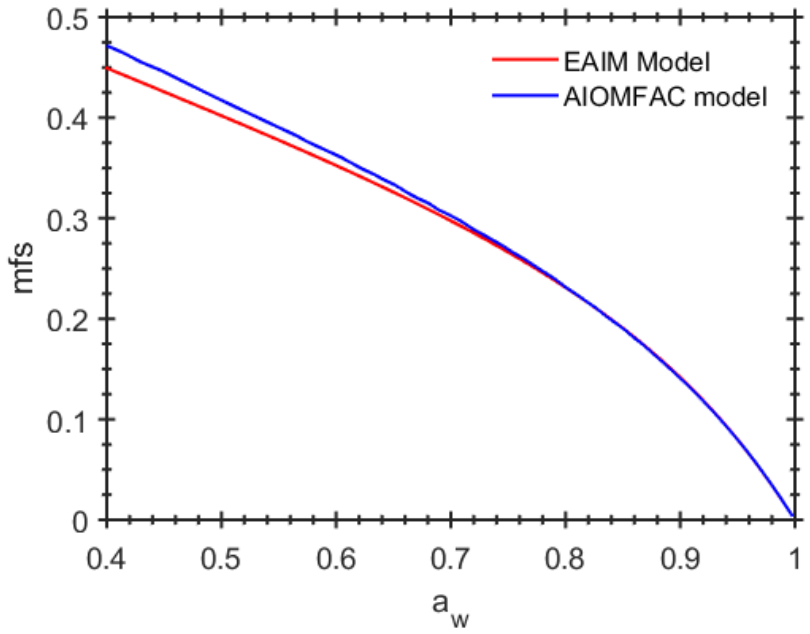

Figure 1.2. Comparison of thermodynamic models for parameterizing the mass fraction solute (mfs) of NaCl with water activity.

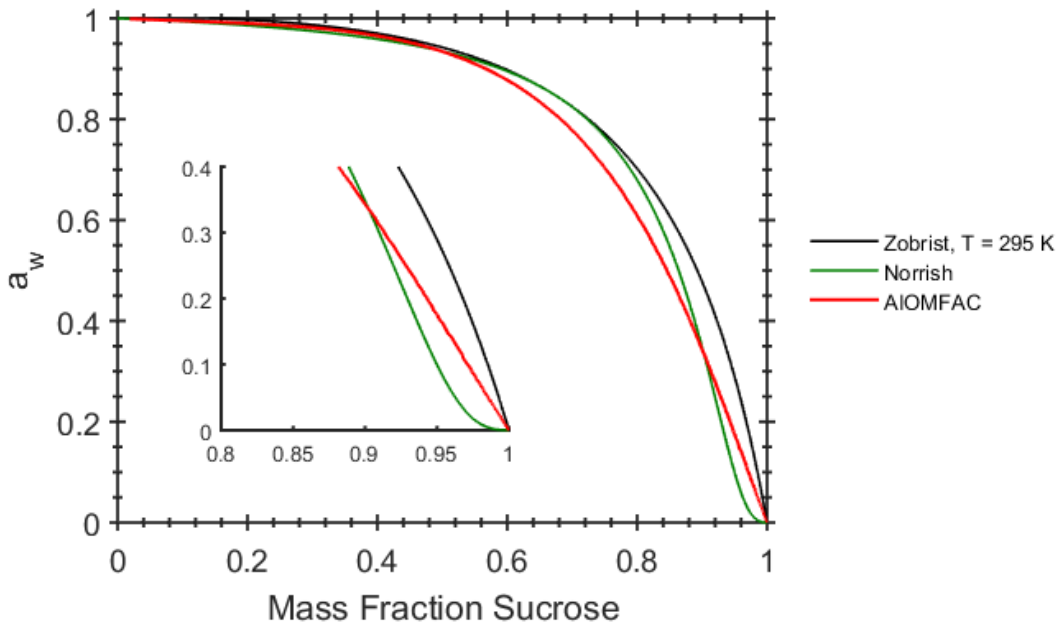

Figure 1.3. Treatments for the dependence of water activity on the mass fraction solute of sucrose for the empirical Zobrist *et al.*[75] parameterization, Norrish,[76] and thermodynamic treatment of AIOMFAC.[70]

1.2 The impacts of high viscosity in aerosol

The viscosity of an aerosol is directly related to its atmospheric effects, such as light scattering, absorption efficiency, and CCN efficiency. Low viscosity, liquid-like aerosols quickly respond to changes in RH and gas-phase composition, as indicated in Figure 1.4.[34,77,78] High viscosity organic aerosols, however, display slow kinetics to changes in RH and gas-phase oxidants at low temperatures and in dry environments.[77,79,80] The relationship between viscosity and water content, dictated by

RH, has been confirmed experimentally[79,81,82] where a higher amount of water in an aerosol correlates to lower viscosity.

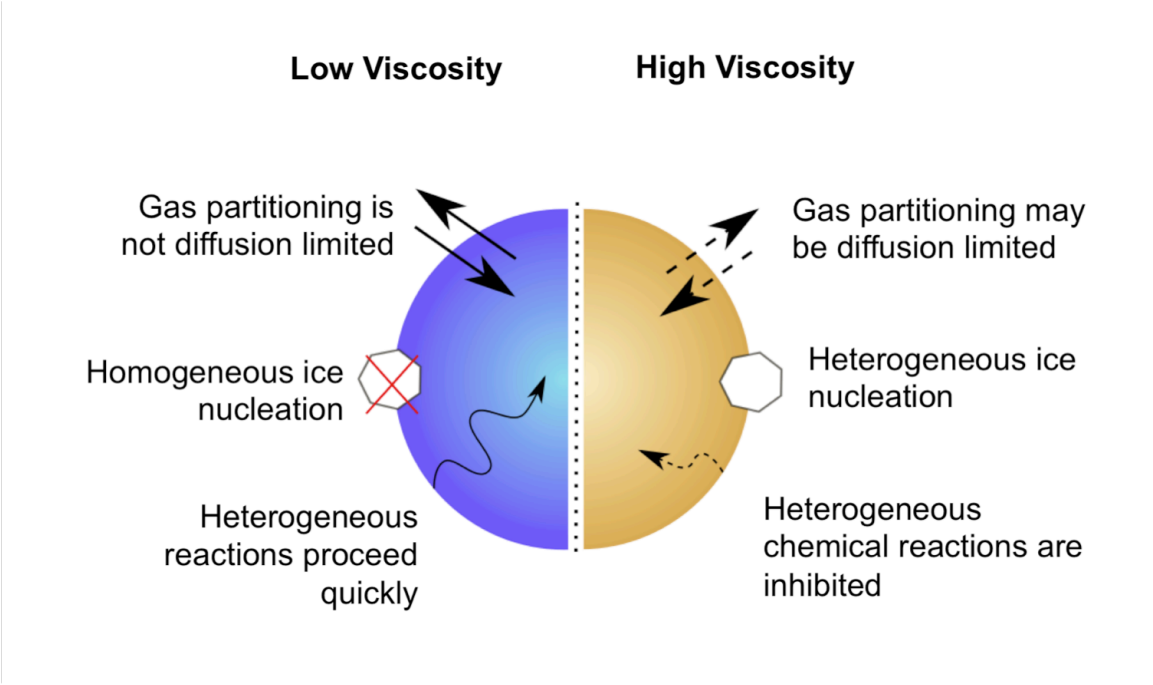

Figure 1.4. Schematic describing the differences in gas partitioning, ice nucleation activity, and heterogeneous reaction kinetics for low viscosity compared to high viscosity aerosols.

The ability of organic aerosols to reversibly uptake water even at reduced RH without crystallization led to the assumption that they existed in a low viscosity state.[83] It was discovered during laboratory experiments that model organic aerosols achieve ultra-viscous or glassy states at atmospherically relevant temperatures and RH.[83] This

propelled the development of techniques, both in the field and laboratory, to measure the viscosity of single aerosol. Subsequent observations in the boreal forest revealed that 40 – 100 nm biogenic organic aerosol exhibited a high bounce fraction when impacted on a surface, consistent with a viscosity significantly higher than that of liquid-like aerosols. The bounce factor measurements were confirmed using secondary organic aerosol surrogate molecules in the laboratory which displayed similar high-rebound fractions at low RH.

The revelation that organic and mixed-organic aerosols can exist in high viscosity phases has led to a number of experimental and theoretical developments. The conventional method to measure viscosity is using a viscometer or rheometer[84] which can measure 10^{-3} – 10^{8} Pa·s however large volumes of sample are required, and high solute concentrations beyond the solubility limit can not be accessed.[33] A few of the most widely used experimental techniques for probing aerosol viscosity are explained briefly. In the poke flow method,[17,18,85] aerosols of 20 – 50 μm diameter are deposited on a hydrophobic-coated substrate contained in an environmental cell through which an RH-controlled air stream flows. Microscope images are collected over time as the aerosol is mechanically deformed using a sharp needle, and the relaxation time back to the equilibrium shape is measured to infer viscosity. An alternative method examines the coalescence of two aerosol particles contained in holographic optical tweezers under controlled RH conditions. The elastic backscattered light is used to determine the time at which the coalesced droplets relax into a single, spherical droplet where fast relaxation

times correlate to low viscosity. Optical tweezers coalescence measurements have been used extensively to study binary aqueous and ternary organic-organic and inorganic-organic model systems over the viscosity range 10^{-3} – 10^{9} Pa·s.[86–88] A third method for measuring viscosity is to measure the particle rebound fraction as a function of RH.[83,89] Liquid-like, low viscosity aerosols lose energy through deformation when impacted on a surface, resulting in a low fraction of aerosols rebounding from the surface. High viscosity aerosols exhibit high bounce fractions as a result of retaining the kinetic energy post-impact. The method is applied to smaller aerosols, below 1 μm, and has been demonstrated in field studies.[89,90] The various experimental and analytical techniques used in these methods highlights the need to use complementary techniques to handle the challenges of viscosity measurements over a wide range un aerosol of varying sizes.

Using these innovative new techniques, viscosity has been measured as a function of relative humidity for single organic aerosols composed of binary organic-aqueous mixtures in recent years.[52,86,87,91] Figure 1.5, reproduced from Song *et al.,*[91] compares the viscosity of different saccharides as a function of relative humidity measured using the holographic optical tweezers coalescence method. Approaching 100% RH all of the viscosities converge to the viscosity for water, $1x10^{-3}$ Pa·s, as the solution droplets become infinitely diluted at this limit. As the RH decreases, the saccharide viscosities diverge from one, and reach the glass transition viscosity, $1x10^{12}$ Pa·s, at different RH. The difference in viscosity between the simple saccharide model systems highlights the significant impact of structural differences on bulk properties. Other studies have

specifically compared viscosity measurements of organic model systems as a function of hydroxyl groups, suggesting a near-linear relationship between the $\log_{10}$(viscosity) and the addition of OH groups to a carbon backbone.[86] The experimental measurements are often compared to models which use functional group and thermodynamic treatments, however improvement between theory and experiment has increased due to the available data used to train the models.[86,91–93] Therefore even simple model systems are of great importance for gaining a better understanding of atmospherically relevant aerosols.

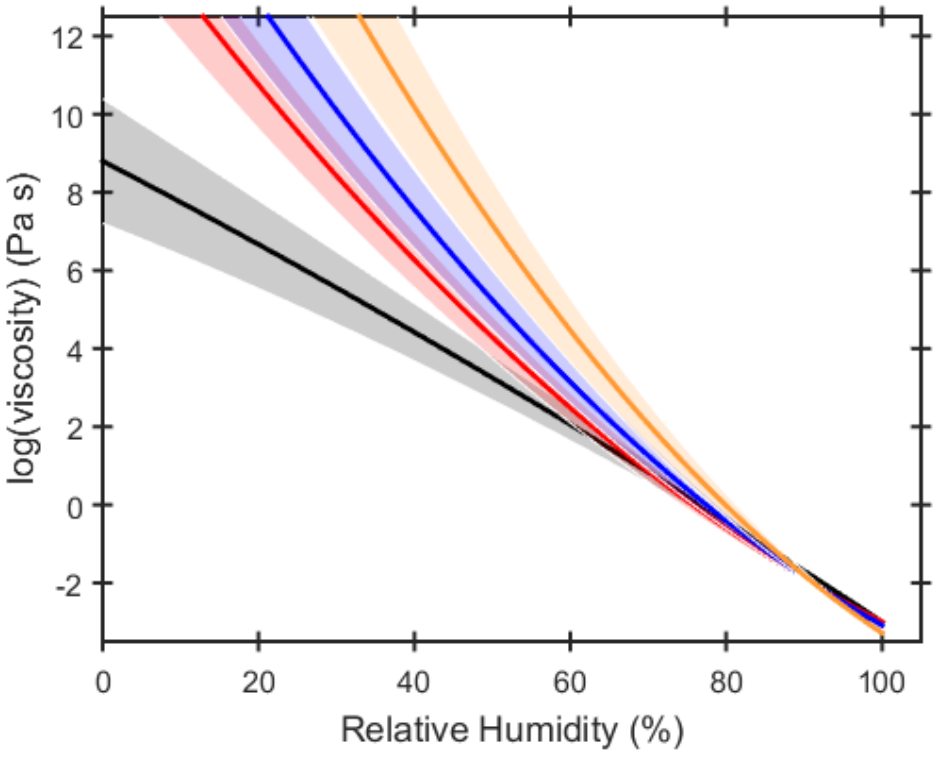

Figure 1.5. Empirical parameterizations for the viscosity measurements of single saccharide aerosols using holographic optical tweezers from Song *et al*:[91] monosaccharide (glucose, black), three disaccharides (sucrose, red; trehalose, blue) and a trisaccharide (raffinose, orange), shaded regions correspond to 95% confidence intervals.

Studies have also examined increasing complexity in model systems by measuring the viscosity of ternary mixtures.[79,87,94] Figure 1.6, adapted from Power *et al.*[87] shows the viscosity of mixed sucrose-sodium chloride droplets with molar ratio (sucrose:NaCl) 1:4, 1:2, 1:1, 2:1, and 4:1 compared with the binary sucrose-water mixture. The data are compared with model predictions using the Chenlo *et al.*[95] parameterization of viscosity with molar ratio of NaCl and sucrose, the Norrish[76] parameterization for the water activity of sucrose, ADDEM model,[44,96] and the pure additivity mixing rules of ZSR.[72] The results show a trend of increasing viscosity with greater mole fraction of sucrose, as expected given the difference in viscosity of sucrose and sodium chloride. It should be noted that sodium chloride aqueous droplets undergo deliquescence below 45% RH, however the addition of a non-deliquescing organic compound, in this case sucrose, prevents crystallization. The model predictions are consistent with the binary sucrose-water measurements, not shown in this figure, and agree well with the 4:1 sucrose/NaCl data. However, the model consistently under-predicts the viscosity for all other mixing ratios, which has been attributed to the sucrose molecules disproportionately increasing the viscosity by dominating the mechanical properties of the mixture.

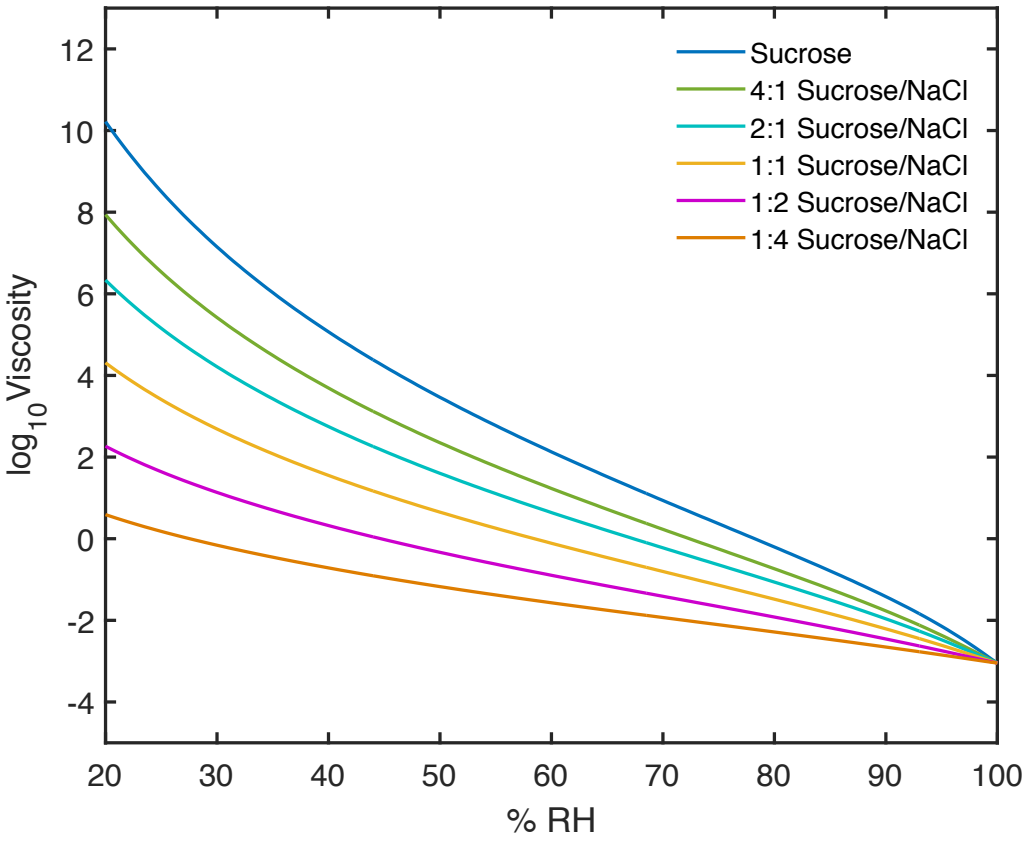

Figure 1.6. Predictions of viscosity of sucrose-NaCl aerosols as a function of RH for varying molar described in Power *et al*.[87]

Another analytical method using optical tweezers and elastic light scattering infers the viscosity from the measured change in size of a droplet in response to a fast RH change. The authors show that varying the molar ratio of sucrose to NaCl in a ternary mixture leads to a difference in viscosity by several orders of magnitude compared to the binary mixture.[79] Drastic increases in aerosol viscosity are accompanied by slower

growth and evaporation responses, as shown in Figure 1.7 where the half time is defined as the time required for an aerosol to reach half of the radius of the equilibrium size:

$$\tau_{1/2} = \frac{r^2}{\pi^2 D \cdot ln(2)} \tag{1.1}$$

where r is the aerosol radius and D is the coefficient of diffusion (m^2/s). The blue lines represent sucrose-water binary aerosols that exhibit an increase in half time by several orders of magnitude as the RH is lowered from 40% to 20% RH. A 1:1 molar sucrose/NaCl mixed aerosol, shown in red, exhibits a lower half time by over 5 orders of magnitude at the same RH, adapted from Bones *et al.*[79] The behavior is attributed to an increase in hygroscopicity with the addition of NaCl, which has a higher uptake of water for a given RH. These results imply that for highly viscous aerosol at sizes below 1 μm, the timescales for equilibration are on the order of minutes to days which is significant compared to response times of liquid-like aerosols.

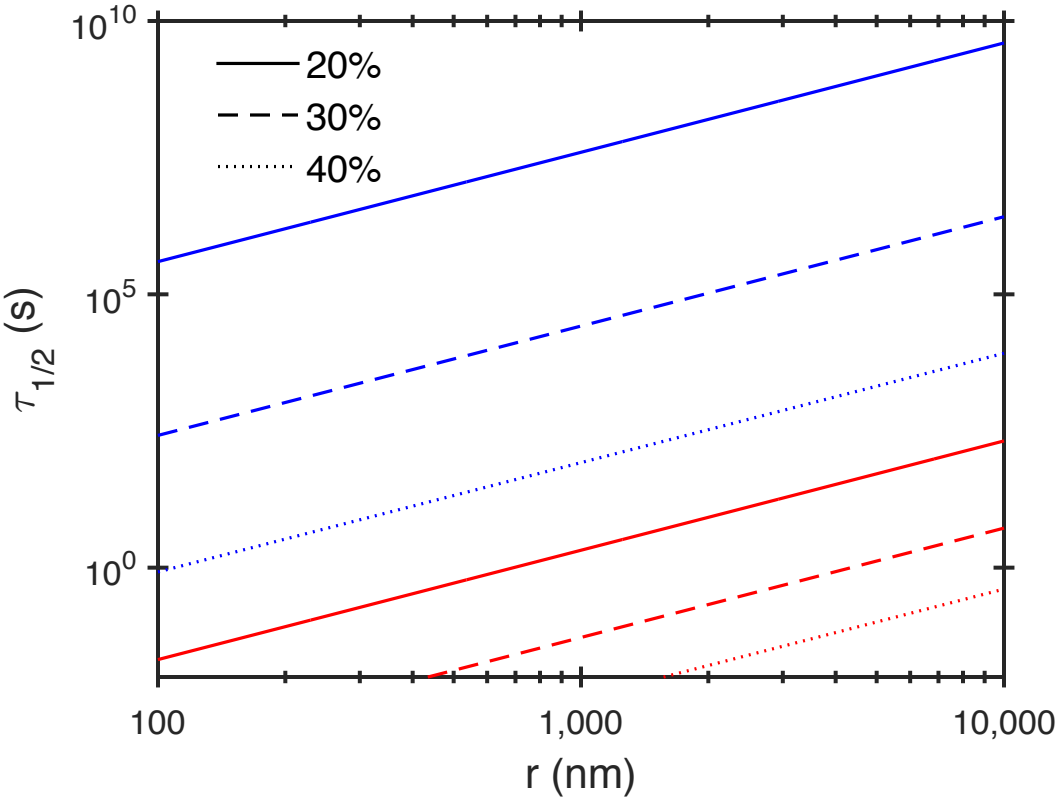

Figure 1.7. Estimated half-times for sucrose (blue) aerosols and 1:1 molar ratio of sucrose-NaCl (red) aerosols at 20%, 30%, and 40% RH and 298 K as a function of size.

1.3 Water diffusion in aerosols

The diffusion of molecular components, or molecular mobility, in an aerosol significantly impacts the kinetics of evaporation and condensation processes,[79,97] as well as the progress of heterogeneous reactions.[98] Specifically, water diffusion is important for cloud activation as the translational movement of the water into the particle is necessary for growth to occur.[99] If the water mobility is severely limited, the aerosol may not

achieve activation, which has significant climate implications. Molecular diffusion described by Fick's first law shows that the steady-state molecular flux, *J*, is driven by the a concentration gradient, ∂c/∂r

$$J = -D\frac{\partial c}{\partial r} \tag{1.2}$$

where *D* is the diffusion coefficient. The time-dependent non-steady state diffusion is described by Fick's second law which describes the concentration of a molecular species as a function of radial distance and time, *c(r,t),* given by:

$$\frac{\partial c(r,t)}{\partial t} = D\nabla^2 \mathrm{c} \tag{1.3}$$

and applied to a sphere, the time-dependent concentration follows:

$$\frac{\partial c}{\partial t} = \frac{1}{r^2}\frac{\partial}{\partial r}\left(Dr^2\frac{\partial c}{\partial r}\right) \tag{1.4}$$

where *r* is the radial position in a sphere. The diffusion coefficients in a pure substance are termed self-diffusion, and the mutual diffusion in a mixture of molecules is mathematically described as a combination of the individual components of self-diffusion. Different mixing rules have been applied to describe mutual diffusion with concentrations of components, such as the Vignes relationship which uses an exponential relationship between self diffusion coefficients of the molecular species *i* and *j:*[100]

$$D_{\mathrm{ij}} = \left(D_{i,self}\right)^{x_i}\left(D_{j,self}\right)^{x_j} \tag{1.5}$$

which has shown to provide good agreement in viscous fluids, particularly when the difference between self diffusion coefficients is large.[101]

The Stokes-Einstein (S-E) relationship predicts the diffusion coefficient of a molecule, *D,* given by:

$$D = \frac{k_B T}{6\pi \cdot a \cdot \eta} \tag{1.6}$$

where k_B is Boltzmann's constant, T (K) is temperature, a is the radius of the diffusing species, and η is the dynamic viscosity (Pa·s). With the push toward analytical instrumentation for measuring viscosity of single aerosols, and only a limited number of techniques which can measure diffusion in aerosols directly, the S-E relationship has been widely used to infer the diffusion coefficient of water.[75,79,81,102] However S-E has been shown to break down at high viscosity, a phenomenon which has been studied extensively,[87,97,103–108] and most widely accepted explanation is the formation dynamical heterogeneities, or essential domains within the medium which exhibit different behavior compared to the average material.[109] Therefore the application of the S-E has been shown to provide only a lower bound to the estimation of the diffusion coefficient.[87,105,110] Inaccuracies in using viscosity measurements and the S-E relation highlight the need for techniques which measure water diffusion directly.

The development of methods to measure slow water diffusion in the aerosol phase directly has been a challenge, and only in recent years several complementary methods

have been reported. A few methods will be described in detail in order to explain the theoretical framework, discuss the experimental limitations, and set the stage for the introduction of the new method presented in this dissertation.

The first category of diffusion measurement techniques, called the Raman tracer method, uses Raman spectroscopy to track the translational movement of an isotopically-labeled tracer molecule, which is measured by a difference in Raman shift. Zhu *et al.* first applied this framework to quantify the coefficient of water in aqueous maltose using D_2O as the tracer species.[111] Aqueous solutions of varying weight percent of maltose were prepared in either D_2O or H_2O, and one drop of each deuterated and non-deuterated solution were placed on a hydrophobic glass slide. When the droplets were compressed using a cover slide into 80 – 130 μm thick disks, the interface created where the discs touched was monitored over time using a Raman microscope to map the ν(O-D) peak intensity as a function of position and time. Using this technique the concentration-dependent water diffusion coefficient of water in maltose was measured and validated using the pulsed-gradient stimulated-echo technique of Tanner *et al.* for D_w larger than 1 x 10^{-11} m^2 s.[111] The technique demonstrated the ability to use Raman microscopy to measure diffusion over 8 orders of magnitude. Price *et al.* extended the method of Zhu to measure the diffusion coefficient for water in a sucrose-water disk by isotopically labeling the gas phase molecules and monitoring the substitution of D_2O for H_2O in the solution with Raman microscopy.[108] The method expanded the library of water diffusion coefficients in a number of chemical systems, and enabled direct comparison of methods

compared to previous studies. However, the experiments at low RH were carried out over several weeks because of the long timescales and relative large sample sizes (100's of μm) and required the use of a substrate.

Studying water diffusion of atmospheric aerosols using single particle, contactless techniques are preferred because the aerosol is free from impacts of surface perturbations at concentrations above the solubility limit. In addition, single particle measurements are preferred over ensemble-averaged experiments, because composition and local chemical environments vary from particle to particle. A widely used technique, optical tweezers, enables spectroscopic studies of single, spherical particles from 1-10 μm in diameter that are trapped at the center of a tightly focused laser beam by a balance of photon gradient forces which are insensitive to charge state.[112] Scattering from the focusing laser is collected to provide high resolution size measurements using cavity enhanced features of the light scattering such as morphology dependent resonances,[113,114] as well as chemical identity from the Raman scattering or fluorescence. The response of a single particle to changes in humidity or ambient gaseous composition provides measurements of chemical kinetics,[20,21] and hygroscopicity.[115] Davies *et al.* applied the isotopic exchange technique together with aerosol optical tweezers for single-particle confinement[116] which reduced the sample size to less than 6 μm radius, speeding up the experimental timescales from weeks to hours. Similar to Price *et al.,* the optical tweezers isotopic tracer experiments were carried out at a constant RH, and therefore constant aerosol size and solute concentration. Fick's second law of diffusion applied to a sphere was used to model the

time-dependent intensities of the ν(O-D) and ν(O-H) Raman peaks to quantify the diffusion coefficient as a function of concentration, or water activity, in sucrose, citric acid, sucrose/citric acid mixtures, and shikimic acid.[116] The results were modeled using a Vignes-type parameterization of Equation 1.5 where the self-diffusion coefficient of water is 2 x 10^{-9} m^2/s and the coefficient of the solute component, $D^0_{w,org}$, was empirically determined for different molecular compositions. In mixtures of sucrose/citric acid the $D^0_{w,org}$ was determined to be a log-linear function of mass fraction, enabling an effective mixed-solute $D^0_{w,org}$ to satisfy a Vignes fit without requiring an activity coefficient correction. The results presented by Davies *et al.* suggest the practicality of applying the isotope tracer method in conjunction with a single particle confinement technique for measuring a water diffusion in variety of atmospherically-relevant viscous aerosols.

The second category of aerosol diffusion techniques is the mass transport method which infers diffusion coefficients from the water-uptake driven growth of single, levitated aerosols in response to stepwise changes in the environmental RH.[75,81,117] These experiments are carried out by trapping a single, micron-sized aerosol using optical tweezers or an electrodynamic balance (EDB). The electrodynamic balance is a single particle technique that offers similar advantages to optical tweezers, including contactless levitation. However, it is not limited by size or morphology, as the trapping potential depends solely on mass-to-charge ratio. EDBs have been used extensively to measure physicochemical properties of single aerosol particles such as evaporation rates[118–121] and nucleation,[122–126] and provide complementary results to optical tweezers.

Zobrist *et al.* first conducted water diffusion measurements by trapping a single aqueous droplet at an initial RH and after sufficient time for equilibration, the RH was quickly increased of decreased and the droplet growth response was measured using Mie resonance spectroscopy.[75] The kinetic response of water evaporating or condensing in the droplet is strongly dependent on the diffusion coefficient of water, which becomes slow at high viscosity. The size response curves as a function of time were interpreted using a theoretical framework based on principles of mass transport which applies a numerical analysis which divides the particle into a discrete number of concentric shells, typically 100-200 of no less than 0.3 nm thickness, between which water molecules translationally move to reach equilibrium. If the flux of the water molecules between shells, described by D_w, was assumed to remain constant at the rate of the water self-diffusion coefficient, the model would over-predict the growth response measurements. Instead, the model accounts for the formation of a highly nonlinear radial concentration gradient between the center of the droplet, initially equal to the concentration given by the initial RH condition, and the outermost layer, which is assumed to establish equilibrium with the gas phase instantaneously. In this way, the time dependence of the droplet size is modeled by dynamically changing the concentration profile of each shell as the droplet approaches equilibrium, yielding excellent agreement with the measurements. The function describing the concentration profile numerically represents the number of solute molecules and water molecules present in each shell at a given time, can be used to infer the value of D_w from the average concentration of neighboring shells.[75,81] For RH steps near the glass transition of ~ 23%, the concentration gradient becomes more pronounced

leading to a steep diffusion front where the particle assumes an approximate core-shell morphology. At a constant RH, retrieving the refractive index, *RI,* from the Mie resonance spectrum is straightforward because the droplet concentration is homogeneous. However, when a steep concentration front is formed by a step to low RH, the RI becomes a fit parameter along with the radius, leading to an increase in the uncertainty by an order of magnitude.[127] Thus the accuracy of the radius measurement decreases at low RH when the difference in solute concentration between the viscous core and the liquid surface layer is extremely large.

Despite differences in experimental setups, the isotope tracing model and mass transport model produce similar water diffusion coefficients in sucrose over a wide range of RH.[75,108,116] Deviations between the methods arise near the glass transition at low RH where Zobrist *et al.*[75] predicts a diffusion coefficient nearly 3 orders of magnitude higher than Price *et al.*[108] An analysis of the uncertainties in mass transport kinetics at high viscosities points out key differences in analytical and numerical methodology to solve the diffusion equations, parameterizations of mass fraction and density, and experimental challenges associated with maintaining constant RH and temperature conditions over extended periods of time.[127] At low RH, <25 %, small changes to the RH or temperature result in large shifts in diffusion timescales because of the logarithmic dependence, which poses a significant source of uncertainty as instrumental drifts in temperature and RH are common and the accuracy of RH probes is typically on the order of 1– 3%. Furthermore, the choice of parameterization for the dependence of mass fraction, density, and

refractive index with water activity can lead to significant differences below $a_w = 0.3$.[74–76,127] However it was demonstrated that when different thermodynamic treatments for the mass fraction dependence of sucrose were re-considered in the mass transport method analysis of Zobrist *et al.,* other parameterizations could not reproduce the experimental response functions. The disparity between methods at low RH highlights the need for additional techniques capable of measuring the diffusion of highly viscous aerosols, as well an expansion of the library of compounds for which diffusion coefficients have been measured to improve predictions of kinetic behaviors with chemical composition.

The present work reports a new technique that combines the Raman spectroscopic isotope tracing method on substrate-supported droplets previously applied by Price *et al.*[108] with single particle electrodynamic trapping. Instead of following the approach of Davies *et al.* to isolate single aerosol in optical tweezers,[116] we used a RH-controlled EDB to trap single charged aerosol droplets for measuring water diffusion. A microdroplet containing a solute-H_2O mixture is trapped and equilibrated at a specific RH, and then exposed to D_2O at the same RH. The D_2O behaves as an isotopically labeled tracer molecule with assumed identical diffusion properties as H_2O.[116] Raman spectra of the droplet are acquired as a function of time, in order to assess the progression of D_2O diffusing into the droplet. D_2O was observed to eventually replace all H_2O, as indicated by complete disappearance of the ν(O-H) asymmetric stretch peak in the Raman spectrum. It is assumed that the entire droplet is irradiated with the laser and the total content of water remains constant throughout an experiment so that a volume-averaged

Fickian diffusion model can be used to describe the exponential growth of the ν(O-D) Raman peak. The solute contentration-dependent water diffusion coefficient is measured at room temperature (22-24 C) under a range of RH from 20-55 %RH for binary and ternary model aerosol systems. The results are discussed in the context of previous diffusion coefficient measurements as well as comparison to coefficients predicted from the S-E relation when viscosity data are available. The ternary mixture diffusion coefficient results serve to expand the database of direct measurements of water diffusion which can be used to inform models and improve predictions of hygroscopic growth. Additional chemical systems, with a greater number of mixing ratios, will be necessary for continued evaluation of the use for the Stokes-Einstein relation to predict diffusion coefficients in semi-solid and glassy regimes.

1.4 Thesis Outline

The second chapter of this dissertation describes the experimental setup of a new, mobile electrodynamic balance which was designed and characterized for the purpose of conducting single particle atmospheric-pressure water diffusion, ice nucleation, and heterogeneous chemistry measurements. The experimental capabilities of the apparatus are discussed, along with the development of methodology for performing measurements of water diffusion on single, charged aerosol.

The third chapter focuses on the application of the mobile EDB for conducting water diffusion measurements in single aerosol at room temperature as a function of relative humidity. The method was validated using a commonly used binary model system, sucrose-water, which showed good agreement with previous studies.

The fourth chapter reports water diffusion measurements in model aerosol composed of ternary mixtures using mobile EDB, which are compared to diffusion coefficients predicted from viscosity measurements and the S-E relation.

1.5 References

(1) McCormick, M. P.; Thomason, L. W.; Trepte, C. R. Atmospheric Effects of the Mt Pinatubo Eruption. *Nature* **1995**, *373* (6513), 399–404.

(2) Brasseur, G.; Granier, C. Mount Pinatubo Aerosols, Chlorofluorocarbons, and Ozone Depletion. *Science (80-.).* **1992**, *257* (5074), 1239–1242.

(3) Andreae, M. O.; Merlet, P. Emission of Trace Gases and Aerosols from Biomass Burning. *Global Biogeochem. Cycles* **2001**, *15* (4), 955–966.

(4) Crutzen, P. J.; Andreae, M. O.; O'Neill, C. A. Biomass Burning in the Tropics: Impact on Atmospheric Chemistry and Biogeochemical Cycles. *Science* **1990**, *250* (4988), 1669–1678.

(5) Jacobson, M. Z. Strong Radiative Heating Due to the Mixing State of Black Carbon in Atmospheric Aerosols. *Nature* **2001**, *409* (6821), 695–697.

(6) Martins, J. V.; Artaxo, P.; Liousse, C.; Reid, J. S.; Hobbs, P. V.; Kaufman, Y. J. Effects of Black Carbon Content, Particle Size, and Mixing on Light Absorption by Aerosols from Biomass Burning in Brazil. *J. Geophys. Res. Atmos.* **1998**, *103* (D24), 32041–32050.

(7) Andreae, M. O.; Crutzen, P. J. Atmospheric Aerosols: Biogeochemical Sources and Role in Atmospheric Chemistry. *Science (80-.).* **1997**, *276* (5315), 1052–

1058.

(8) Tegen, I.; Fung, I. Modeling of Mineral Dust in the Atmosphere: Sources, Transport, and Optical Thickness. *J. Geophys. Res.* **1994**, *99* (D11), 22897.

(9) DeMott, P. J.; Sassen, K.; Poellot, M. R.; Baumgardner, D.; Rogers, D. C.; Brooks, S. D.; Prenni, A. J.; Kreidenweis, S. M. African Dust Aerosols as Atmospheric Ice Nuclei. *Geophys. Res. Lett.* **2003**, *30* (14).

(10) Claquin, T.; Schulz, M.; Balkanski, Y. J. Modeling the Mineralogy of Atmospheric Dust Sources. *J. Geophys. Res. Atmos.* **1999**, *104* (D18), 22243–22256.

(11) Wang, X. F.; Sultana, C. M.; Trueblood, J.; Hill, T. C. J.; Malfatti, F.; Lee, C.; Laskina, O.; Moore, K. A.; Beall, C. M.; McCluskey, C. S.; et al. Microbial Control of Sea Spray Aerosol Composition: A Tale of Two Blooms. *Acs Cent. Sci.* **2015**, *1* (3), 124–131.

(12) DeMott, P. J.; Hill, T. C. J.; McCluskey, C. S.; Prather, K. A.; Collins, D. B.; Sullivan, R. C.; Ruppel, M. J.; Mason, R. H.; Irish, V. E.; Lee, T.; et al. Sea Spray Aerosol as a Unique Source of Ice Nucleating Particles. *Proc. Natl. Acad. Sci. U. S. A.* **2016**, *113* (21), 5797–5803.

(13) Shrivastava, M.; Cappa, C. D.; Fan, J.; Goldstein, A. H.; Guenther, A. B.; Jimenez, J. L.; Kuang, C.; Laskin, A.; Martin, S. T.; Ng, N. L.; et al. Recent Advances in Understanding Secondary Organic Aerosol: Implications for Global Climate Forcing. *Rev. Geophys.* **2017**, *55* (2), 509–559.

(14) Pöschl, U. Atmospheric Aerosols: Composition, Transformation, Climate and Health Effects. *Angew. Chemie Int. Ed.* **2005**, *44* (46), 7520–7540.

(15) Brooks, S. D.; Wise, M. E.; Cushing, M.; Tolbert, M. A. Deliquescence Behavior of Organic/Ammonium Sulfate Aerosol. *Geophys. Res. Lett.* **2002**, *29* (19).

(16) Choi, M. Y.; Chan, C. K. Investigation of Efflorescence of Inorganic Aerosols Using Fluorescence Spectroscopy. *J. Phys. Chem. A* **2005**, *109* (6), 1042–1048.

(17) Grayson, J. W.; Song, M.; Sellier, M.; Bertram, A. K. Validation of the Poke-Flow Technique Combined with Simulations of Fluid Flow for Determining Viscosities in Samples with Small Volumes and High Viscosities. *Atmos. Meas. Tech.* **2015**, *8* (6), 2463–2472.

(18) Renbaum-Wolff, L.; Grayson, J. W.; Bertram, A. K. Technical Note: New Methodology for Measuring Viscosities in Small Volumes Characteristic of Environmental Chamber Particle Samples. *Atmos. Chem. Phys.* **2013**, *13* (2), 791–802.

(19) Chim, M. M.; Cheng, C. T.; Davies, J. F.; Berkemeier, T.; Shiraiwa, M.; Zuend, A.; Chan, M. N. Compositional Evolution of Particle-Phase Reaction Products and Water in the Heterogeneous OH Oxidation of Model Aqueous Organic Aerosols. *Atmos. Chem. Phys.* **2017**, *17* (23), 14415–14431.

(20) Dennis-Smither, B. J.; Miles, R. E. H.; Reid, J. P. Oxidative Aging of Mixed Oleic Acid/Sodium Chloride Aerosol Particles. *J. Geophys. Res.* **2012**, *117*, D20204.

(21) Dennis-Smither, B. J.; Marshall, F. H.; Miles, R. E. H.; Preston, T. C.; Reid, J. P. Volatility and Oxidative Aging of Aqueous Maleic Acid Aerosol Droplets and the Dependence on Relative Humidity. *J. Phys. Chem. A* **2014**, *118* (30), 5680–5691.

(22) Jarvinen, E.; Ignatius, K.; Nichman, L.; Kristensen, T. B.; Fuchs, C.; Hoyle, C. R.; Hoppel, N.; Corbin, J. C.; Craven, J.; Duplissy, J.; et al. Observation of Viscosity Transition in Alpha-Pinene Secondary Organic Aerosol. *Atmos. Chem. Phys.* **2016**, *16* (7), 4423–4438.

(23) CHARLSON, R. J.; SCHWARTZ, S. E.; HALES, J. M.; CESS, R. D.; COAKLEY, J. A.; HANSEN, J. E.; HOFMANN, D. J. Climate Forcing by Anthropogenic Aerosols. *Science (80-.).* **1992**, *255* (5043), 423–430.

(24) Che, H. C.; Zhang, X. Y.; Zhang, L.; Wang, Y. Q.; Zhang, Y. M.; Shen, X. J.; Ma, Q. L.; Sun, J. Y.; Zhong, J. T. Prediction of Size-Resolved Number Concentration of Cloud Condensation Nuclei and Long-Term Measurements of Their Activation Characteristics. *Sci. Rep.* **2017**, *7* (1), 5819.

(25) Hartz, K. E. H.; Tischuk, J. E.; Chan, M. N.; Chan, C. K.; Donahue, N. M.; Pandis, S. N. Cloud Condensation Nuclei Activation of Limited Solubility Organic Aerosol. *Atmos. Environ.* **2006**, *40* (4), 605–617.

(26) Cotterell, M. I.; Mason, B. J.; Preston, T. C.; Orr-Ewing, A. J.; Reid, J. P. Optical Extinction Efficiency Measurements on Fine and Accumulation Mode Aerosol Using Single Particle Cavity Ring-down Spectroscopy. *Phys. Chem. Chem. Phys.* **2015**, *17* (24), 15843–15856.

(27) Cotterell, M. I.; Willoughby, R. E.; Bzdek, B. R.; Orr-Ewing, A. J.; Reid, J. P. A Complete Parameterisation of the Relative Humidity and Wavelength Dependence of the Refractive Index of Hygroscopic Inorganic Aerosol Particles. *Atmos. Chem. Phys.* **2017**, *17* (16), 9837–9851.

(28) DeMott, P. J.; Prenni, A. J.; Liu, X.; Kreidenweis, S. M.; Petters, M. D.; Twohy, C. H.; Richardson, M. S.; Eidhammer, T.; Rogers, D. C. Predicting Global Atmospheric Ice Nuclei Distributions and Their Impacts on Climate. *Proc. Natl. Acad. Sci. U. S. A.* **2010**, *107* (25), 11217–11222.

(29) Carslaw, K. S.; Lee, L. A.; Reddington, C. L.; Pringle, K. J.; Rap, A.; Forster, P. M.; Mann, G. W.; Spracklen, D. V.; Woodhouse, M. T.; Regayre, L. A.; et al. Large Contribution of Natural Aerosols to Uncertainty in Indirect Forcing. *Nature* **2013**, *503* (7474), 67–71.

(30) Lee, L. A.; Pringle, K. J.; Reddington, C. L.; Mann, G. W.; Stier, P.; Spracklen, D. V.; Pierce, J. R.; Carslaw, K. S. The Magnitude and Causes of Uncertainty in Global Model Simulations of Cloud Condensation Nuclei. *Atmos. Chem. Phys.* **2013**, *13* (17), 8879–8914.

(31) Andreae, M. O.; Rosenfeld, D. Aerosol–Cloud–Precipitation Interactions. Part 1. The Nature and Sources of Cloud-Active Aerosols. *Earth-Science Rev.* **2008**, *89* (1–2), 13–41.

(32) Marsh, A.; Rovelli, G.; Song, Y. C.; Pereira, K. L.; Willoughby, R. E.; Bzdek, B. R.; Hamilton, J. F.; Orr-Ewing, A. J.; Topping, D. O.; Reid, J. P. Accurate Representations of the Physicochemical Properties of Atmospheric Aerosols: When Are Laboratory Measurements of Value? *Faraday Discuss.* **2017**, *200*, 639–661.

(33) Reid, J. P.; Bertram, A. K.; Topping, D. O.; Laskin, A.; Martin, S. T.; Petters, M. D.; Pope, F. D.; Rovelli, G. The Viscosity of Atmospherically Relevant Organic Particles. *Nat. Commun.* **2018**, *9* (1), 956.

(34) Krieger, U. K.; Marcolli, C.; Reid, J. P. Exploring the Complexity of Aerosol Particle Properties and Processes Using Single Particle Techniques. *Chem. Soc. Rev.* **2012**, *41* (19), 6631.

(35) Petters, M. D.; Kreidenweis, S. M. A Single Parameter Representation of Hygroscopic Growth and Cloud Condensation Nucleus Activity. *Atmos. Chem. Phys.* **2007**, *7* (8), 1961–1971.

(36) Komppula, M.; Lihavainen, H.; Kerminen, V. M.; Kulmala, M.; Viisanen, Y. Measurements of Cloud Droplet Activation of Aerosol Particles at a Clean Subarctic Background Site. *J. Geophys. Res.* **2005**, *110*, D06204.

(37) Pratt, K. A.; Prather, K. A. Aircraft Measurements of Vertical Profiles of Aerosol Mixing States. *J. Geophys. Res.* **2010**, *115*.

(38) Ryan C. Sullivan, A.; Prather, K. A. Recent Advances in Our Understanding of Atmospheric Chemistry and Climate Made Possible by On-Line Aerosol Analysis Instrumentation. **2005**.

(39) Pratt, K. A.; Mayer, J. E.; Holecek, J. C.; Moffet, R. C.; Sanchez, R. O.; Rebotier, T. P.; Furutani, H.; Gonin, M.; Fuhrer, X. K.; Su, X. Y.; et al. Development and

Characterization of an Aircraft Aerosol Time-of-Flight Mass Spectrometer. **2009**, *81* (5), 1792–1800.

(40) Pratt, K. A.; DeMott, P. J.; French, J. R.; Wang, Z.; Westphal, D. L.; Heymsfield, A. J.; Twohy, C. H.; Prenni, A. J.; Prather, K. A. In Situ Detection of Biological Particles in Cloud Ice-Crystals. *Nat. Geosci.* **2009**, *2* (6), 397–400.

(41) Prather, K. A.; Bertram, T. H.; Grassian, V. H.; Deane, G. B.; Stokes, M. D.; DeMott, P. J.; Aluwihare, L. I.; Palenik, B. P.; Azam, F.; Seinfeld, J. H.; et al. Bringing the Ocean into the Laboratory to Probe the Chemical Complexity of Sea Spray Aerosol. *Proc. Natl. Acad. Sci. U. S. A.* **2013**, *110* (19), 7550–7555.

(42) Jentzsch, P. V; Kampe, B.; Ciobota, V.; Rosch, P.; Popp, J. Inorganic Salts in Atmospheric Particulate Matter: Raman Spectroscopy as an Analytical Tool. *Spectrochim. Acta Part a-Molecular Biomol. Spectrosc.* **2013**, *115*, 697–708.

(43) Choi, M. Y.; Chan, C. K. The Effects of Organic Species on the Hygroscopic Behaviors of Inorganic Aerosols. *Environ. Sci. Technol.* **2002**, *36* (11), 2422–2428.

(44) Topping, D. O.; McFiggans, G. B.; Coe, H. A Curved Multi-Component Aerosol Hygroscopicity Model Framework: Part 1 - Inorganic Compounds. *Atmos. Chem. Phys.* **2005**, *5*, 1205–1222.

(45) Abbatt, J. P. D.; Benz, S.; Cziczo, D. J.; Kanji, Z.; Lohmann, U.; Mohler, O. Solid Ammonium Sulfate Aerosols as Ice Nuclei: A Pathway for Cirrus Cloud Formation. *Science (80-.).* **2006**, *313* (5794), 1770–1773.

(46) Hameri, K.; Charlson, R.; Hansson, H. C. Hygroscopic Properties of Mixed Ammonium Sulfate and Carboxylic Acids Particles. *Aiche J.* **2002**, *48* (6), 1309–1316.

(47) Meresman, H.; Hudson, A. J.; Reid, J. P. Spectroscopic Characterization of Aqueous Microdroplets Containing Inorganic Salts. *Analyst* **2011**, *136* (17), 3487–3495.

(48) Cruz, C. N.; Pandis, S. N. Deliquescence and Hygroscopic Growth of Mixed Inorganic-Organic Atmospheric Aerosol. *Environ. Sci. Technol.* **2000**, *34* (20), 4313–4319.

(49) Chan, M. N.; Lee, A. K. Y.; Chan, C. K. Responses of Ammonium Sulfate Particles Coated with Glutaric Acid to Cyclic Changes in Relative Humidity: Hygroscopicity and Raman Characterization. *Environ. Sci. Technol.* **2006**, *40* (22), 6983–6989.

(50) Estillore, A. D.; Morris, H. S.; Or, V. W.; Lee, H. D.; Alves, M. R.; Marciano, M.

A.; Laskina, O.; Qin, Z.; Tivanski, A. V.; Grassian, V. H. Linking Hygroscopicity and the Surface Microstructure of Model Inorganic Salts, Simple and Complex Carbohydrates, and Authentic Sea Spray Aerosol Particles. *Phys. Chem. Chem. Phys.* **2017**, *19* (31), 21101–21111.

(51) Hansson, H. C.; Rood, M. J.; Koloutsou-Vakakis, S.; Hameri, K.; Orsini, D.; Wiedensohler, A. NaCl Aerosol Particle Hygroscopicity Dependence on Mixing with Organic Compounds. *J. Atmos. Chem.* **1998**, *31* (3), 321–346.

(52) Marsh, A.; Miles, R. E. H.; Rovelli, G.; Cowling, A. G.; Nandy, L.; Dutcher, C. S.; Reid, J. P. Influence of Organic Compound Functionality on Aerosol Hygroscopicity: Dicarboxylic Acids, Alkyl-Substituents, Sugars and Amino Acids. *Atmos. Chem. Phys.* **2017**, *17* (9), 5583–5599.

(53) Rovelli, G.; Miles, R. E. H.; Reid, J. P.; Clegg, S. L. Accurate Measurements of Aerosol Hygroscopic Growth over a Wide Range in Relative Humidity. *J. Phys. Chem. A* **2016**, *120* (25), 4376–4388.

(54) Pope, F. D.; Dennis-Smither, B. J.; Griffiths, P. T.; Clegg, S. L.; Cox, R. A. Studies of Single Aerosol Particles Containing Malonic Acid, Glutaric Acid, and Their Mixtures with Sodium Chloride. I. Hygroscopic Growth. *J. Phys. Chem. A* **2010**, *114* (16), 5335–5341.

(55) Cochran, R. E.; Laskina, O.; Trueblood, J. V.; Estillore, A. D.; Morris, H. S.; Jayarathne, T.; Sultana, C. M.; Lee, C.; Lin, P.; Laskin, J.; et al. Molecular Diversity of Sea Spray Aerosol Particles: Impact of Ocean Biology on Particle Composition and Hygroscopicity. *Chem* **2017**, *2* (5), 655–667.

(56) Tang, I. N.; Tridico, A. C.; Fung, K. H. Thermodynamic and Optical Properties of Sea Salt Aerosols. *J. Geophys. Res. Atmos.* **1997**, *102* (D19), 23269–23275.

(57) Gong, S. L.; Barrie, L. A.; Blanchet, J.-P. Modeling Sea-Salt Aerosols in the Atmosphere: 1. Model Development. *J. Geophys. Res. Atmos.* **1997**, *102* (D3), 3805–3818.

(58) Gong, S. L. A Parameterization of Sea-Salt Aerosol Source Function for Sub- and Super-Micron Particles. *Global Biogeochem. Cycles* **2003**, *17* (4), n/a-n/a.

(59) Jayarathne, T.; Sultana, C. M.; Lee, C.; Malfatti, F.; Cox, J. L.; Pendergraft, M. A.; Moore, K. A.; Azam, F.; Tivanski, A. V; Cappa, C. D.; et al. Enrichment of Saccharides and Divalent Cations in Sea Spray Aerosol During Two Phytoplankton Blooms. *Environ. Sci. Technol.* **2016**, *50* (21), 11511–11520.

(60) Quinn, P. K.; Collins, D. B.; Grassian, V. H.; Prather, K. A.; Bates, T. S. Chemistry and Related Properties of Freshly Emitted Sea Spray Aerosol. *Chem.*

Rev. **2015**, *115* (10), 4383–4399.

(61) Collins, D. B.; Zhao, D. F.; Ruppel, M. J.; Laskina, O.; Grandquist, J. R.; Modini, R. L.; Stokes, M. D.; Russell, L. M.; Bertram, T. H.; Grassian, V. H.; et al. Direct Aerosol Chemical Composition Measurements to Evaluate the Physicochemical Differences between Controlled Sea Spray Aerosol Generation Schemes. *Atmos. Meas. Tech.* **2014**, *7* (11), 3667–3683.

(62) Russell, L. M.; Hawkins, L. N.; Frossard, A. A.; Quinn, P. K.; Bates, T. S. Carbohydrate-like Composition of Submicron Atmospheric Particles and Their Production from Ocean Bubble Bursting. *Proc. Natl. Acad. Sci. U. S. A.* **2010**, *107* (15), 6652–6657.

(63) Quinn, P. K.; Bates, T. S.; Schulz, K. S.; Coffman, D. J.; Frossard, A. A.; Russell, L. M.; Keene, W. C.; Kieber, D. J. Contribution of Sea Surface Carbon Pool to Organic Matter Enrichment in Sea Spray Aerosol. *Nat. Geosci.* **2014**, *7* (3), 228–232.

(64) Cochran, R. E.; Laskina, O.; Jayarathne, T.; Laskin, A.; Laskin, J.; Lin, P.; Sultana, C.; Lee, C.; Moore, K. A.; Cappa, C. D.; et al. Analysis of Organic Anionic Surfactants in Fine and Coarse Fractions of Freshly Emitted Sea Spray Aerosol. *Environ. Sci. Technol.* **2016**, *50* (5), 2477–2486.

(65) Cochran, R. E.; Jayarathne, T.; Stone, E. A.; Grassian, V. H. Selectivity Across the Interface: A Test of Surface Activity in the Composition of Organic-Enriched Aerosols from Bubble Bursting. *J. Phys. Chem. Lett.* **2016**, *7* (9), 1692–1696.

(66) Ault, A. P.; Axson, J. L. Atmospheric Aerosol Chemistry: Spectroscopic and Microscopic Advances. *Anal. Chem.* **2017**, *89* (1), 430–452.

(67) Wex, H.; Stratmann, F.; Topping, D.; McFiggans, G. The Kelvin versus the Raoult Term in the Köhler Equation. *J. Atmos. Sci.* **2008**, *65* (12), 4004–4016.

(68) Wexler, A. S.; Clegg, S. L. Atmospheric Aerosol Models for Systems Including the Ions H+, NH4+, Na+, SO42-, NO3-,Cl-, Br-, and H2O. *J. Geophys. Res.* **2002**, *107* (D14).

(69) Clegg, S. L.; Brimblecombe, P.; Wexler, A. S. Thermodynamic Model of the System H+-NH4+-Na+-SO42--NB3--Cl--H2O at 298.15 K. *J. Phys. Chem. A* **1998**, *102* (12), 2155–2171.

(70) Zuend, A.; Marcolli, C.; Luo, B. P.; Peter, T. A Thermodynamic Model of Mixed Organic-Inorganic Aerosols to Predict Activity Coefficients. *Atmos. Chem. Phys.* **2008**, *8* (16), 4559–4593.

(71) Topping, D.; Barley, M.; Bane, M. K.; Higham, N.; Aumont, B.; Dingle, N.;

McFiggans, G. UManSysProp v1.0: An Online and Open-Source Facility for Molecular Property Prediction and Atmospheric Aerosol Calculations. *Geosci. Model Dev.* **2016**, *9* (2), 899–914.

(72) Stokes, R. H.; Robinson, R. A. Interactions in Aqueous Nonelectroylte Solutions I. Solute-Solvent Equilibria. *J. Phys. Chem.* **1966**, *70* (7), 2126-.

(73) Dutcher, C. S.; Ge, X.; Wexler, A. S.; Clegg, S. L. An Isotherm-Based Thermodynamic Model of Multicomponent Aqueous Solutions, Applicable Over the Entire Concentration Range. *J. Phys. Chem. A* **2013**, *117* (15), 3198–3213.

(74) Cai, C.; Miles, R. E. H.; Cotterell, M. I.; Marsh, A.; Rovelli, G.; Rickards, A. M. J.; Zhang, Y. H.; Reid, J. P. Comparison of Methods for Predicting the Compositional Dependence of the Density and Refractive Index of Organic-Aqueous Aerosols. *J. Phys. Chem. A* **2016**, *120* (33), 6604–6617.

(75) Zobrist, B.; Soonsin, V.; Luo, B. P.; Krieger, U. K.; Marcolli, C.; Peter, T.; Koop, T. Ultra-Slow Water Diffusion in Aqueous Sucrose Glasses. *Phys. Chem. Chem. Phys.* **2011**, *13* (8), 3514–3526.

(76) Norrish, R. S. An Equation for the Activity Coefficients and Equilibrium Relative Humidities of Water in Confectionery Syrups. *J. Food Sci. Technol.* **1966**, *1*, 25–39.

(77) Shiraiwa, M.; Zuend, A.; Bertram, A. K.; Seinfeld, J. H. Gas–Particle Partitioning of Atmospheric Aerosols: Interplay of Physical State, Non-Ideal Mixing and Morphology. *Phys. Chem. Chem. Phys.* **2013**, *15* (27), 11441.

(78) Shiraiwa, M.; Seinfeld, J. H. Equilibration Timescale of Atmospheric Secondary Organic Aerosol Partitioning. *Geophys. Res. Lett.* **2012**, *39* (24), L24801.

(79) Bones, D. L.; Reid, J. P.; Lienhard, D. M.; Krieger, U. K. Comparing the Mechanism of Water Condensation and Evaporation in Glassy Aerosol. *Proc. Natl. Acad. Sci. U. S. A.* **2012**, *109* (29), 11613–11618.

(80) Koop, T.; Bookhold, J.; Shiraiwa, M.; Pöschl, U. Glass Transition and Phase State of Organic Compounds: Dependency on Molecular Properties and Implications for Secondary Organic Aerosols in the Atmosphere. *Phys. Chem. Chem. Phys.* **2011**, *13* (43), 19238.

(81) Lienhard, D. M.; Huisman, A. J.; Krieger, U. K.; Rudich, Y.; Marcolli, C.; Luo, B. P.; Bones, D. L.; Reid, J. P.; Lambe, A. T.; Canagaratna, M. R.; et al. Viscous Organic Aerosol Particles in the Upper Troposphere: Diffusivity-Controlled Water Uptake and Ice Nucleation? *Atmos. Chem. Phys.* **2015**, *15* (23), 13599–13613.

(82) Yli-Juuti, T.; Pajunoja, A.; Tikkanen, O.-P.; Buchholz, A.; Faiola, C.; Väisänen,

O.; Hao, L.; Kari, E.; Peräkylä, O.; Garmash, O.; et al. Factors Controlling the Evaporation of Secondary Organic Aerosol from α-Pinene Ozonolysis. *Geophys. Res. Lett.* **2017**, *44* (5), 2562–2570.

(83) Zobrist, B.; Marcolli, C.; Pedernera, D. A.; Koop, T. Do Atmospheric Aerosols Form Glasses? *Atmos. Chem. Phys.* **2008**, *8* (17), 5221–5244.

(84) Läuger, J.; Stettin, H. Differences between Stress and Strain Control in the Non-Linear Behavior of Complex Fluids. *Rheol. Acta* **2010**, *49* (9), 909–930.

(85) Booth, A. M.; Murphy, B.; Riipinen, I.; Percival, C. J.; Topping, D. O. Connecting Bulk Viscosity Measurements to Kinetic Limitations on Attaining Equilibrium for a Model Aerosol Composition. *Environ. Sci. Technol.* **2014**, *48* (16), 9298–9305.

(86) Grayson, J. W.; Evoy, E.; Song, M.; Chu, Y.; Maclean, A.; Nguyen, A.; Upshur, M. A.; Ebrahimi, M.; Chan, C. K.; Geiger, F. M.; et al. The Effect of Hydroxyl Functional Groups and Molar Mass on the Viscosity of Non-Crystalline Organic and Organic–Water Particles. *Atmos. Chem. Phys.* **2017**, *17* (13), 8509–8524.

(87) Power, R. M.; Simpson, S. H.; Reid, J. P.; Hudson, A. J. The Transition from Liquid to Solid-like Behaviour in Ultrahigh Viscosity Aerosol Particles. *Chem. Sci.* **2013**, *4* (6), 2597–2604.

(88) Song, Y. C.; Haddrell, A. E.; Bzdek, B. R.; Reid, J. P.; Bannan, T.; Topping, D. O.; Percival, C.; Cai, C. Measurements and Predictions of Binary Component Aerosol Particle Viscosity. *J. Phys. Chem. A* **2016**, *120* (41), 8123–8137.

(89) Bateman, A. P.; Belassein, H.; Martin, S. T. Impactor Apparatus for the Study of Particle Rebound: Relative Humidity and Capillary Forces. *Aerosol Sci. Technol.* **2014**, *48* (1), 42–52.

(90) Bateman, A. P.; Gong, Z.; Liu, P.; Sato, B.; Cirino, G.; Zhang, Y.; Artaxo, P.; Bertram, A. K.; Manzi, A. O.; Rizzo, L. V.; et al. Sub-Micrometre Particulate Matter Is Primarily in Liquid Form over Amazon Rainforest. *Nat. Geosci.* **2016**, *9* (1), 34–37.

(91) Song, Y. C.; Haddrell, A. E.; Bzdek, B. R.; Reid, J. P.; Barman, T.; Topping, D. O.; Percival, C.; Cai, C. Measurements and Predictions of Binary Component Aerosol Particle Viscosity. *J. Phys. Chem. A* **2016**, *120* (41), 8123–8137.

(92) Sastri, S. R. S.; Rao, K. K. A New Group Contribution Method for Predicting Viscosity of Organic Liquids. *Chem. Eng. J.* **1992**, *50* (1), 9–25.

(93) Marrero-Morejón, J.; Pardillo-Fontdevila, E. Estimation of Liquid Viscosity at Ambient Temperature of Pure Organic Compounds by Using Group-Interaction Contributions. *Chem. Eng. J.* **2000**, *79* (1), 69–72.

(94) Marsh, A.; Petters, S. S.; Rothfuss, N. E.; Rovelli, G.; Song, Y. C.; Reid, J. P.; Petters, M. D. Amorphous Phase State Diagrams and Viscosity of Ternary Aqueous Organic/Organic and Inorganic/Organic Mixtures. *Phys. Chem. Chem. Phys.* **2018**, *20* (22), 15086–15097.

(95) Chenlo, F.; Moreira, R.; Pereira, G.; Ampudia, A. Viscosities of Aqueous Solutions of Sucrose and Sodium Chloride of Interest in Osmotic Dehydration Processes. *J. Food Eng.* **2002**, *54* (4), 347–352.

(96) Topping, D. O.; McFiggans, G. B.; Coe, H. A Curved Multi-Component Aerosol Hygroscopicity Model Framework: Part 2 - Including Organic Compounds. *Atmos. Chem. Phys.* **2005**, *5*, 1223–1242.

(97) Rothfuss, N. E.; Marsh, A.; Rovelli, G.; Petters, M. D.; Reid, J. P. Condensation Kinetics of Water on Amorphous Aerosol Particles. *J. Phys. Chem. Lett.* **2018**, *9* (13), 3708–3713.

(98) Marshall, F. H.; Miles, R. E. H.; Song, Y.-C.; Ohm, P. B.; Power, R. M.; Reid, J. P.; Dutcher, C. S. Diffusion and Reactivity in Ultraviscous Aerosol and the Correlation with Particle Viscosity. *Chem. Sci.* **2016**, *7* (2), 1298–1308.

(99) Mikhailov, E.; Vlasenko, S.; Martin, S. T.; Koop, T.; Pöschl, U. Amorphous and Crystalline Aerosol Particles Interacting with Water Vapor: Conceptual Framework and Experimental Evidence for Restructuring, Phase Transitions and Kinetic Limitations. *Atmos. Chem. Phys.* **2009**, *9* (24), 9491–9522.

(100) Vignes, A. Diffusion in Binary Solutions - Variation of Diffusion Coefficient with Composition. *Ind. Eng. Chem. Fundam.* **1966**, *5* (2), 189–199.

(101) Fowler, K.; Connolly, P. J.; Topping, D. O.; O'Meara, S. Maxwell–Stefan Diffusion: A Framework for Predicting Condensed Phase Diffusion and Phase Separation in Atmospheric Aerosol. *Atmos. Chem. Phys.* **2018**, *18* (3), 1629–1642.

(102) Chenyakin, Y.; Ullmann, D. A.; Evoy, E.; Renbaum-Wolff, L.; Kamal, S.; Bertram, A. K. Diffusion Coefficients of Organic Molecules in Sucrose-Water Solutions and Comparison with Stokes-Einstein Predictions. *Atmos. Chem. Phys.* **2017**, *17* (3), 2423–2435.

(103) Nga, K. L. Breakdown of Debye-Stokes-Einstein and Stokes-Einstein Relations in Glass-Forming Liquids: An Explanation from the Coupling Model. *Philos. Mag. B* **1999**, *79* (11–12), 1783–1797.

(104) Tarjus, G.; Kivelson, D. Breakdown of the Stokes–Einstein Relation in Supercooled Liquids. *J. Chem. Phys.* **1995**, *103* (8), 3071–3073.

(105) Kumar, S. K.; Szamel, G.; Douglas, J. F. Nature of the Breakdown in the Stokes-Einstein Relationship in a Hard Sphere Fluid. *J. Chem. Phys.* **2006**, *124* (21), 214501.

(106) Chen, S.-H.; Mallamace, F.; Mou, C.-Y.; Broccio, M.; Corsaro, C.; Faraone, A.; Liu, L. The Violation of the Stokes-Einstein Relation in Supercooled Water. *Proc. Natl. Acad. Sci.* **2006**, *103* (35), 12974–12978.

(107) Chenyakin, Y.; Ullmann, D. A.; Evoy, E.; Renbaum-Wolff, L.; Kamal, S.; Bertram, A. K. Diffusion Coefficients of Organic Molecules in Sucrose–Water Solutions and Comparison with Stokes–Einstein Predictions. *Atmos. Chem. Phys.* **2017**, *17* (3), 2423–2435.

(108) Price, H. C.; Murray, B. J.; Mattsson, J.; O'Sullivan, D.; Wilson, T. W.; Baustian, K. J.; Benning, L. G. Quantifying Water Diffusion in High-Viscosity and Glassy Aqueous Solutions Using a Raman Isotope Tracer Method. *Atmos. Chem. Phys.* **2014**, *14* (8), 3817–3830.

(109) Kumar, P. Breakdown of the Stokes-Einstein Relation in Supercooled Water. *Proc. Natl. Acad. Sci. U. S. A.* **2006**, *103* (35), 12955–12956.

(110) Molinero, V.; Goddard, W. A. Microscopic Mechanism of Water Diffusion in Glucose Glasses. *Phys. Rev. Lett.* **2005**, *95* (4), 045701.

(111) Zhu, L.; Cai, T.; Huang, J.; Stringfellow, T. C.; Wall, M.; Yu, L. Water Self-Diffusion in Glassy and Liquid Maltose Measured by Raman Microscopy and NMR. *J. Phys. Chem. B* **2011**, *115* (19), 5849–5855.

(112) Hopkins, R. J.; Mitchem, L.; Ward, A. D.; Reid, J. P. Control and Characterisation of a Single Aerosol Droplet in a Single-Beam Gradient-Force Optical Trap. *Phys. Chem. Chem. Phys.* **2004**, *6* (21), 4924–4927.

(113) Chylek, P.; Ramaswamy, V.; Ashkin, A.; Dziedzic, J. M. Simultaneous Determination of Refractive-Index and Size of Spherical Dielectric Particles from Light-Scattering Data. *Appl. Opt.* **1983**, *22* (15), 2302–2307.

(114) Ray, A. K.; Souyri, A.; Davis, E. J.; Allen, T. M. Precision of Light-Scattering Techniques for Measuring Optical-Parameters of Microspheres. *Appl. Opt.* **1991**, *30* (27), 3974–3983.

(115) Cai, C.; Stewart, D. J.; Reid, J. P.; Zhang, Y. H.; Ohm, P.; Dutcher, C. S.; Clegg, S. L. Organic Component Vapor Pressures and Hygroscopicities of Aqueous Aerosol Measured by Optical Tweezers. *J. Phys. Chem. A* **2015**, *119* (4), 704–718.

(116) Davies, J. F.; Wilson, K. R. Raman Spectroscopy of Isotopic Water Diffusion in Ultraviscous, Glassy, and Gel States in Aerosol by Use of Optical Tweezers. *Anal.*

Chem. **2016**, *88* (4), 2361–2366.

(117) Steimer, S. S.; Berkemeier, T.; Gilgen, A.; Krieger, U. K.; Peter, T.; Shiraiwa, M.; Ammann, M. Shikimic Acid Ozonolysis Kinetics of the Transition from Liquid Aqueous Solution to Highly Viscous Glass. *Phys. Chem. Chem. Phys.* **2015**, *17* (46), 31101–31109.

(118) Davies, J. F.; Haddrell, A. E.; Reid, J. P. Time-Resolved Measurements of the Evaporation of Volatile Components from Single Aerosol Droplets. *Aerosol Sci. Technol.* **2012**, *46* (6), 666–677.

(119) Davies, J. F.; Miles, R. E. H.; Haddrell, A. E.; Reid, J. P. Influence of Organic Films on the Evaporation and Condensation of Water in Aerosol. *Proc. Natl. Acad. Sci. U. S. A.* **2013**, *110* (22), 8807–8812.

(120) Miles, R. E. H.; Davies, J. F.; Reid, J. P. The Influence of the Surface Composition of Mixed Monolayer Films on the Evaporation Coefficient of Water. *Phys. Chem. Chem. Phys.* **2016**, *18* (29), 19847–19858.

(121) Davies, J. F.; Miles, R. E. H.; Haddrell, A. E.; Reid, J. P. Temperature Dependence of the Vapor Pressure and Evaporation Coefficient of Supercooled Water. *J. Geophys. Res.* **2014**, *119* (18), 10931–10940.

(122) Vortisch, H.; Kramer, B.; Weidinger, I.; Woste, L.; Leisner, T.; Schwell, M.; Baumgartel, H.; Ruhl, E. Homogeneous Freezing Nucleation Rates and Crystallization Dynamics of Single Levitated Sulfuric Acid Solution Droplets. *Phys. Chem. Chem. Phys.* **2000**, *2* (7), 1407–1413.

(123) Kramer, B.; Hubner, O.; Vortisch, H.; Woste, L.; Leisner, T.; Schwell, M.; Ruhl, E.; Baumgartel, H. Homogeneous Nucleation Rates of Supercooled Water Measured in Single Levitated Microdroplets. *J. Chem. Phys.* **1999**, *111* (14), 6521–6527.

(124) Stockel, P.; Vortisch, H.; Leisner, T.; Baumgartel, H. Homogeneous Nucleation of Supercooled Liquid Water in Levitated Microdroplets. *J. Mol. Liq.* **2002**, *96–7*, 153–175.

(125) Tong, H. J.; Ouyang, B.; Nikolovski, N.; Lienhard, D. M.; Pope, F. D.; Kalberer, M. A New Electrodynamic Balance (EDB) Design for Low-Temperature Studies: Application to Immersion Freezing of Pollen Extract Bioaerosols. *Atmos. Meas. Tech.* **2015**, *8* (3), 1183–1195.

(126) Hermann, G.; Zhang, Y.; Wassermann, B.; Fischer, H.; Quennet, M.; Ruhl, E. Charge Effects on the Efflorescence in Single Levitated Droplets. *J. Phys. Chem. A* **2017**, *121* (36), 6790–6799.

(127) Rickards, A. M. J.; Song, Y. C.; Miles, R. E. H.; Preston, T. C.; Reid, J. P. Variabilities and Uncertainties in Characterising Water Transport Kinetics in Glassy and Ultraviscous Aerosol. *Phys. Chem. Chem. Phys.* **2015**, *17* (15), 10059–10073.

CHAPTER 2: The Design and Characterization of a Mobile Electrodynamic Balance Apparatus

2.1 Introduction

The development of analytical instrumentation in the aerosol community over the last 20 years has enabled enormous progress toward our understanding of the physicochemical properties of individual aerosols and the chemical transformations they undergo.[1–4] Single particle capabilities such as single particle aerosol mass spectrometers,[5,6] atomic force microscopy,[7,8] micro Raman spectroscopy,[9–11] optical tweezers,[12–16] and electrodynamic balances (EDBs)[17–19] often provide complementary information because of the dynamic size ranges and specific analytical information extracted using each method. While some instrumentation is commercially available, others are developed exclusively in research laboratories and must be custom built.

A mobile EDB has been constructed, equipped to trap single, charged aerosol particles for long timescales (days) at controlled relative humidity and temperature for spectroscopic characterization. The versatile instrument platform is able to trap aerosols composed of virtually any water-soluble molecular compound and spectroscopically characterize properties such as hygroscopicity, (the uptake of water-vapor), water diffusion, and reaction kinetics.

In this chapter, the theoretical principles of electrodynamic trapping are described as an introduction to the design of the mobile EDB and the experimental setup of the apparatus. Then, the spectroscopic principles of Mie and Raman scattering are discussed, followed by a description of the optical components chosen for the experimental applications. Finally, the experimental procedure for conducting water diffusion measurements is described.

2.2 Theory and Design of a Quadrupole Ion trap

Quadrupole ion trap (QIT) mass spectrometers (MS) are used to store and non-destructively analyze charged particles defined by their mass-to-charge ratio, *m/q*. The confinement of ions in a three-dimensional quadrupole ion trap, or Paul trap[20] has been used to study molecules over wide range of sizes, from atomic ions[21,22] to micrometers.[18,23] Operated as a mass filter, QITs enable high resolution measurements of *m/q* and have become standard components in a large number of commercially available chemical analysis devices such as gas chromatography MS,[24] liquid chromatography MS,[25] and tandem MS.[26] QITs used for ion storage enable nondestructive interrogation in an environment free from solvent interactions and surface perturbations. An advantage of QITs is the ability to store particles, regardless of composition or shape, for extended periods of time, up to weeks if desired,[20] allowing the investigation of slow processes[27] and repetitive measurements[28] on the same sample.

The principle of trapping ions in a QIT is the formation of a dynamic electric potential which is experienced by the ion as time-averaged pseudo harmonic potential well with a spatially localized minimum. Figure 2.1 shows a simulated electric field, shaped as a saddle point, which oscillates with time.[29] In comparison to higher order *n*-pole traps, the equations of motion describing the time-dependent trajectory of an ion in a quadrupolar field are expressed as decoupled one-dimensional Mathieu equations:[30,31]

$$\frac{d^2u}{d\zeta^2} + \left(a_u - 2q_u cost(2\zeta)\right)u = 0 \qquad (2.1)$$

where u represents the special dimension (x, y, z), and $\zeta=\Omega t/2$ where Ω is frequency and t is time.

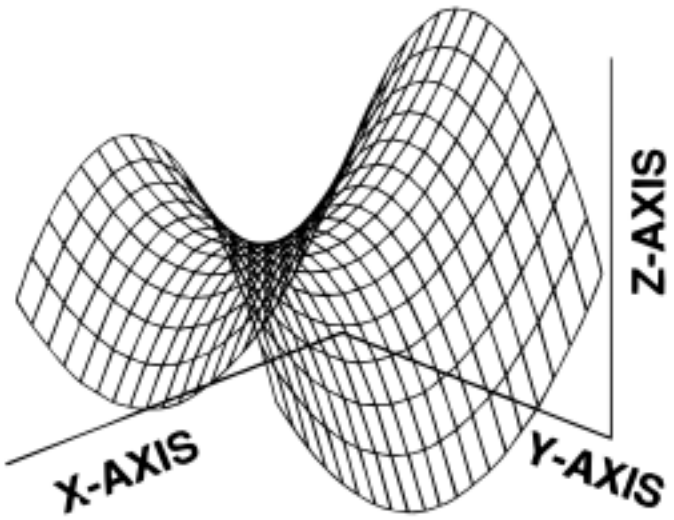

Figure 2.1 A simulation of a 3-D quadrupole field generated by a quadrupole ion trap. Adapted from March.[32]

In a quadrupole field, the electric potentential is described by:

$$\phi_{r,z} = \frac{\phi_0}{r_0^2}(r^2 - 2z^2) \tag{2.2}$$

where $x = r\cos\theta$, $y = r\sin\theta$, and $z = r$ in cylindrical coordinates, r_0, is a geometric parameter of the trap, and the electrical potential, ϕ_0, is the AC driving potential applied to hyperbolic-shaped electrodes :

$$\phi_0(t) = U_0 + V_0 \sin(\Omega t) \tag{2.3}$$

where $\Omega = 2\pi f$ and f is the frequency in Hz. The motion of the particle is described using solutions to the Mathieu differential equation 2.1 giving:

$$a_z = -\frac{8qU_0}{mz_0^2\Omega^2} \tag{2.4}$$

$$q_z = -\frac{4qV_0}{mz_0^2\Omega^2} \tag{2.5}$$

as stability parameters along the z coordinate which determine the experimental conditions for confinement. For a given AC amplitude and frequency, there are specific m/q which are bound inside of the trap and oscillate at the drive frequency where the

amplitude of oscillatory secular motion of the ion is proportional to the stability value. The effective potential, V_{eff}, experienced by an ion inside the quadupolar field is given as:

$$V_{eff} = -\frac{8qV_0}{mz_0^2\Omega^2} \tag{2.6}$$

The design of a traditional 3D QIT, invented by Wolfgang Paul for which he won the Nobel Prize in Physics in 1989,[33,34] consists of two conical electrodes, called endcaps, and a third hyberbolic-shaped ring electrode concentric with the radial symmetry axis and centered between the endcaps. In an ideal quadrupolar field the endcap electrodes are spaced by z_0, typically 0.5 – 1 cm and the inner radius of the ring is equal to $r_0 = z_0\sqrt{2}$,.

A cloud of ions may be trapped in a QIT simultaneously and repel one another due to interparticle Coulombic forces. An example of multiple particles contained in a QIT is shown in Figure 2.2 where a single particle trajectory along the AC field is visualized as a white line and the endcap electrodes are seen on the left and right of the cloud. The particles closest to the center of the trap move with the lowest amplitude motion, and particles located furthest from the center can be seen to have large amplitude motions, indicating the dependence of stability on the position inside the trap. The image also serves to highlight the difficulty in unambiguously tracking the evolution of one of the particles and the desire for trapping a single particle which, in the absence of other particles, resides in the center of the trap.

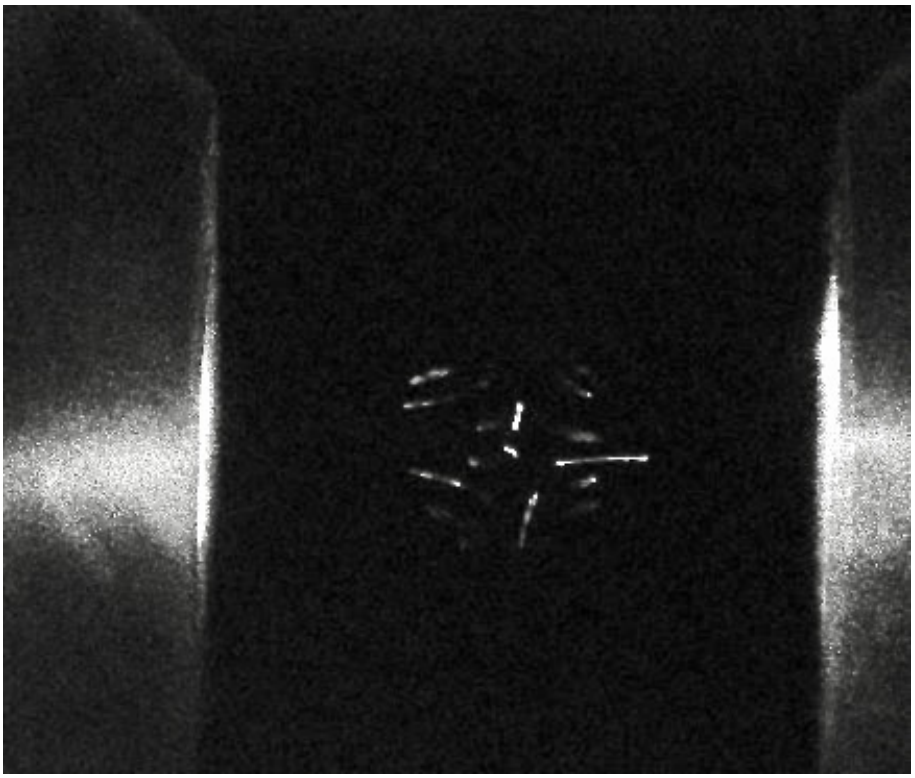

Figure 2.2. A cloud of charged particles in the center of the trap, repelling one another due to Coulombic repulsion.

In the limit of trapping heavy particles, the weight becomes sufficient to require an external force in the form of a superimposed DC potential to overcome the force of gravity and center the particle. This type of trap is called an Electrodynamic Balance (EDB) because the voltage used to balance the gravitational force is proportional to the *m/q* and can be used as a picobalance scale:[36]

$$V_{dc} = \frac{m}{qz_0^2 C} \tag{2.7}$$

where C is an empirical constant dependent on the specific geometry of the trap. EDBs have been used extensively in aerosol science because of the ability to levitate any charged particle independent of the morphology and chemical composition in a surface-free environment. Additionally, the large size of the particles analyzed in EDBs, typically >5 μm diameter, are significantly heavier than gas molecules and therefore remain stable even at atmospheric pressure. Small molecular weight ions commonly analyzed in commercial QITs are severely impacted by the presence of gas molecules and require vacuum, $< 10^{-5}$ Torr, to perform high mass resolution analysis.

The operation of EDBs at atmospheric pressure enables measurements of single aerosols undergoing physical and chemical changes in response to water vapor and other atmospherically-relevant gas phase reactants. This requires isolation of the trap from the surrounding environment followed by control of the environment as implemented in the experimental design. Nominally the trap is isolated from the laboratory using an environmental chamber, into which a select concentration of gas is introduced at a controlled concentration and flow rate. Altering the humidity inside of the trap is achieved by mixing dry air with the headspace vapor of a water bubbler, where the ratio of wet to dry air generates a select relative humidity. A large number of studies in EDBs have been conducted at room temperature, nominally 20 – 24 °C, without further temperature regulation. Adding capabilities to control the temperature far from room temperature requires thermally insulating the trap and a cooling mechanism, generally by thermalizing air prior to its introduction into the trap.

A number of electrode configurations have been used for EDB instruments, although none have been made commercially available. The electrode geometry for the mobile EDB is based on of the open-electrode configuration of Schlemmer *et al.*[37] and Trevitt *et al.*[38] The endcap electrodes, similar to the traditional Paul trap, are cones and carry the AC potential. Eight concentric rod electrodes form a cage structure around the endcaps and replace the traditional ring electrode. Six of the eight rod electrodes are electrically grounded and the remaining two, which are located vertically below the center of the trap, are used to apply DC voltage from an external power supply to maintain the droplet in the center. The electrodes are mounted in a cylindrical Macor ceramic insulator for precisely aligning and electrically isolating each electrode, as shown in Figure 2.3. The endcaps contain a 1.5 mm cylindrical channel, enabling a laser beam to pass through and serve as an alignment tool.

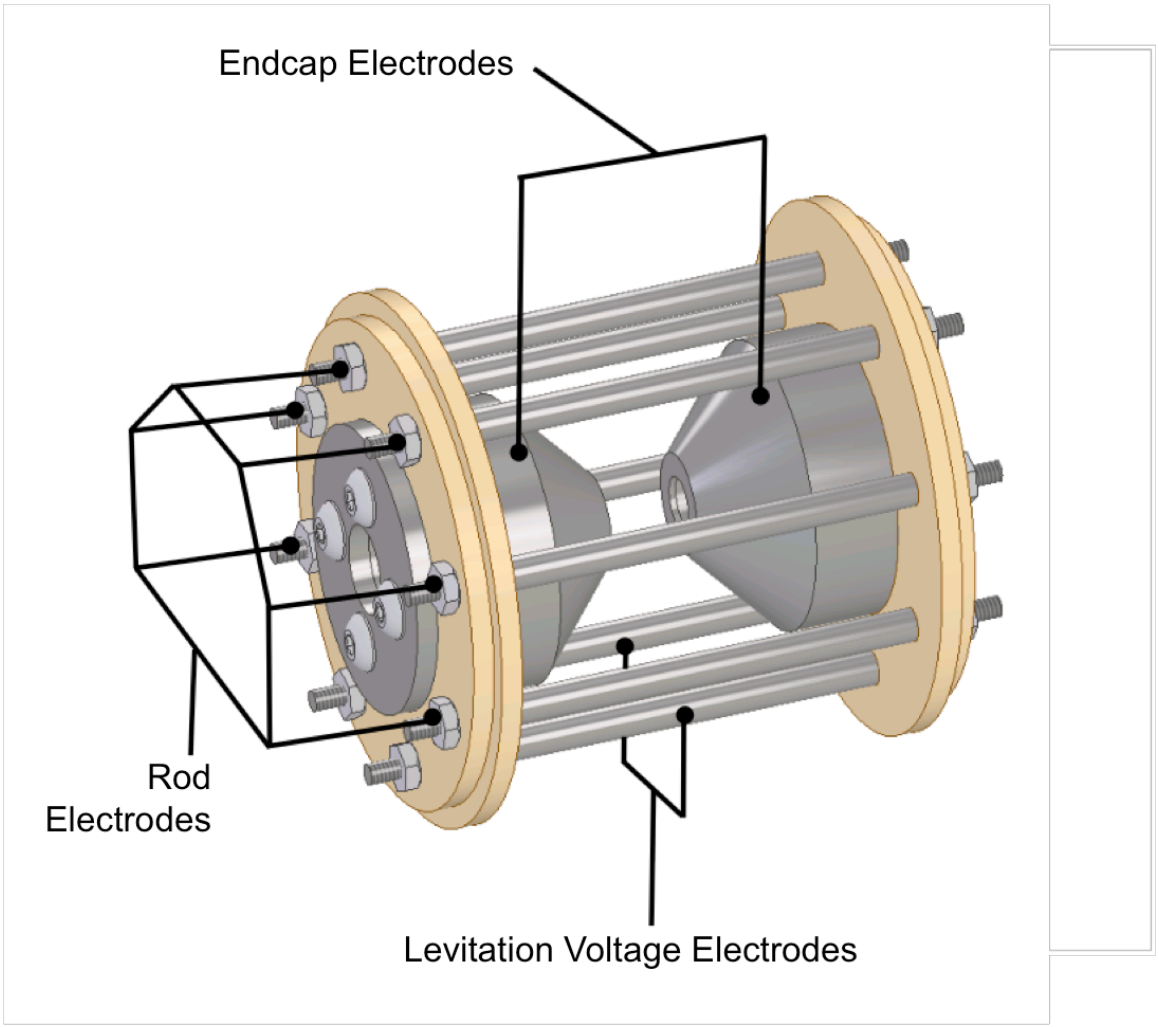

Figure 2.3. Open-electrode geometry of the mobile EDB, consisting of two conical endcap electrodes that carry AC voltage, and eight rod electrodes; two of which carry a DC levitation voltage.

The octagonal symmetry of the trap is preserved with octagonal stainless steel plates mounted to a copper standoff in thermal contact with a cryogenic cooler, shown in Figure 2.4. The stainless steel plates are outfitted with 0.5'' diameter optical windows

and lenses, and are mounted to the trap using two additional stainless steel plates to create an isolated volume within the larger chamber. An image of the actual EDB trap is shown in Figure 2.5.

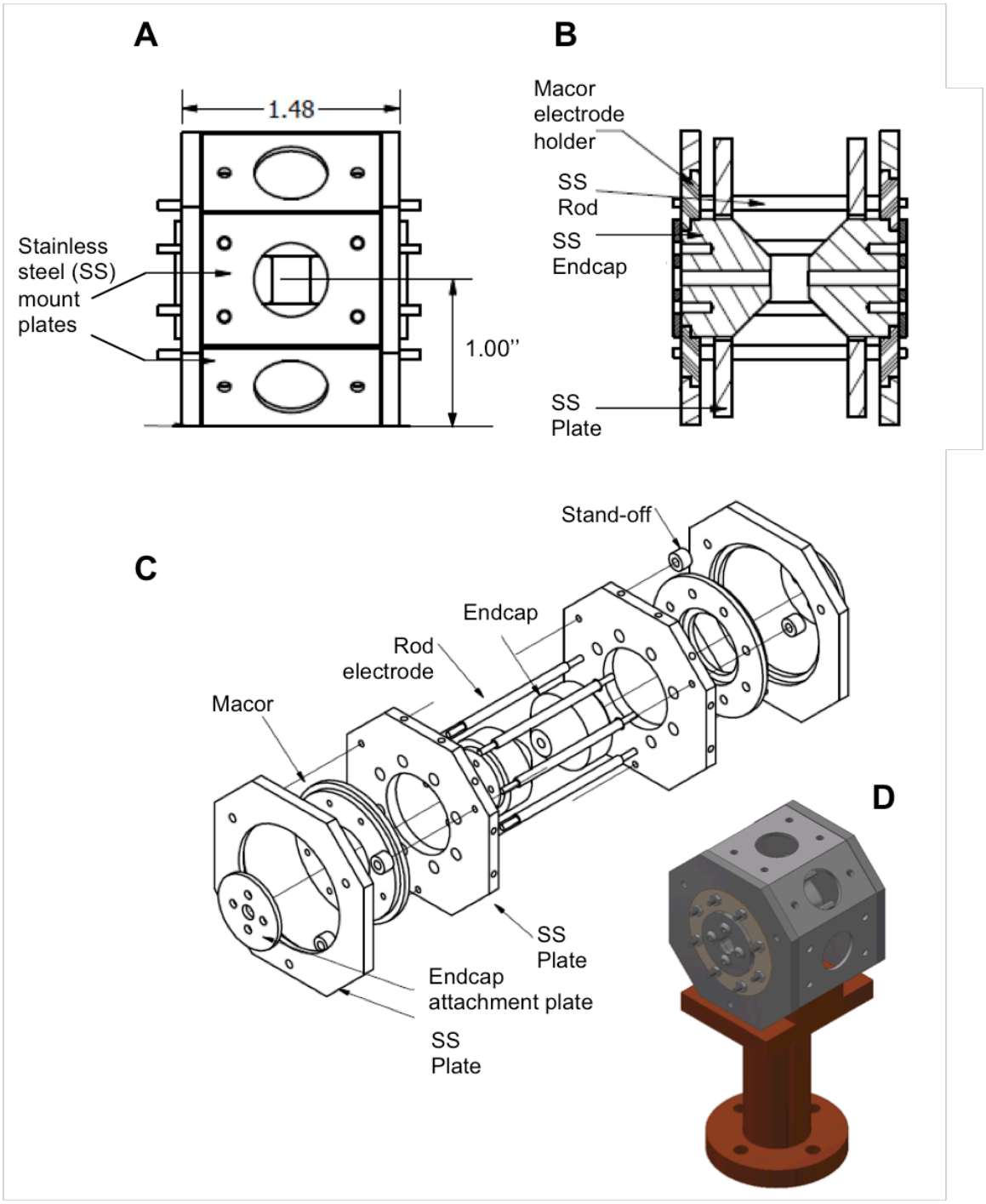

Figure 2.4. A) Mechanical drawing of a side view of the EDB trap mounting structure; B) a hatched view of (A) showing the composition of the trap; C) a projected view of the EDB components; D) A 3-D rendering of the EDB trap and the copper standoffs.

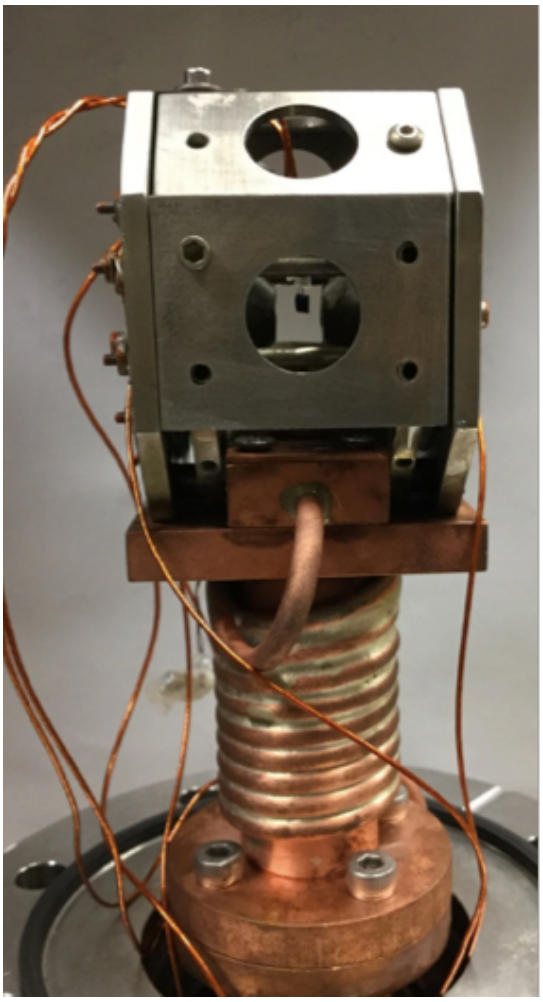

Figure 2.5. A picture of the actual mobile EDB trap removed from the environmental chamber.

Trapping a particle or droplet requires selecting AC amplitude and frequency parameters which meet the stability relationship in Equation 2.4. Inappropriate values result in the charge particle following an unstable trajectory, often ejecting axially through an endcap in a matter of seconds. The AC parameters and DC voltage for centering the particle can be used to estimate the number of charges on the particle. The surface charge density, in elementary charges/um^2 is also calculated because the charge

resides on the surface of the droplet, and studies on the influence of surface charge on properties such as crystallization suggest a strong influence if the charge density exceeds 200 elementary charges/μm^2.[39] In Chapter 3, we show that the droplets in our studies contain charge densities well below the suggested threshold necessary to impact bulk properties such as diffusion.

Centering of the particle in the center, or null point, of the trap is achieved using an automated proportional-control feedback loop. The vertical position of the droplet, P_D (pixels), is measured by fitting a Gaussian distribution to the intensity of the 1D pixel array collected using a CCD camera focused to the center of the trap. If the difference in position, ΔP, between the droplet and the experimentally determined set-point position, P_{SP}, exceeds a threshold value the DC voltage is automatically adjusted by ΔV_{dc} given by:

$$\Delta V_{dc} = C\Delta P = C(P_{SP} - P_D) \tag{2.8}$$

where C is an empirically determined constant. Figure 2.6 shows the LabView computer program designed to measure the set point and droplet positions by fitting the laser scattering from the droplet using a sing Gaussian. The feedback loop cycles at 1 Hz, optimized experimentally to minimize underdampening which causes oscillations about the set point. The centering loop enables consistent positioning of a single particle over extended periods of time, up to days.

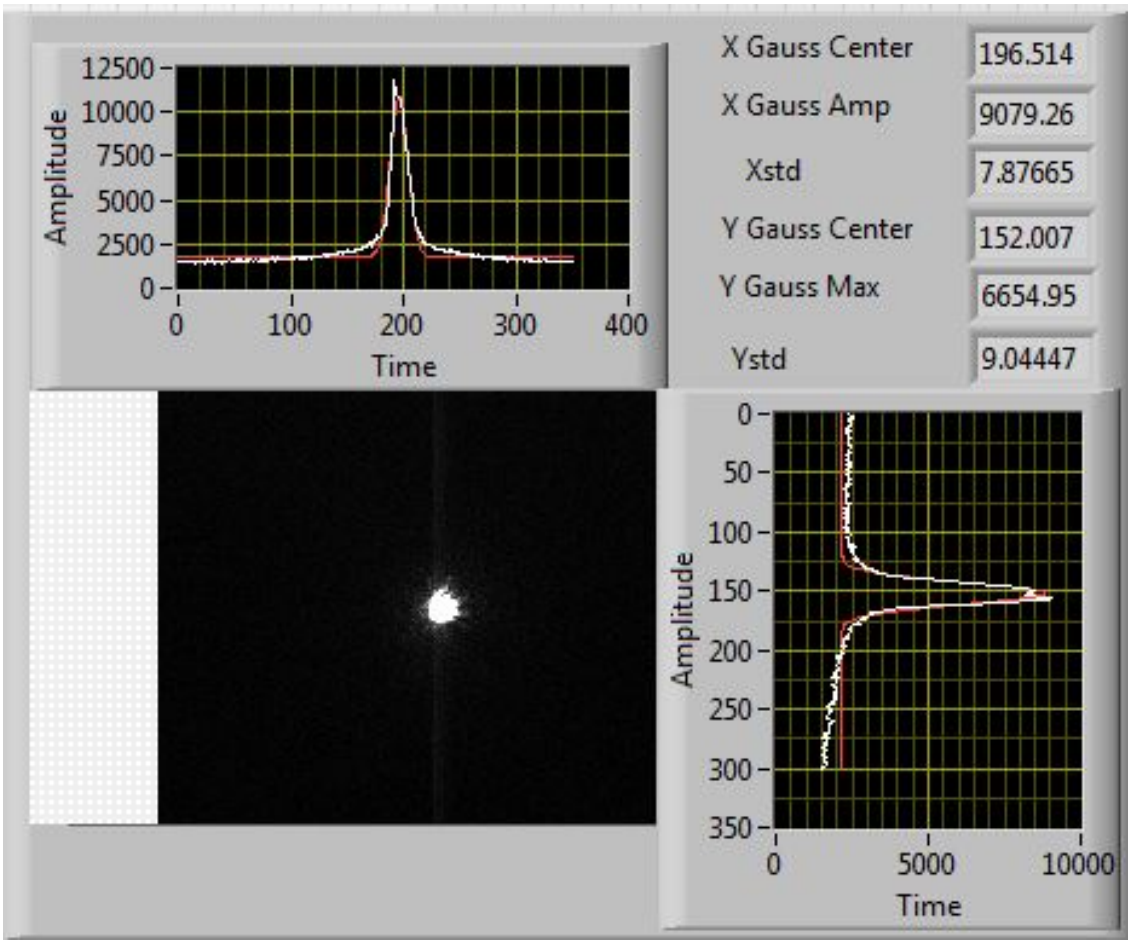

Figure 2.6. Analysis of the vertical position of the droplet in the trap is performed by collecting a CCD image and fitting a Gaussian curve to the intensity as a function of pixel location.

2.2 Environmental Control

The mobile EDB was designed for spectroscopically analyzing the physical and chemical properties of a single aerosol over time in controlled relative humidity and temperature. Custom computer software programs were created to enable instrument

control and data acquisition and enabled communication with an assortment of sensors (temperature, RH), cameras, and other electronic equipment. A schematic of the experimental setup is shown in Figure 2.7. Control of the environmental conditions was achieved by sealing off the environmental chamber from the laboratory using an electronically-actuated shutter.

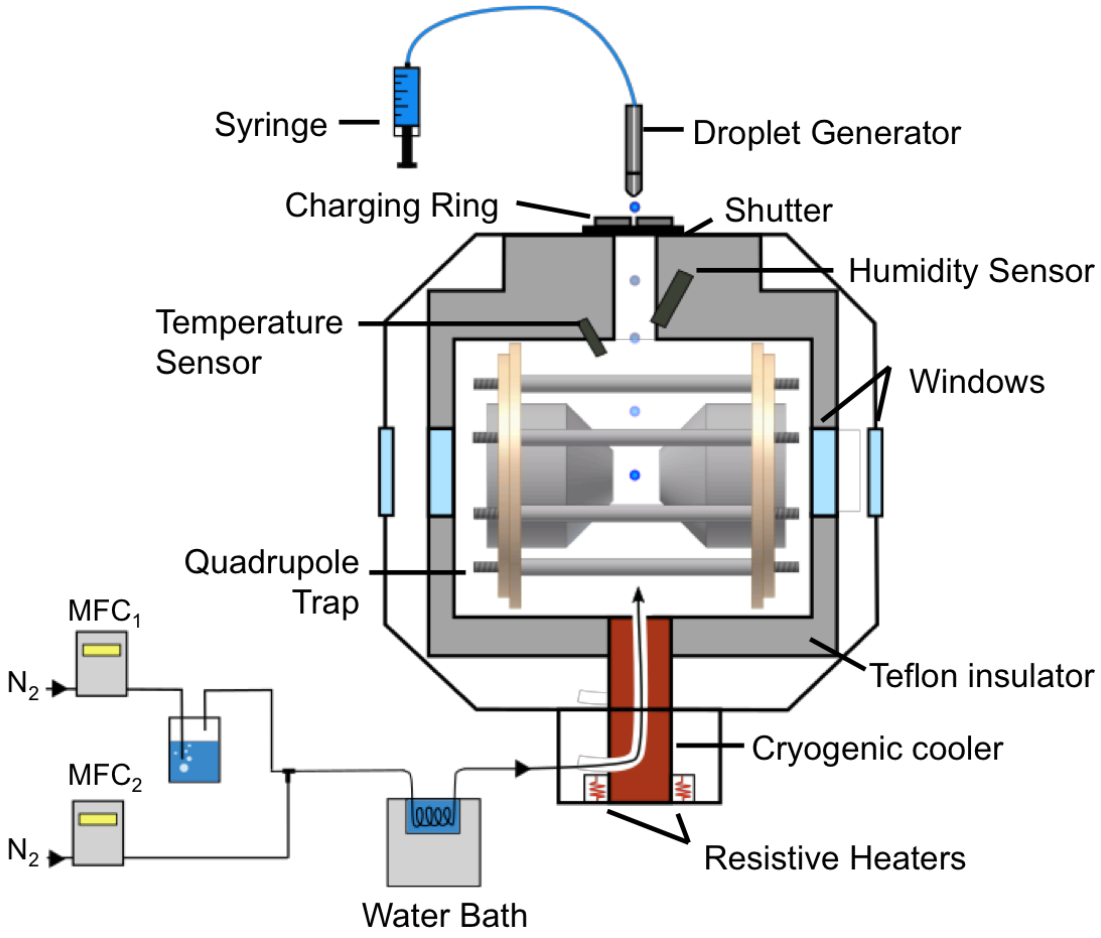

Figure 2.7. Schematic of the experimental setup of the mobile electrodynamic balance. An aqueous sample, approximately 20 μL, is aspirated into the droplet generator which produces single droplets on demand when triggered using computer software. Droplets are inductively charged using an electrostatic high voltage charging ring and injected into an enclosed chamber by opening an electronic shutter. The trapping region is insulated using a Teflon housing to reduce the volume of air subject to climate control.

The EDB is mounted inside an environmental chamber (Kimball Physics 4.5'' Spherical Cube) on a DN63CF Conflat flange equipped with electrical and gasline feedthroughs, shown in Figure 2.8. The chamber and optical boards are built onto a T-rail cart equipped with wheels, enabling the entire apparatus to be rotated or moved freely without disruption to the laser alignment. Further outfitting the apparatus for mobility, instead of using circulating water, all instrument-cooling systems were composed of electrical fans.

The primary mounting structure of the EDB is augmented with a secondary Teflon housing, shown in Figure 2.9, with the primary purpose of reducing the volume of air in the chamber required to equilibrate to the experimental RH. Additionally, the Teflon structure serves as a channel from the entrance of the chamber directly on the top face of the chamber where the droplet generation setup is located. An electrically grounded stainless steel mesh tube inside the channel prevents charging up of the material from the high voltage electrodes. A custom built electronic shutter at the chamber entrance is actuated using an Arduino servo and seals the chamber from the laboratory except when a new droplet is trapped. The high voltage AC potential is connected through the HV electrical feedthrough while the sensor connections and DC levitation voltage are made through the low voltage electrical feedthroughs.

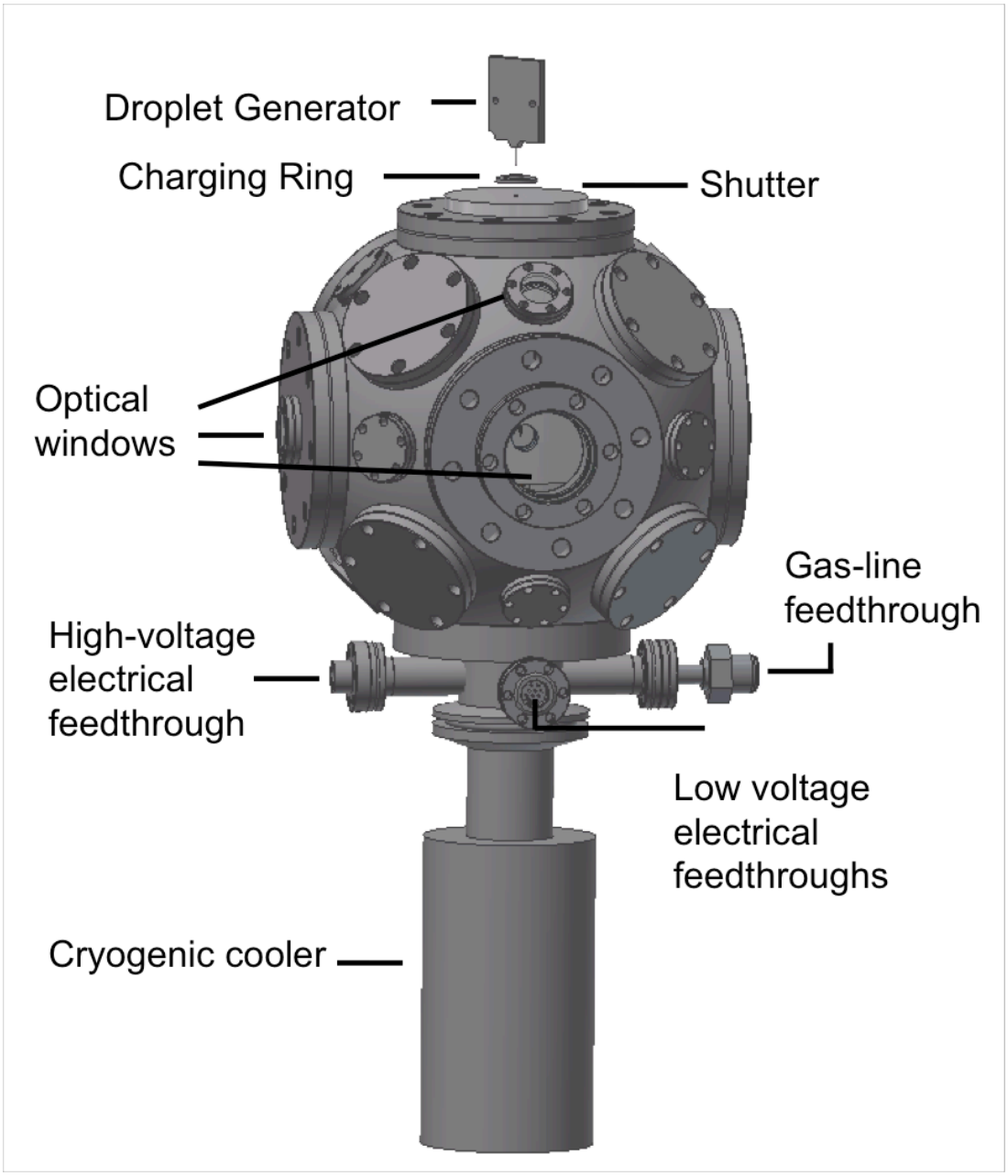

Figure 2.8. Computer-aided-design (CAD) rendering of the environmental chamber; the droplet generator and charging ring are positioned above the electronic shutter, optical windows provide spectroscopic access to the trap, and electrical and gasline feedthroughs are provided using a mini-Conflat tee.

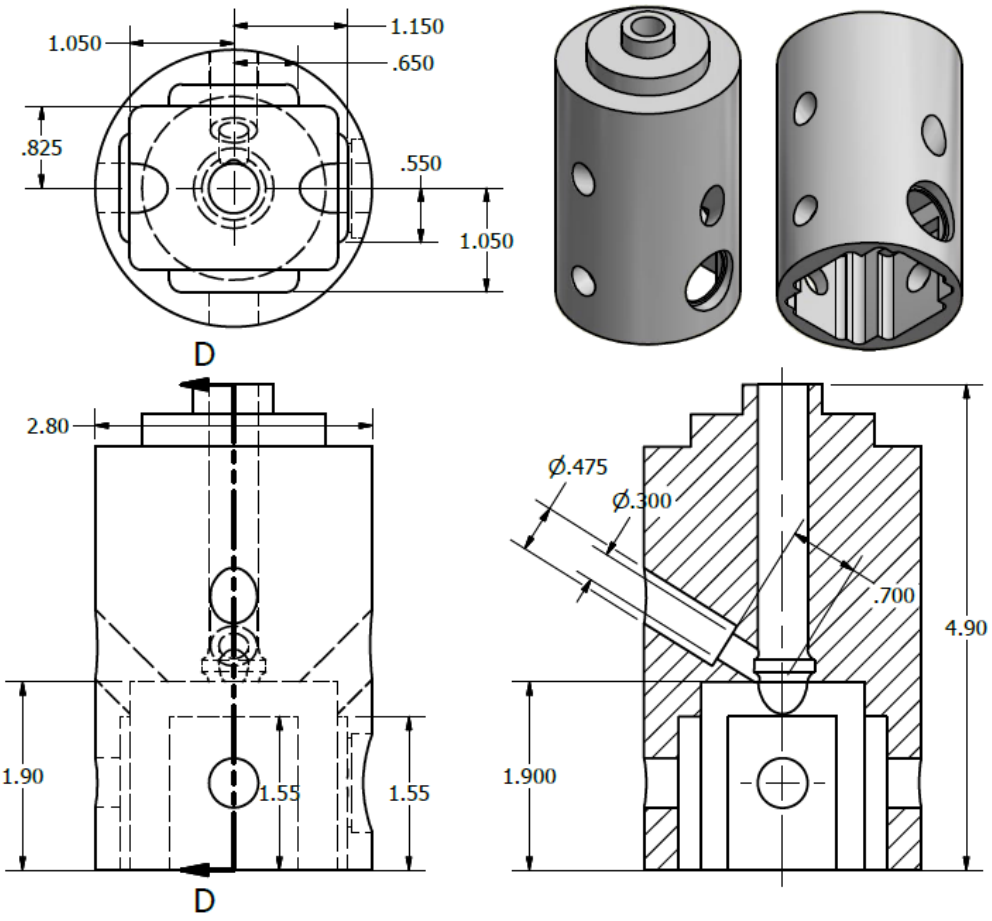

Figure 2.9. Mechanical drawing and CAD rendering of the Teflon secondary housing surrounding the primary trap housing. The structure is outfitted with optical windows, a channel for direct access between the droplet generator and trap, and mount for the relative humidity probe.

All aerosols are introduced to the EDB in the form of an aqueous droplet which are generated on demand using a piezoelectric droplet generator (Engineering Arts DE03). Aqueous solutions are prepared and filtered to remove particulate matter which

may clog the droplet dispenser. A small volume of solution (10-20 μL) is aspirated into the dispense head (45 or 67 μm fixed diameter), then a computer-controlled program signals the drive electronics to generate a pulse sequence for firing droplets into the trap. An image of the droplet generator firing a train of droplets generated from a sequence of pulses is shown in Figure 2.10. A charging ring electrode is located between the dispense head and the chamber shutter for generating a DC electric field between the ring and the grounded dispense head. As droplets are generated, the electric field induces a net electric charge to the droplet, where the polarity and magnitude of charges depends on the direction and strength of the applied field.

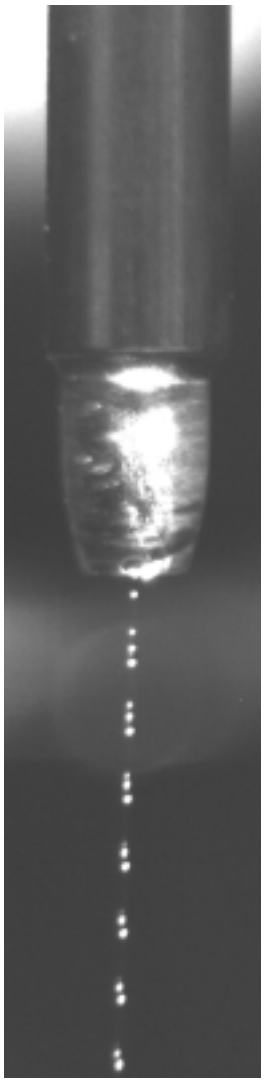

Figure 2.10. A train of droplets firing from the piezo electric droplet generator.

Droplets initially 45-67 μm in diameter equilibrate to the surrounding RH inside of the trap. The humidity is controlled using digital mass flow controllers (Alicat MC-500SCCM) to mix dry N_2 with the humidified vapor headspace of a bubbler containing water. The humidified air is subsequently directed through copper tubing wrapped around

and welded to a copper standoff in thermal contact with a Stirling free-piston coldhead cooler (Sunpower Cryotel CT) and resistive heaters which serve to maintain a constant temperature and thermalize the air before entering the trap.

Alternatively, a temperature-regulated water bath has been implemented for room temperature studies to sustain a constant temperature over long, ~ 48 hour, experimental timescales. The water bath is composed of a liquid nitrogen dewar filled with water in which two copper coils are submerged; one recirculates water through a temperature-regulated water chiller, and a the other passes the humidified air into the EDB. Characterization of the temperature regulating capabilities are shown in Figure 2.11 These measurements were recorded with the coldhead cooler maintained at 60 W allowing the temperature to reach – 40 °C as measured using a PT100 temperature sensor suspended in the null point of the trap. The humidity and temperature are measured during water diffusion experiments using a capacitive thin film polymer RH probe (Vaisala HMP60 and HMP110, ±3 % and ±1.5 % accuracy, respectively) for high stability in the range of 0 – 100 %RH and 180 – (-70) °C. The composition of the RH probe consists of three layers: an upper electrode, a thin film polymer, and a lower electrode. The capacitance is measured between the upper and lower electrode which varies as the active material, in this case a thin-film polymer, absorbs water vapor, thus changing the dielectric proportionally to the change in RH. The probe is placed into the Teflon channel approximately 25 mm above the trap where the airflow passes directly over the sensor to the exhaust.

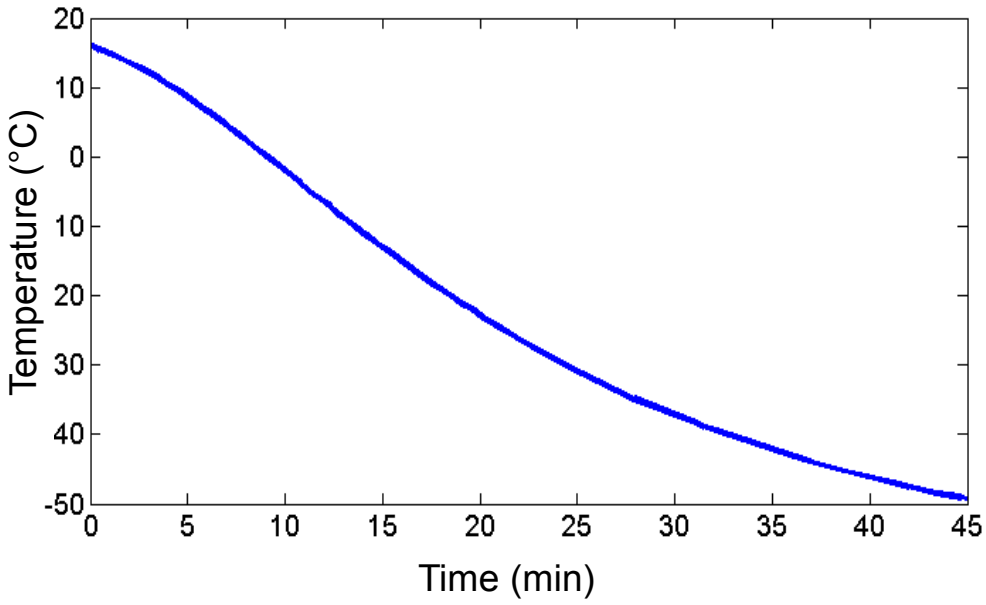

Figure 2.11. Temperature curve collected using a pt100 thermistor located in the center of the trap showing the low temperature capabilities by flowing air through copper tubing welded to a copper standoff in thermal contact with the cryogenic cooler.

During water diffusion experiments, a second bubbler filled with liquid D_2O is implemented for rapidly switching between H_2O and D_2O gas phase composition. Figure 2.12 shows a schematic of the valve system where digital mass flow controllers (MFC) regulate the N_2 flow into the bubblers and the vapor headspace is either exhausted or mixed with dry N_2. Typically during an experiment the H_2O RH is maintained in the chamber for 20-180 minutes after trapping a new droplet to ensure equilibration and the D_2O bubbler is activated for a minimum of 10 minutes prior to switching to allow intermediate flow lines to reach the set RH. This process minimizes the fluctuation in RH inside the chamber caused when the gas composition is switched.

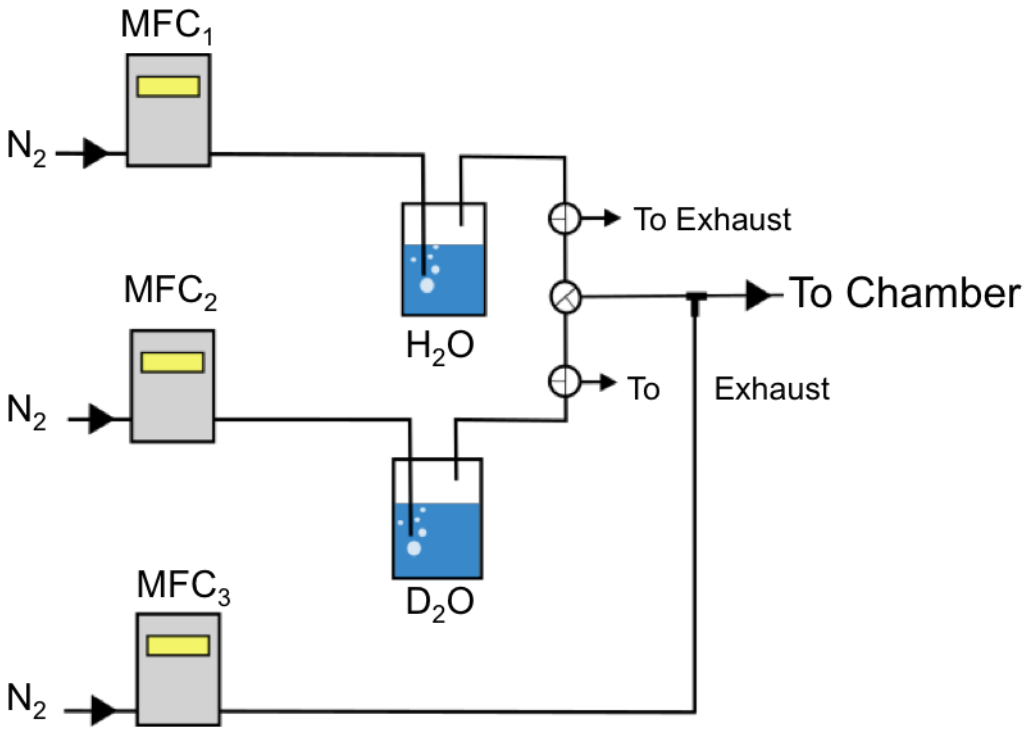

Figure 2.12. Schematic of the dual-bubbler humidity system used for D_2O isotope exchange diffusion measurements; the air flow through H_2O bubbler is first directed into the chamber as the droplet equilibrates at a given RH and then the valves are rotated to quickly replace the chamber with D_2O vapor.

A custom LabView data acquisition program controls the environmental conditions of the chamber and records settings and measurements of the trap. A CCD camera aligned to the trap acts to diagnose the presence, stability, and approximate position of a trapped droplet. On occasion multiple droplets are trapped simultaneously, experiencing repulsive Coulombic forces and oscillate along the electric field lines outside of the null point. The AC frequency is adjusted to eject all but one droplet, or to

eject all droplets and attempt to trap only a single droplet during the next cycle of droplet generation. A proportional feedback loop was programmed for automatically centering a droplet using a CCD camera as a position-sensitive detector. Unlike spectroscopic measurements of substrate-deposited particles, during which the particle is stationary in the focal point of the optical setup, the signal collection from droplet in a 3D trap is sensitive to the optical alignment. Implementation of an automated particle-centering program was vitally important for ensuring both consistent overlap of the laser beam with the trapped droplet and sufficient alignment with the collection optics and spectrometer.

2.3 Spectroscopy of levitated particles

Analysis of the physical state and chemical composition of the trapped droplet are performed using Mie and Raman spectroscopy. The optical layout is shown in Figure 2.13. A vertically polarized, frequency-doubled 532 nm YAG laser is reflected off a broadband mirror and 532 nm laser edge beamsplitter through optical windows and focused by a lens to the center of the trap. The laser power and pulse frequency are controlled with a digital controller with typical operation at approximately 200 mW and 80 kHz. The Mie elastic scattering is collected with *f/2* optics over a solid angle of 24.5 degrees centered at 45 degrees in the forward direction and passes through optical windows, a neutral density filter, and linear polarizer and detected on a 2D CCD array, with a maximum acquisition frequency of 30 Hz. Figure 2.14 shows a side view of the optical layout. The Raman scattering is collected using an *f/2* optic and passed as a plane

wave through optical windows and the 532 nm laser edge beam splitter which has a sharp transmission cut off below 532 nm. The transmitted signal is focused with a 100 mm focal length lens into a high-OH fiber optic cable composed of seven 105 μm cores for an effective core of 355 μm which are linearly arranged at the output to optimize transmission through the monochromatic entrance slit. The cable is mounted to the monochromator by means of a custom built XY optical translator which contains a 532 nm notch filter to further reject elastic scatter and a biconvex lens to focus the dispersive light exiting the fiber optic. The monochromator (Acton SpectraPro 275) is equipped with a 600 g/mm grating with a 750 nm blaze for maximum quantum efficiency in the 610-630 nm wavelength range. A thermo-electrically cooled CCD detector (2048 x 70 pixels) is mounted to the monochromator and interfaces with the LabView data acquisition program.

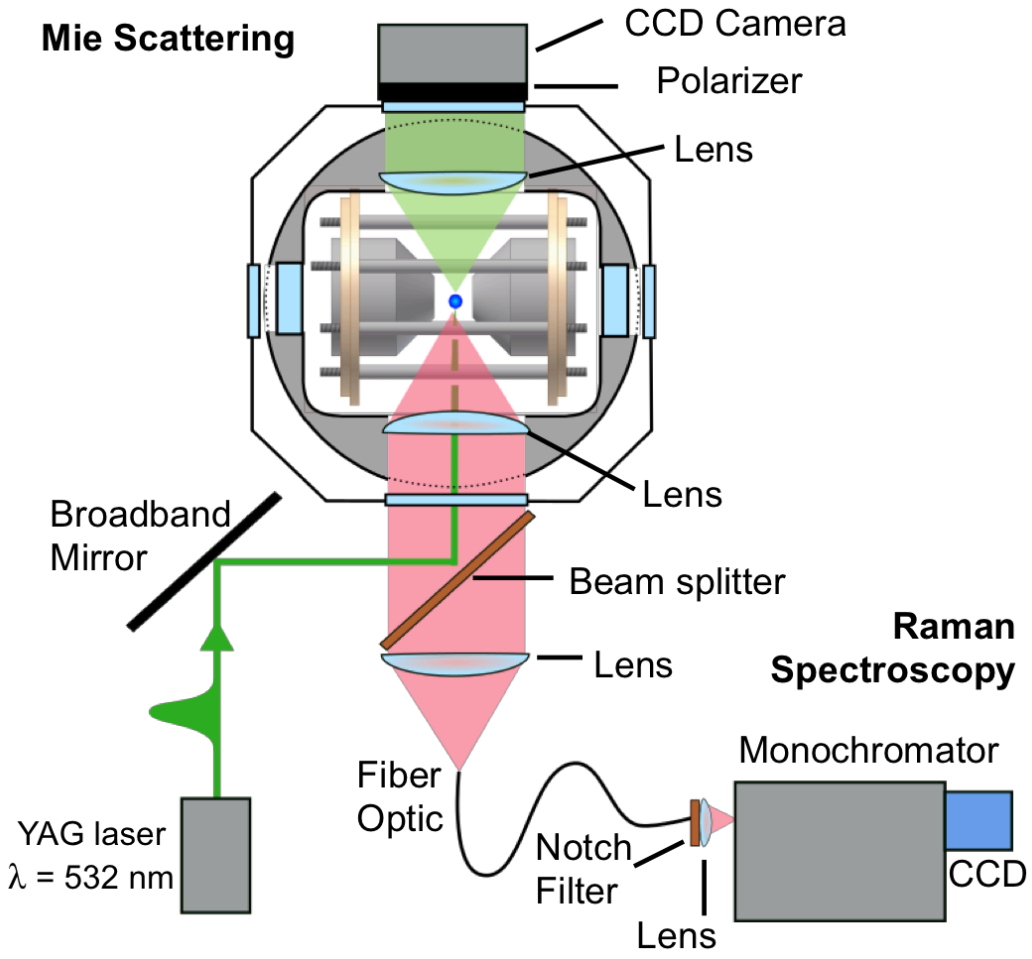

Figure 2.13. Schematic for the top view of the optical layout; the trapped particle is irradiated with an 80 kHz YAG laser focused into the trap center. The two dimensional angular elastic scattering is collected in the forward scattering direction centered around 45° relative to the laser propagation direction and recorded with a CCD camera providing size and morphology measurements. The Raman scattering is collected in the backscattering direction centered around 180° through a laser edge beam splitter and focused into a fiber optic cable mounted to a spectrometer consisting of a monochromator and CCD detector.

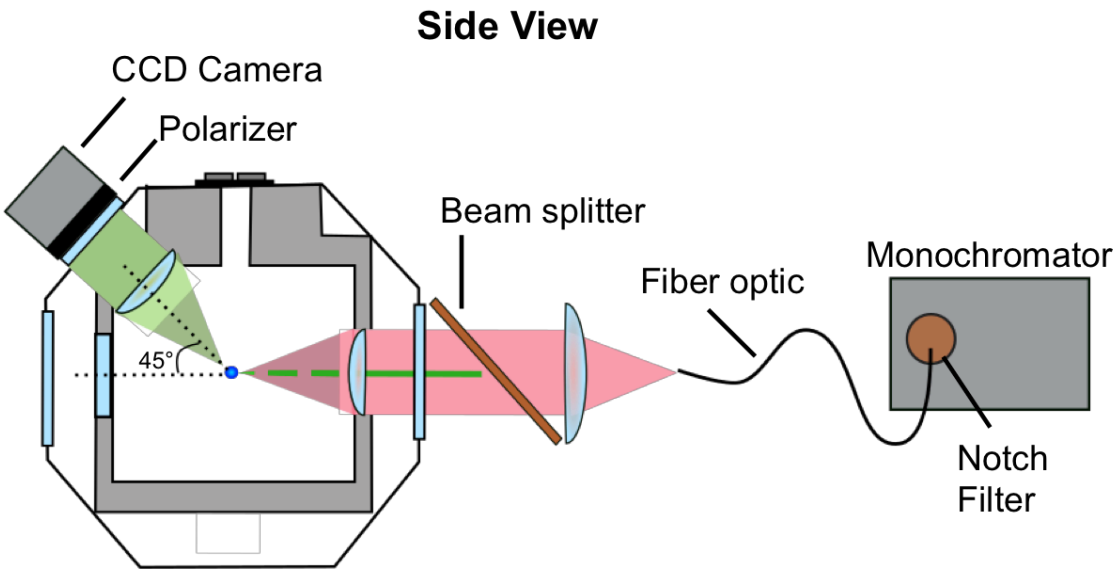

Figure 2.14. Schematic of a side view of the optical layout which shows the Mie scattering collection centered at 45° in the forward direction and the backscattering configuration for detection of the Raman scattering. The trap electrodes have been omitted for clarity and instead a centered droplet is shown.

2.3.1 Mie Scattering of single microdroplets

The morphology and size of the trapped particle are measured from the angular elastic scattering intensity spectrum. The interaction of electromagnetic light with spherical particles has been described using Mie theory.[16,40] The theory predicts the amplitude of an elastically scattered photon, I, measured at a given scattering angle, θ, with respect to the direction of the incident photon as a function of the size parameter, x. defined in terms of the radius and wavelength, $x=2\pi r/\lambda$, and the relative real part of the index of refraction of the particle to the medium, m, giving:

$$I(x,m,\theta) = \sum_{n=1}^{N} \frac{2n+1}{n(n+1)} \left[a_n(x,m)\pi_n(\cos\theta) + b_n(x,m)\tau_n(\cos\theta) \right] \tag{2.9}$$

where $a_n(x,m)$ and $b_n(x,m)$ are scattering coefficients and $\pi_n(\cos\theta)$ and $\tau_n(\cos\theta)$ are angular coefficients. A lens collects a wide solid angle of scattering, typically 20 - 30º onto a 2D CCD, and the time resolution is limited only by the frame rate of the detector, typically 30 Hz, although higher frame rate, high-speed cameras are available.

Comparison of experimental spectra with full calculations from Mie theory provide a measure of the size and refractive index to a high degree of accuracy, ± 20 nm and ± $1x10^5$ respectively.[15,16] However, achieving this level of accuracy requires well defined experimental parameters such as the scattering angle and angular resolution, and is also computationally demanding because the number of terms in the expansion of the $I(x,m,\theta)$ is proportional to x, which approaches a value of 400 when the radius exceeds 30 μm. A less computationally complex expression to describe the angular scattering intensity is desirable where applicable.

The geometric optics approximation of Mie theory is used when the size of the sphere is significantly larger than the irradiation wavelength.[41] A large sphere can be described as a small spherical lens such that a light ray hitting the sphere at an incident angle, θ_i, undergoes partial reflection and partial refraction, repeating this process at every interface for each ray that interacts with the sphere. When a ray emerges from a sphere it is characterized by the incident angle, θ_i, and the number of interfaces, N, it

encountered. However, instead of expressions as a function of the incident angle, a dependence of the intensity on the scattering angle is more desirable. It was determined that for large spheres, $x>10\lambda$, greater than 91% of the total scattering intensity is contained in the forward scatter, and greater than 99.5% of the forward scattering is contained for $N = 1$ and $N = 2$. These come from the rays reflected at the first interface and the rays that emerge from the second interface after refraction through the first interface. Using the assumption that the entire scattering intensity may be described only using the first two terms of the summation over N, the expression can be converted to one that is expressed in terms of the scattering angle as opposed to the angle of incidence. A comprehensive description of the derivation has been discussed previoiusly.[40,41] Shown in Figure 2.15 are theoretical simulations of the scattering intensity as a function of angle comparin the result fromMie theory and the geometrical optics approximation for (A) a 10 μm water droplet and (B) 50 μm water droplet. There is excellent agreement of the geometrical optics approximation with Mie theory at small scattering angles, or those approaching the forward scattering direction, and as the size parameter x is very large.[42]

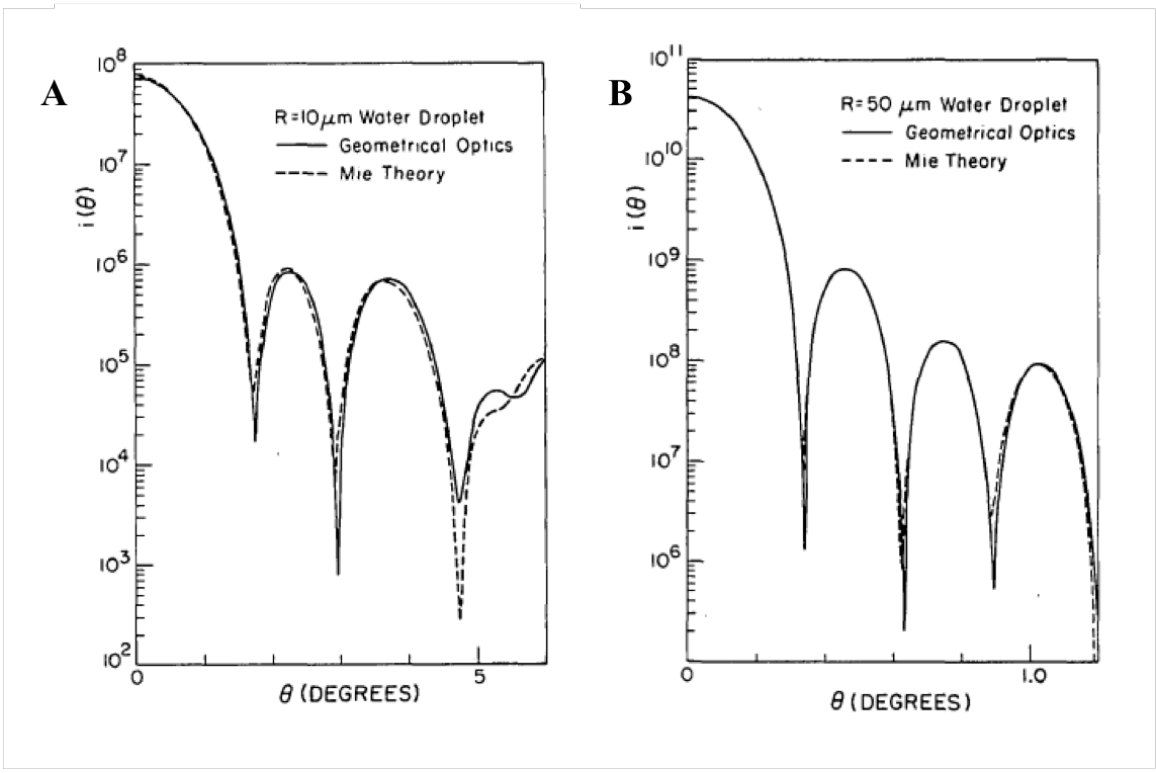

Figure 2.15. Comparison of the Geometrical Optics approximation with Mie Theory for the scattering intensity, i(*θ),* with scattering angle, *θ (Degrees),* for A) a water droplet with a radius of 10 μm and B) a water droplet with a radius of 50 μm. Adapted from *Glantschnig et al.*[41]

A useful consequence of the geometrical optics approximation is the agreement of the positions of the peaks and troughs with Mie theory. The undulations are evenly spaced and the angular spacing between successive maxima, Δθ, is inversely proportional to the droplet radius given by:[41]

$$r = \frac{\lambda}{\Delta\theta}\left(\cos\left(\frac{\theta}{2}\right) + \frac{n\sin\left(\frac{\theta}{2}\right)}{\sqrt{1+n^2-2n\cos\left(\frac{\theta}{2}\right)}}\right)^{-1} \quad (2.10)$$

where λ is the laser wavelength (μm) and θ is the median scattering angle (rad). Figure 2.17 shows an example scattering image collected on the CCD of a trapped sucrose-water droplet at 42 %RH. The image consists of a 2D array of intensity values that are sliced and summed along the vertical coordinate of the image to produce the intensity spectrum as a function of scattering angle. The angular intensity spectrum is processed by a fast Fourier transform (FFT) where the maxima in frequency space corresponds to the average peak spacing. The inset of Figure 2.17 shows the corresponding frequency spectrum. The computational processing of the spectra via FFT is computationally less demanding compared to full Mie theory calculations, allowing for a nearly *in situ* real-time size calculation of a trapped droplet, provided the index of refraction is known. The geometrical optics approximation has been used to measure the size of suspended single particles in a number of studies including measurements of homogeneous ice nucleation, evaporation rates, hygroscopicity, and heterogeneous reaction kinetics. The FFT processing can achieve an accuracy of ± 100 nm for droplets.[43]

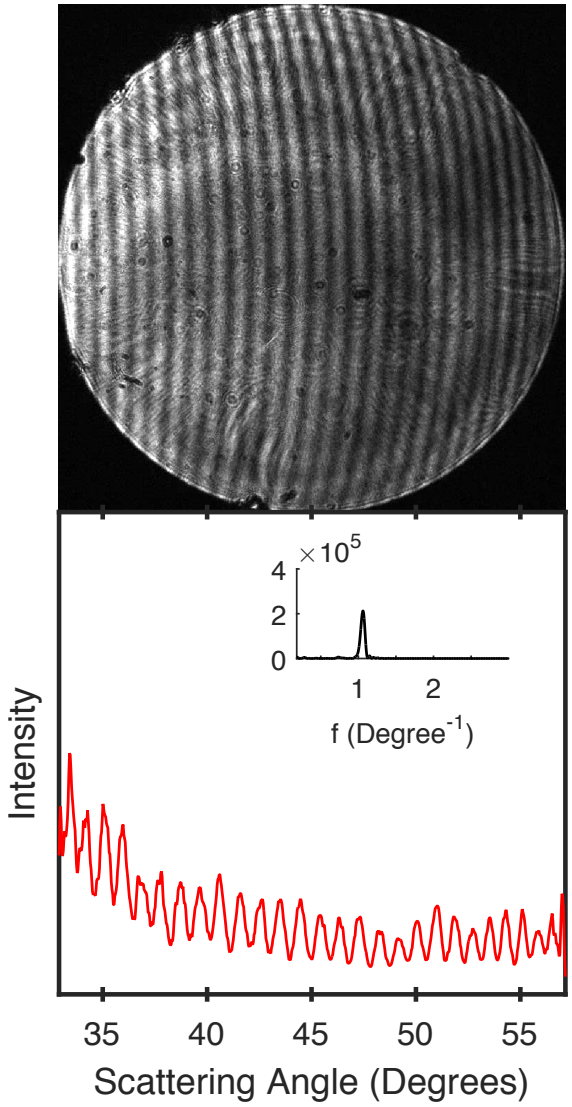

Figure 2.17. A Mie image (upper) of a trapped sucrose water droplet at 42 %RH, angular intensity spectrum (lower) and FFT frequency spectrum (inset) of the intensity spectrum where the sharp maximum is equal to the average angular spacing between successive bands in the image and maxima in the angular intensity spectrum.

Sizing of a trapped droplet *via* the geometric optics approximation requires conversion from CCD pixels to scattering angle. Calibration of the scattering angle was

performed using polystyrene latex spheres (PSLs) of known size and refractive index. Diluted aqueous/methanol solutions were prepared from the stock concentrated PSL solutions (Polysciences) which were aspirated into the droplet dispenser for firing droplets containing PSLs into the EDB and allowing the water to evaporate leaving behind a single suspended PSL. The PSL scattering angle calculations compiled into a calibration curve are used to compute the radius from equation 2.10 from any droplet, provided the index of refraction is known or can be calculated. The calibration with PSLs is used to determine the value of the solid angle collected by the yielding a conversion factor from pixels in the CCD array to scattering angle.

The index of refraction is parameterized as a function of mass fraction solute because the concentration of a droplet changes as evaporation or condensation of water occurs as a function of the surrounding RH. The dependence of MFS on water activity, a_w, has been well studied for sucrose solutions and the treatment by Norrish[44] has been shown to correlate with experimental measurements over the entire RH range:

$$a_w = x_w \exp(k x_s^2) \tag{2.11}$$

where x_w and x_s are the mole fractions of water and solute, respectively, and k is an empirical constant equal to -6.47 for sucrose.[45] The density of sucrose as a function of mass fraction is calculated from the empirical parameterization from Cai et al.:[46]

$$\rho_s = a + b_1 MFS + b_2 MFS^2 + b_3 MFS^3 \tag{2.12}$$

where a = 0.9982, b_1 = 0.02974, b_2 = 0.20386, and b_3 = 0.30992. The mole fraction, mass fraction, and density of NaCl-water and $CaCl_2$-water were calculated using the Extended Aerosol Inorganic Model (E-AIM)[47,48] and Aerosol Inorganic-Organic Mixtures Functional groups Activity Coefficients (AIOMFAC)[49,50] respectively. The density of a ternary mixture can be taken as the volume additivity of components, with the pure component density of water, $\rho = 1000\ kg \cdot m^{-3}$, and sucrose,[46] $\rho = 1541.7\ kg \cdot m^{-3}$ giving:

$$\frac{\mathbf{1}}{\boldsymbol{\rho_{mix}}} = \sum_{\boldsymbol{i}} \frac{\boldsymbol{\phi_i}}{\boldsymbol{\rho_i}} \tag{2.13}$$

where ϕ is the mass fraction of the component. The effective index of refraction for the mixture is calculated using the linear molar refraction mixing rule:[46]

$$n_{eff} = \sum_i x_i n_i \tag{2.14}$$

in which x_i is the mole fraction and n_i is the refractive index for each component taken as 1.33 for water and 1.558 for sucrose.[46] The calculated index of refraction of the mixed component droplet at a given RH is then used in Eqn (2.2) to calculate the droplet diameter. Applications to ternary mixtures are further discussed in Chapter 4.

2.3.2 Raman Spectroscopy of trapped aerosol

Raman spectroscopy provides information on the molecular vibrations in a sample through nondestructive inelastic scattering of electromagnetic radiation. The Raman spectrum gives a molecular fingerprint, observed as peaks commensurate with the

vibrational modes of the molecules. The modes must have a non-zero time-dependent polarizability in the interaction with polarized monochromatic light to give rise to an inelastically scattered photon, described as the Raman effect. Assuming molecular vibrations are described as harmonic oscillators, a reasonable assumption for low-lying vibrational states occupied at room temperature, the solution to the Schrödinger equation gives rise to equally spaced quantized vibrational energy levels:

$$E_\nu = \left(\nu + \tfrac{1}{2}\right) h\upsilon_0 \tag{2.15}$$

with quantum numbers ν = 0, 1, 2,... and allowed transitions occurring between neighboring states Δν = ±1. A molecule consisting of N atoms has 3N – 6 vibrational degrees of freedom, 3N –5 for linear molecules, corresponding to a set of independent normal modes, Q_i. A normal mode is defined as a vibrational motion where each atom is displaced from its equilibrium position by a vector not necessarily defined by a bond coordinate, the center of mass remains fixed during the vibration, and all the atoms move in-phase. Using Hooke's law it follows that the time-dependent displacement in a normal mode is equal to:

$$Q_k(t) = Q_{k,0} cos\ (2\pi\nu_0 t) \tag{2.16}$$

and the characteristic normal mode frequency is:

$$\upsilon_0 = \frac{1}{2\pi}\sqrt{\frac{k}{\mu}} \tag{2.17}$$

where k is the force constant and μ is the reduced mass of the vibrating atoms. The frequency is typically reported in wavenumber, $\tilde{\nu} = \upsilon/c$ and c is the speed of light.

Monochromatic light of frequency ω_i interacting with the electron density of a molecule gives rise to an induced dipole :

$$\mu_{ind}(t) = \alpha E(t) = \alpha E_0 \sin(2\pi\omega_e t) \tag{2.18}$$

and the polarizability depends on the bond length displaced from the equilibrium value, x_0:

$$\alpha(t) = \alpha_0 + \left(\frac{d\alpha}{dQ_k}\right) Q_k + \cdots \tag{2.19}$$

Together the induced dipole is now expressed in the form:

$$\mu_{ind}(t) = E_0 \sin(2\pi\omega_e t) + \left(\frac{d\alpha}{dQ_k}\right) A E_0 [\cos(2\pi(\omega_e + \upsilon_0)t) + \cos(2\pi(\omega_e - \upsilon_0)t)] \tag{2.20}$$

This leads to the time-varying dipole scattering of light at the same frequency as incident light, shown in Figure 2.17, as elastic Rayleigh scattering, and at frequencies equal to $\omega_e + \upsilon$ and $\omega_e - \upsilon$, called Stokes and anti-Stokes scattering, respectively. For a molecular vibration to lead to inelastic scattering, the polarizability vector along a normal coordinate must be non-zero.[51]

$$\frac{d\alpha}{dQ_k} \neq 0 \tag{2.21}$$

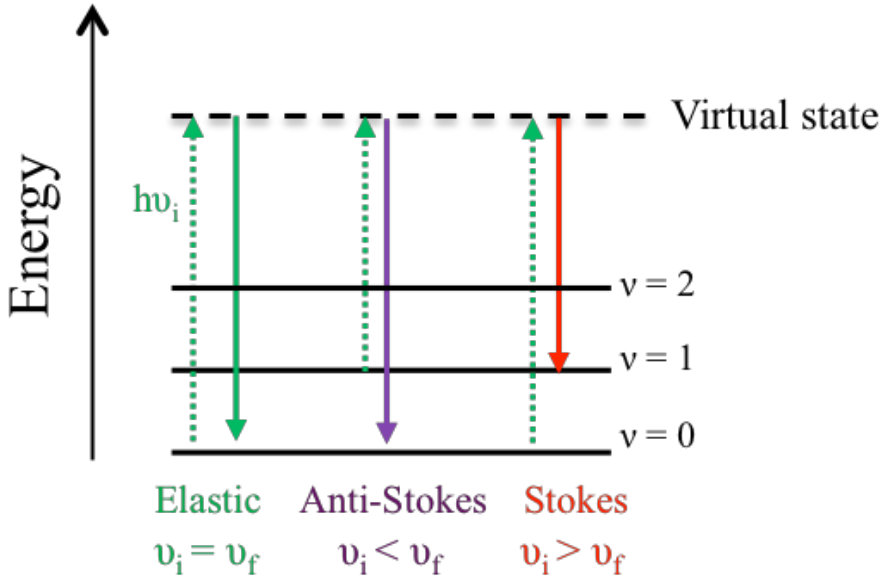

Figure 2.17 Schematic representation of the energy transitions in Raman spectroscopy; the dotten green line represents the energy of the laser and the resulting scattering may be of equal energy (elastic), greater energy (Anti-Stokes), or lower energy (Stokes).

Experimentally, the inelastically scattered photons are detected using a spectrometer measuring peaks corresponding to normal mode frequency used to identify a molecular species in the sample. The energy transitions of Raman scattering occur at vibrational levels higher and lower than the incident light, as shown in Figure 2.18 where scattering without a change in energy is elastic, and inelastic scattering at discrete values equivalent to vibrations higher and lower are termed Stokes and anti-Stokes, respectively.

For linear Raman scattering, the number of scattered photons per second, N_R (s^{-1}) collected over a solid angle $\Delta\Omega$ is given by:

$$N_R = \left(\frac{\partial\sigma}{\partial\Omega}\right)\Delta\Omega\,\frac{I_0}{h\omega}(N)(S)(L) \tag{2.22}$$

where I_0 ($W\cdot cm^{-1}$) is the laser irradiance, ($\partial\sigma/\partial\Omega$) is the Raman scattering cross-section ($cm^2\cdot sr^{-1}$), ω is the laser frequency (s^{-1}), N is the number density of molecules ($molec\cdot cm^{-3}$), S is the beam cross section (cm^2), and L is the interaction length (cm). For example, the vibrations of bulk H_2O give rise to Raman features at 1650 cm^{-1} for the bend, 686 cm^{-1} libration mode, and a broad OH stretch with a maximum of ~3480 cm^{-1}.[4,52]

The optical layout for collection of Raman spectroscopy was designed using a 532 nm laser and collection of inelastic scattering in the 550-700 nm wavelength range allowing measurement of Stokes Raman features shifted by 500 – 4000 cm^{-1}. The apparatus is outfitted with optical windows composed of N-BK7 optical glass or S1-UV fused silica with high transmission (>90 %) in the 200-1200 nm wavelength range. A 532 nm laser edge beamsplitter (Semrock Razor Edge dichroic) behaves as a reflective mirror to the laser and a high transmission window for wavelengths greater than 532.5 nm when aligned at 45°. This configuration enables collection of the high intensity backscattered light as compared to the lower intensity scattering at 90°. A 12.7 mm diameter S1-UV lens with a focal length of 25 mm (*f/2*) both focuses the laser beam and collimates the inelastic back scatter over a solid angle of approximately 28°. The collimated

backscattered light passes through the laser edge beamsplitter and is focused by at 25.4 mm diameter lens with an anti-reflective coating into the six cores of a fiber optic cable arranged in a circular cluster. The exit of the fiber cable rearranges the six cores into a line for high transmission through the slit of a spectrometer. A custom optical mount aligns the fiber with a 532 nm notch filter and a biconvex lens to focus the signal into the monochromator. A 600 g/mm grating with a 750 nm blaze is used for high quantum efficiency in the 600 – 650 nm wavelength range, a linear dispersion of 150 nm, and spectral resolution of 10 cm^{-1}. An open-electrode thermo-electrically cooled CCD detector (Horiba Syncerity) is mounted to the monochromator and was calibrated using fluorescent and helium lamps with well-characterized spectra. The CCD suffers from a large noise associated with analog readout from the CCD electronics to the computer, which is accounted for in the data processing procedure by subtracting the baseline noise from an acquired spectrum. A long integration time, typically 30 – 120 s for each spectra leads to high signal-to-noise for resolving characteristic peaks in the Raman spectrum rather than averaging over multiple spectra collected with a lower exposure time.

The data acquisition and control are carried out using custom built LabView programs which interface with the devices associated with the EDB apparatus. The instrument control panel displays critical environmental parameters such as temperature, humidity, levitation voltage, and cryocooler power. The spectroscopy control interface displays the Mie and Raman spectra and records raw spectra for post-processing of the size and chemical analysis. Example displays of the LabView programs for instrument control and spectroscopic collection are found in Appendix A.

2.4 Diffusion measurements in single aerosol

Measurements of the diffusion coefficient of water are performed on binary and ternary mixtures in single charged microdroplets by tracking the evolution of the *ν*(O-D) and *ν*(O-H) Raman peaks corresponding to D_2O diffusing into the droplet and isotopically replacing H_2O. Experiments are carried out at constant RH by first trapping a single sucrose droplet in H_2O RH and allowing sufficient time for equilibration. Then D_2O vapor at the same RH is introduced to the chamber, replacing the gas-phase H_2O in the trap and eventually diffusing into the droplet to replace the H_2O. During each experimental run the H_2O humidified air is initially directed into the chamber for droplet equilibration while the D_2O bubbler is exhausted to fill intermediate tubing lines, reducing changes in RH during the gas transition in the trap. When the chamber atmosphere is switched to D_2O the humidity probe measurement must be corrected for the difference in equilibrium vapor pressure of D_2O versus H_2O[53] as shown in Eqn (1) where A = -0.30661, B = 9.14056, and C = 75.753 and T is in Celsius.

$$ln\left(\frac{p^0_{H_2O}}{p^0_{D_2O}}\right) = A + \frac{B}{C+T} \tag{2.23}$$

Since the total amount of sucrose is constant throughout each experiment all spectra are normalized to the sucrose ν(C-H) peak at 2900 cm^{-1}, allowing for correction for fluctuations in spectral intensity due to low amplitude motions of the droplet in the laser beam. The spectrum between 2000 – 3800 cm^{-1} is modeled with a seven or eight

term summation of Gaussians is applied to the spectrum to determine individual peak contributions and therefore calculations of relative abundances of chemical species present. Up to two Gaussians contribute to the O-D band, two Gaussians to the C-H stretch, one Gaussian to the weak C-H overtone peak, two Gaussians to the O-H band, and a weak, broad Gaussian accounts for background signal. Figure 2.18 shows the contributions of the seven Gaussians for an example Raman spectra of a sucrose droplet approximately halfway through an isotope exchange experiment when distinct peaks from both H_2O and D_2O are present. The integrated intensity of these features allows calculation of the fractional concentration of D_2O in the sucrose droplet over time.

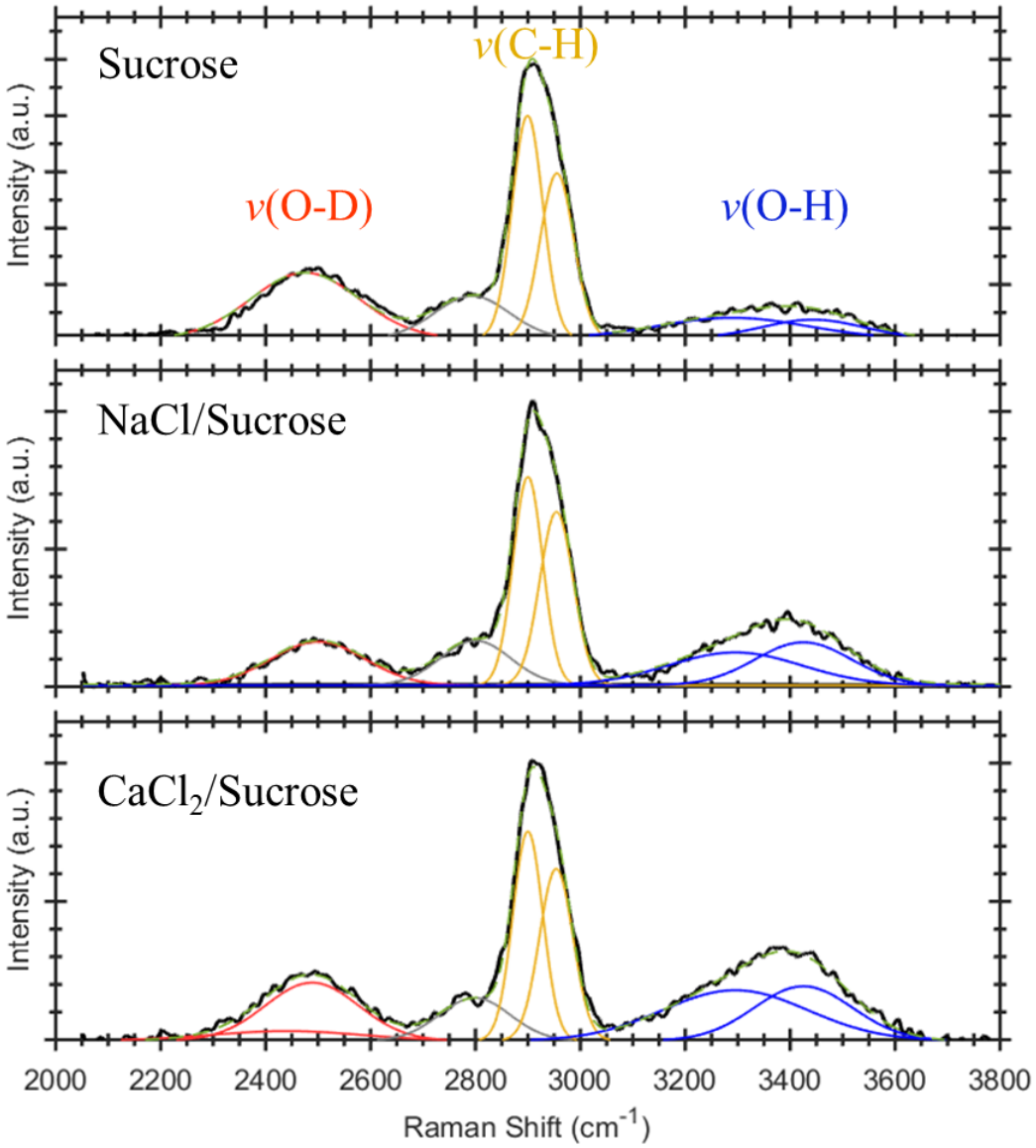

Figure 2.18. Raman spectra collected of single (A) sucrose, (B) 1:1 sucrose-NaCl, and (C) 1:1 sucrose-$CaCl_2$ droplets undergoing H/D isotope exchange which are deconvoluted using a series of Gaussian fits as shown individually and as the summation.

The intensity of the features corresponding to H_2O and D_2O are calculated from the Gaussian fits and used to calculate the fractional concentration of D_2O in the droplet:

$$\phi_{OD} = \frac{A_{OD}}{A_{OD} + \frac{1}{\sqrt{2}} A_{OH}} \tag{2.24}$$

where the O-D stretch located at 2500 cm^{-1} has a lower integrated intensity by a factor of $1/\sqrt{2}$ based on the difference in reduced mass.[54] During an experiment when the gas manifold valves are rotated to switch from H_2O to D_2O there is a time delay until the chamber is sufficiently filled with D_2O and the isotope exchange begins. Figure 2.19 shows the concentration fractions of D_2O and H_2O at 44% RH that are initially constant as the droplet equilibrates and then abruptly change from baseline values. It can be assumed that for a period of time, which is longer at lower humidities, the droplet is undergoing isotope exchange while the chamber atmosphere is a mixture of H_2O, HOD, and D_2O. During this time the vapor-liquid interface does not meet the condition that the gas-phase concentration of D_2O is constant, assumed by the diffusion model derived from Fick's second law. We therefore introduce a systematic approach for determining when constant D_2O RH is reached by fitting the time-dependent fractional concentration of OD

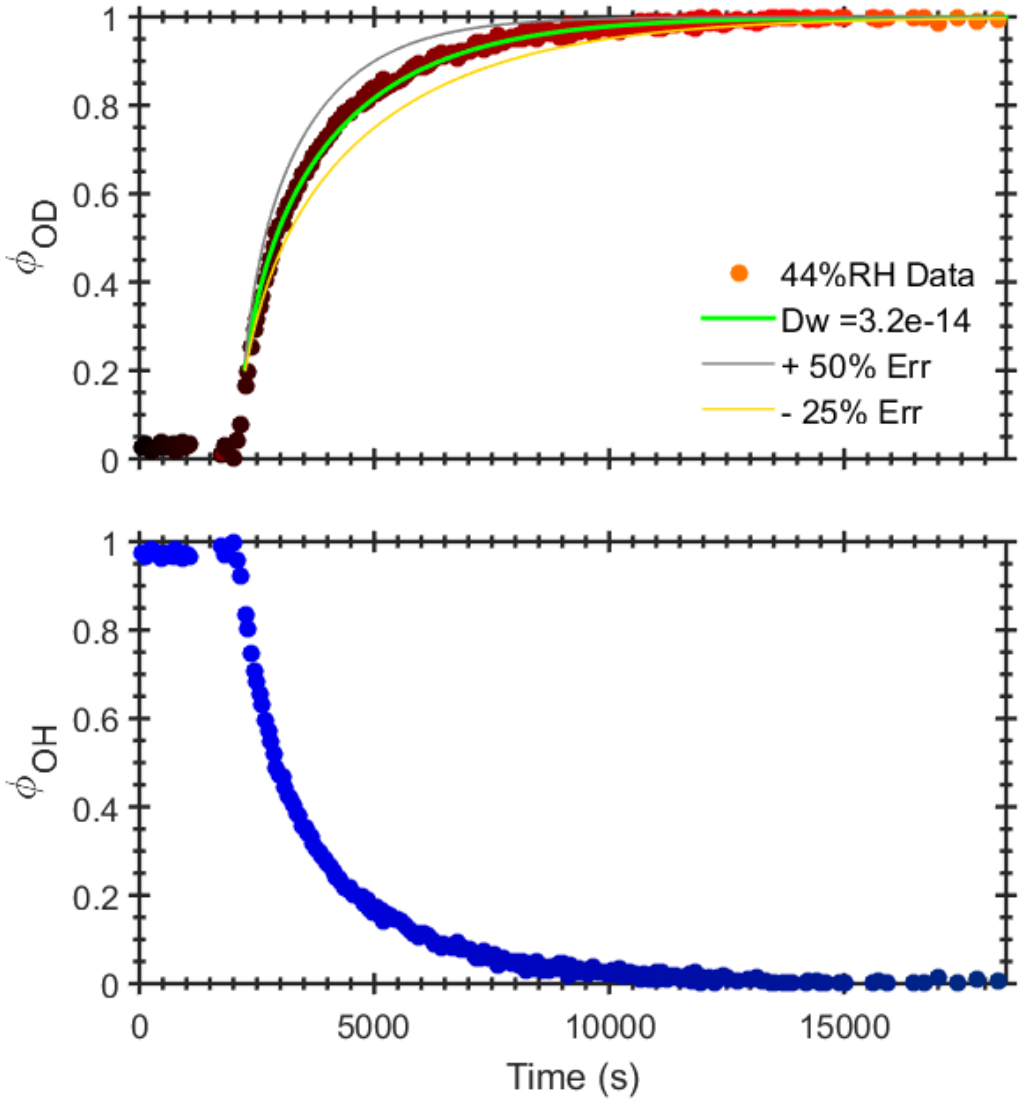

Figure 2.19. Fractional concentration of D_2O (upper) and H_2O (lower) in a sucrose droplet undergoing H/D isotope exchange at 44% RH with the model fit for D_w (green), +50 % uncertainty in D_w (gray), and -25% uncertainty in D_w (yellow).

with a three-parameter S-shaped curve where A, B, and C are empirically determined:

$$\phi_{OD} = \frac{1}{1+\mathrm{Aexp}(-B+Ct)} \tag{2.25}$$

The time at the inflection point of the S-shaped fit is selected as t = 0 for D_2O diffusion and indicates the time at which D_2O vapor has sufficiently replaced the H_2O in the trapping volume, and only the successive O-D fractional concentration data are used in the calculations. The solution to Fick's second law of diffusion applied to a sphere is used to model the time-dependent concentration, ϕ, of the diffusing D_2O:[13]

$$\phi_{D_2O} = 1 - \left(\frac{6}{\pi^2}\right)\sum_{n=1}^{\infty}\frac{1}{n^2}\exp\left(-\frac{n^2\pi^2 D_w t}{a^2}\right) \tag{2.26}$$

where D_w is the coefficient for translational diffusion of water and a is the droplet radius (m). Figure 2.20 shows a model of the fractional concentration of D_2O for different sized spheres (10 μm – 35 μm) for a fixed D_w = $1.13\text{x}10^{-15}$ m^2/s, which correlates to approximately 30% RH according to Davies *et al.* Figure 2.21 models the dependence of the fractional concentration of D_2O on D_w for a sphere of radius 25 μm. Experiments carried out for measuring concentration-dependent water diffusion coefficients in binary and ternary mixtures are found in Chapter 3 and Chapter 4.

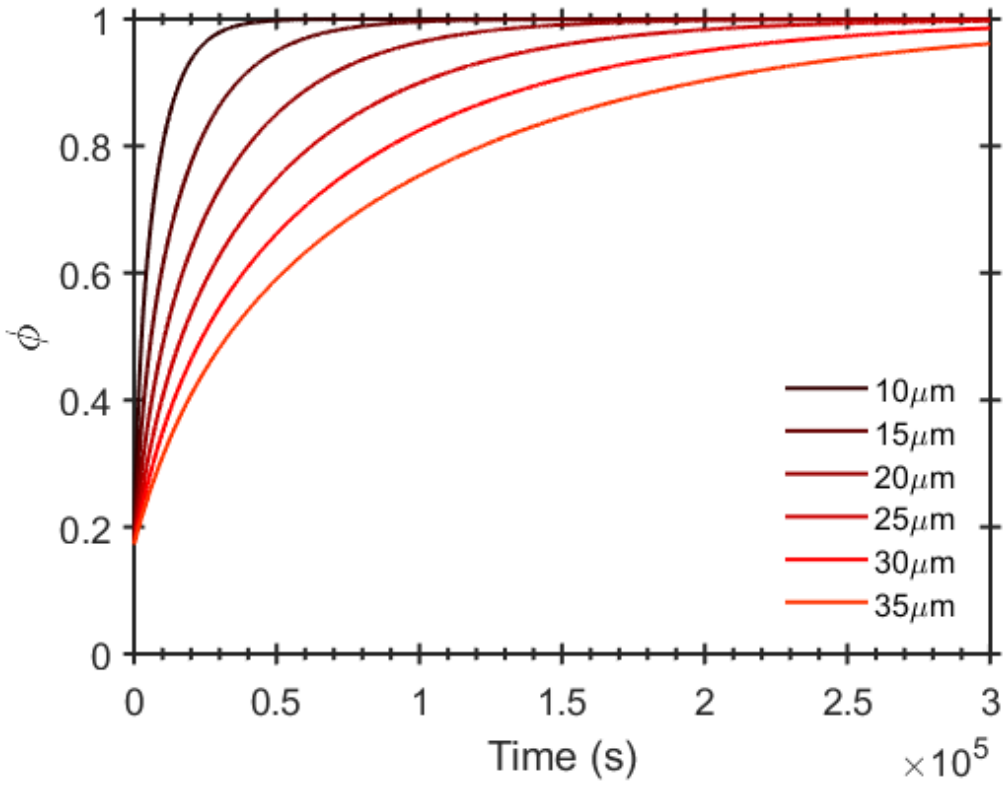

Figure 2.20. Expected fractional concentration of D_2O over time for droplets of different radii for $D_w = 1.13\text{x}10^{-25}$ m^2/s.

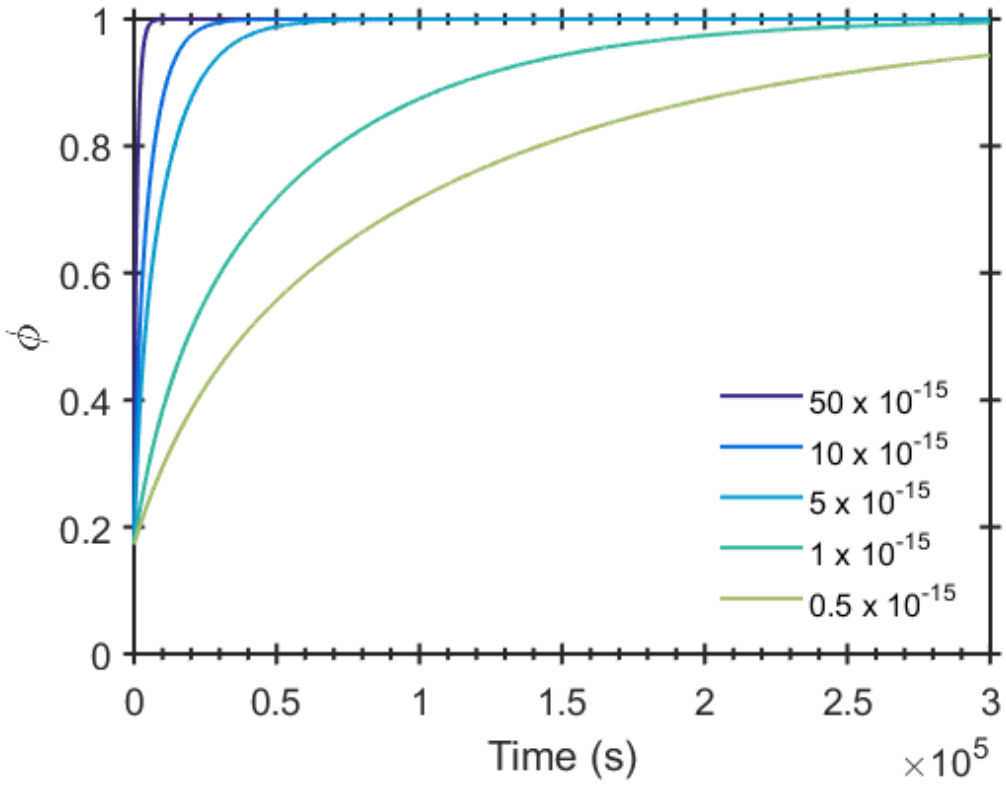

Figure 2.21. Expected fractional concentration of D_2O for a sphere with radius of 25 μm with varying water diffusion coefficients.

2.5 Instrument modifications and future directions

The development of a mobile electrodynamic balance apparatus was conceived for performing low temperature ice nucleation measurements on model and real sea spray aerosol. As shown in Figure 2.12 the cooling capabilities using the cryogenic cooler demonstrate the low, ~ -40 °C, temperatures that can be achieved in the trap are sufficient for observing homogeneous ice nucleation events of supercooled water and low-

concentration salt solutions. However, experimental challenges were encountered when temperatures below ~5 °C were reached in the trap because of a build-up of condensed water and ice in the chamber, leading to frosting of the optical windows, seen in Figure 2.22. Additionally, the droplet generator resides above the chamber and introducing a fresh droplet into the cold trap resulted in an apparent snow-effect from the intrusion of humidified laboratory air. Other low-temperature experimental setups incorporate the particle generation scheme inside the experimental chamber, some with a heating mechanism to prevent the aqueous solution inside from freezing.[17,19] In order to combat the snowing phenomenon, a custom electronic shutter system was designed and implemented which seals the chamber from laboratory air. However the focus of the experimental studies was shifted toward room temperature measurements and the effectiveness of shutter to eliminate the 'snow' has not been tested. Future work targeting low temperatures, specifically below 0 °C, will require consideration of the RH prior to lowering the temperature, and also consideration of a modified location for the droplet dispenser.

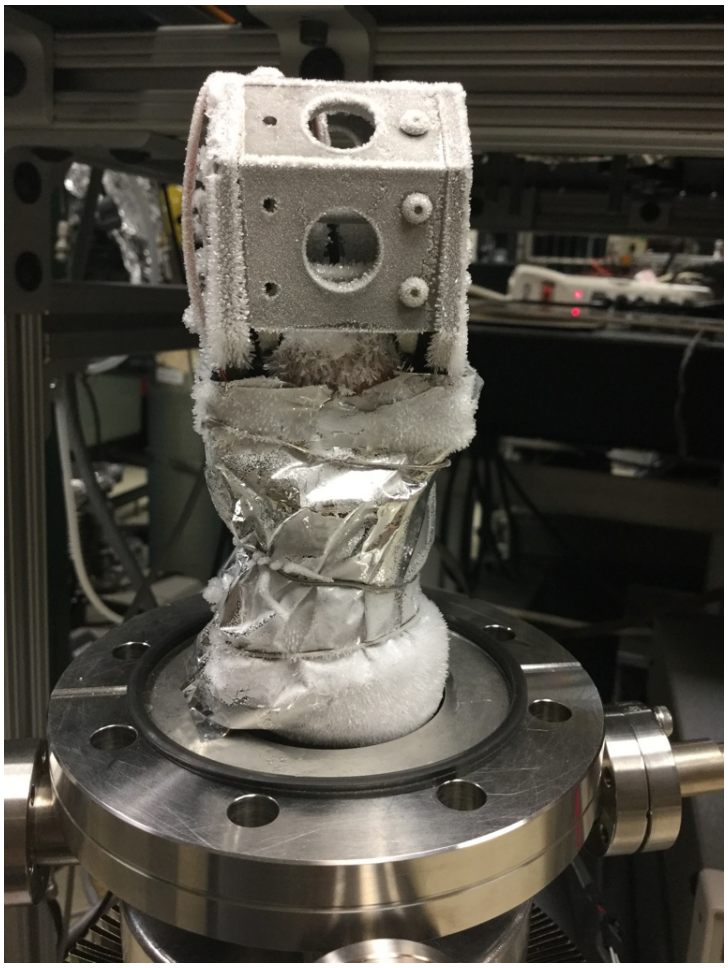

Figure 2.22. Image of the trap after lowering the temperature below – 40 °C.

2.4 References

(1) Ault, A. P.; Axson, J. L. Atmospheric Aerosol Chemistry: Spectroscopic and Microscopic Advances. *Anal. Chem.* **2017**, *89* (1), 430–452.

(2) Reid, J. P.; Bertram, A. K.; Topping, D. O.; Laskin, A.; Martin, S. T.; Petters, M. D.; Pope, F. D.; Rovelli, G. The Viscosity of Atmospherically Relevant Organic Particles. *Nat. Commun.* **2018**, *9* (1), 956.

(3) Krieger, U. K.; Marcolli, C.; Reid, J. P. Exploring the Complexity of Aerosol

Particle Properties and Processes Using Single Particle Techniques. *Chem. Soc. Rev.* **2012**, *41* (19), 6631.

(4) Reid, J. P.; Meresman, H.; Mitchem, L.; Symes†, R. Spectroscopic Studies of the Size and Composition of Single Aerosol Droplets. *Int. Rev. Phys. Chem.* **2007**, *26* (1), 139–192.

(5) Pratt, K. A.; Mayer, J. E.; Holecek, J. C.; Moffet, R. C.; Sanchez, R. O.; Rebotier, T. P.; Furutani, H.; Gonin, M.; Fuhrer, X. K.; Su, X. Y.; et al. Development and Characterization of an Aircraft Aerosol Time-of-Flight Mass Spectrometer. **2009**, *81* (5), 1792–1800.

(6) Pratt, K. A.; DeMott, P. J.; French, J. R.; Wang, Z.; Westphal, D. L.; Heymsfield, A. J.; Twohy, C. H.; Prenni, A. J.; Prather, K. A. In Situ Detection of Biological Particles in Cloud Ice-Crystals. *Nat. Geosci.* **2009**, *2* (6), 397–400.

(7) Laskina, O.; Morris, H. S.; Grandquist, J. R.; Estillore, A. D.; Stone, E. A.; Grassian, V. H.; Tivanski, A. V. Substrate-Deposited Sea Spray Aerosol Particles: Influence of Analytical Method, Substrate, and Storage Conditions on Particle Size, Phase, and Morphology. *Environ. Sci. Technol.* **2015**, *49* (22), 13447–13453.

(8) Estillore, A. D.; Morris, H. S.; Or, V. W.; Lee, H. D.; Alves, M. R.; Marciano, M. A.; Laskina, O.; Qin, Z.; Tivanski, A. V.; Grassian, V. H. Linking Hygroscopicity and the Surface Microstructure of Model Inorganic Salts, Simple and Complex Carbohydrates, and Authentic Sea Spray Aerosol Particles. *Phys. Chem. Chem. Phys.* **2017**, *19* (31), 21101–21111.

(9) Craig, R. L.; Bondy, A. L.; Ault, A. P. Computer-Controlled Raman Microspectroscopy (CC-Raman): A Method for the Rapid Characterization of Individual Atmospheric Aerosol Particles. *Aerosol Sci. Technol.* **2017**, *51* (9), 1099–1112.

(10) Craig, R. L.; Peterson, P. K.; Nandy, L.; Lei, Z.; Hossain, M. A.; Camarena, S.; Dodson, R. A.; Cook, R. D.; Dutcher, C. S.; Ault, A. P. Direct Determination of Aerosol PH: Size-Resolved Measurements of Submicrometer and Supermicrometer Aqueous Particles. *Anal. Chem.* **2018**, *90* (19), 11232–11239.

(11) Ault, A. P.; Axson, J. L. Atmospheric Aerosol Chemistry: Spectroscopic and Microscopic Advances. *Anal. Chem.* **2017**, *89* (1), 430–452.

(12) Cai, C.; Stewart, D. J.; Reid, J. P.; Zhang, Y. H.; Ohm, P.; Dutcher, C. S.; Clegg, S. L. Organic Component Vapor Pressures and Hygroscopicities of Aqueous Aerosol Measured by Optical Tweezers. *J. Phys. Chem. A* **2015**, *119* (4), 704–718.

(13) Davies, J. F.; Wilson, K. R. Raman Spectroscopy of Isotopic Water Diffusion in Ultraviscous, Glassy, and Gel States in Aerosol by Use of Optical Tweezers. *Anal. Chem.* **2016**, *88* (4), 2361–2366.

(14) Hopkins, R. J.; Mitchem, L.; Ward, A. D.; Reid, J. P. Control and Characterisation of a Single Aerosol Droplet in a Single-Beam Gradient-Force Optical Trap. *Phys. Chem. Chem. Phys.* **2004**, *6* (21), 4924–4927.

(15) Preston, T. C.; Reid, J. P. Accurate and Efficient Determination of the Radius, Refractive Index, and Dispersion of Weakly Absorbing Spherical Particle Using Whispering Gallery Modes. *J. Opt. Soc. Am. B-Optical Phys.* **2013**, *30* (8), 2113–2122.

(16) Preston, T. C.; Reid, J. P. Determining the Size and Refractive Index of Microspheres Using the Mode Assignments from Mie Resonances. *J. Opt. Soc. Am. a-Optics Image Sci. Vis.* **2015**, *32* (11), 2210–2217.

(17) Tong, H. J.; Ouyang, B.; Nikolovski, N.; Lienhard, D. M.; Pope, F. D.; Kalberer, M. A New Electrodynamic Balance (EDB) Design for Low-Temperature Studies: Application to Immersion Freezing of Pollen Extract Bioaerosols. *Atmos. Meas. Tech.* **2015**, *8* (3), 1183–1195.

(18) Davis, E. J. Electrodynamic Balance Stability Characteristics and Applications to the Study of Aerocolloidal Particles. *Langmuir* **1985**, *1* (3), 379–387.

(19) Kramer, B.; Hubner, O.; Vortisch, H.; Woste, L.; Leisner, T.; Schwell, M.; Ruhl, E.; Baumgartel, H. Homogeneous Nucleation Rates of Supercooled Water Measured in Single Levitated Microdroplets. *J. Chem. Phys.* **1999**, *111* (14), 6521–6527.

(20) Winter, H.; Ortjohann, H. W. Simple Demonstration of Storing Macroscopic Particles in a '"Paul Trap."' *Am. J. Phys.* **1991**, *59* (9), 807–813.

(21) Wineland, D. J.; Bergquist, J. C.; Itano, W. M.; Bollinger, J. J.; Manney, C. H. Atomic-Ion Coulomb Clusters in an Ion Trap. *Phys. Rev. Lett.* **1987**, *59* (26), 2935–2938.

(22) Blaum, K. High-Accuracy Mass Spectrometry with Stored Ions. *Phys. Rep.* **2006**, *425* (1), 1–78.

(23) Trevitt, A. J.; Wearne, P. J.; Bieske, E. J. Calibration of a Quadrupole Ion Trap for Particle Mass Spectrometry. *Int. J. Mass Spectrom.* **2007**, *262* (3), 241–246.

(24) Jelić, A.; Petrović, M.; Barceló, D. Multi-Residue Method for Trace Level

Determination of Pharmaceuticals in Solid Samples Using Pressurized Liquid Extraction Followed by Liquid Chromatography/Quadrupole-Linear Ion Trap Mass Spectrometry. *Talanta* **2009**, *80* (1), 363–371.

(25) Hager, J. W.; Le Blanc, J. C. Y. High-Performance Liquid Chromatography–Tandem Mass Spectrometry with a New Quadrupole/Linear Ion Trap Instrument. *J. Chromatogr. A* **2003**, *1020* (1), 3–9.

(26) Josephs, J. L.; Sanders, M. Creation and Comparison of MS/MS Spectral Libraries Using Quadrupole Ion Trap and Triple-Quadrupole Mass Spectrometers. *Rapid Commun. Mass Spectrom.* **2004**, *18* (7), 743–759.

(27) Davies, J. F.; Miles, R. E. H.; Haddrell, A. E.; Reid, J. P. Temperature Dependence of the Vapor Pressure and Evaporation Coefficient of Supercooled Water. *J. Geophys. Res.* **2014**, *119* (18), 10931–10940.

(28) Chan, M. N.; Lee, A. K. Y.; Chan, C. K. Responses of Ammonium Sulfate Particles Coated with Glutaric Acid to Cyclic Changes in Relative Humidity: Hygroscopicity and Raman Characterization. *Environ. Sci. Technol.* **2006**, *40* (22), 6983–6989.

(29) Wuerker, R. F.; Shelton, H.; Langmuir, R. V. Electrodynamic Containment of Charged Particles. *J. Appl. Phys.* **1959**, *30* (3), 342–349.

(30) Gerlich, D. Inhomogeneous RF Fields: A Versatile Tool for the Study of Processes with Slow Ions; Wiley-Blackwell, 2007; pp 1–176.

(31) March, R. E. Quadrupole Ion Traps. *Mass Spectrom. Rev.* **2009**, *28* (6), 961–989.

(32) March, R. E. An Introduction to Quadrupole Ion Trap Mass Spectrometry. *J. Mass Spectrom.* **1997**, *32* (4), 351–369.

(33) Paul, W. Electromagnetic Traps for Charged and Neutral Particles. *Rev. Mod. Phys.* **1990**, *62* (3), 531–540.

(34) Paul, W.; Steinwedel, H. A New Mass Spectrometer without a Magnetic Field. *Zeitschrift für Naturforsch.* **1953**, *8a*, 448–450.

(35) O'Hair, R. A. J. The 3D Quadrupole Ion Trap Mass Spectrometer as a Complete Chemical Laboratory for Fundamental Gas-Phase Studies of Metal Mediated Chemistry. *Chem. Commun.* **2006**, *0* (14), 1469.

(36) Davis, E. J. A History of Single Aerosol Particle Levitation. *Aerosol Sci. Technol.* **1997**, *26* (3), 212–254.

(37) Schlemmer, S.; Illemann, J.; Wellert, S.; Gerlich, D. Nondestructive High-Resolution and Absolute Mass Determination of Single Charged Particles in a Three-Dimensional Quadrupole Trap. *J. Appl. Phys.* **2001**, *90* (10), 5410–5418.

(38) Trevitt, A. J.; Wearne, P. J.; Bieske, E. J. Calibration of a Quadrupole Ion Trap for Particle Mass Spectrometry. *Int. J. Mass Spectrom.* **2007**, *262* (3), 241–246.

(39) Hermann, G.; Zhang, Y.; Wassermann, B.; Fischer, H.; Quennet, M.; Ruhl, E. Charge Effects on the Efflorescence in Single Levitated Droplets. *J. Phys. Chem. A* **2017**, *121* (36), 6790–6799.

(40) Ray, A. K.; Souyri, A.; Davis, E. J.; Allen, T. M. Precision of Light-Scattering Techniques for Measuring Optical-Parameters of Microspheres. *Appl. Opt.* **1991**, *30* (27), 3974–3983.

(41) Glantschnig, W. J.; Chen, S. H. Light-Scattering From Water Droplets in the Geometrical-Optics Approximation. *Appl. Opt.* **1981**, *20* (14), 2499–2509.

(42) van de Hulst, H. C. *Light Scattering by Small Particles.*; John Wiley and Sons: New York, New York, 1957.

(43) Marsh, A.; Miles, R. E. H.; Rovelli, G.; Cowling, A. G.; Nandy, L.; Dutcher, C. S.; Reid, J. P. Influence of Organic Compound Functionality on Aerosol Hygroscopicity: Dicarboxylic Acids, Alkyl-Substituents, Sugars and Amino Acids. *Atmos. Chem. Phys.* **2017**, *17* (9), 5583–5599.

(44) Norrish, R. S. An Equation for the Activity Coefficients and Equilibrium Relative Humidities of Water in Confectionery Syrups. *J. Food Sci. Technol.* **1966**, *1*, 25–39.

(45) Chirife, J.; Ferro Fontan, C.; Benmergui, E. A. The Prediction of Water Activity in Aqueous Solutions in Connection with Intermediate Moisture Foods IV. Aw Prediction in Aqueous Non Electrolyte Solutions. *J. Food Technol.* **1980**, *15*, 59–70.

(46) Cai, C.; Miles, R. E. H.; Cotterell, M. I.; Marsh, A.; Rovelli, G.; Rickards, A. M. J.; Zhang, Y. H.; Reid, J. P. Comparison of Methods for Predicting the Compositional Dependence of the Density and Refractive Index of Organic-Aqueous Aerosols. *J. Phys. Chem. A* **2016**, *120* (33), 6604–6617.

(47) Clegg, S. L.; Brimblecombe, P.; Wexler, A. S. Thermodynamic Model of the System H+-NH4+-Na+-SO42--NB3--Cl--H2O at 298.15 K. *J. Phys. Chem. A* **1998**, *102* (12), 2155–2171.

(48) Clegg, S. L.; Seinfeld, J. H.; Brimblecombe, P. Thermodynamic Modelling of Aqueous Aerosols Containing Electrolytes and Dissolved Organic Compounds. *J. Aerosol Sci.* **2001**, *32* (6), 713–738.

(49) Zuend, A.; Marcolli, C.; Luo, B. P.; Peter, T. A Thermodynamic Model of Mixed Organic-Inorganic Aerosols to Predict Activity Coefficients. *Atmos. Chem. Phys.* **2008**, *8* (16), 4559–4593.

(50) Zuend, A.; Marcolli, C.; Booth, A. M.; Lienhard, D. M.; Soonsin, V.; Krieger, U. K.; Topping, D. O.; McFiggans, G.; Peter, T.; Seinfeld, J. H. New and Extended Parameterization of the Thermodynamic Model AIOMFAC: Calculation of Activity Coefficients for Organic-Inorganic Mixtures Containing Carboxyl, Hydroxyl, Carbonyl, Ether, Ester, Alkenyl, Alkyl, and Aromatic Functional Groups. *Atmos. Chem. Phys.* **2011**, *11* (17), 9155–9206.

(51) Davis, E. J.; Aardahl, C. L.; Widmann, J. F. Raman Studies of Aerosol Chemical Reactions. *J. Dispers. Sci. Technol.* **1998**, *19* (2–3), 293–309.

(52) Reid, J. P.; Mitchem, L. Laser Probing of Single-Aerosoldroplet Dynamics. *Annu. Rev. Phys. Chem.* **2006**, *57*, 245–271.

(53) Salomon, M. *Thermodynamic Properties of Liquid H2O and D2O and Their Mixtures*; United States. National Aeronautics and Space Administration. "NASA Technical Note." Print.: Washington, D.C., 1969.

(54) Price, H. C.; Murray, B. J.; Mattsson, J.; O'Sullivan, D.; Wilson, T. W.; Baustian, K. J.; Benning, L. G. Quantifying Water Diffusion in High-Viscosity and Glassy Aqueous Solutions Using a Raman Isotope Tracer Method. *Atmos. Chem. Phys.* **2014**, *14* (8), 3817–3830.

CHAPTER 3: Water Diffusion Measurements of Single Charged Aerosol Using H_2O/D_2O Isotope Exchange and Raman Spectroscopy in an Electrodynamic Balance

3.1 Introduction

Atmospheric aerosols are capable of scattering and absorbing solar radiation directly as well as interacting indirectly through cloud formation, and thus have great impact on climate and the hydrological cycle. Recently, the discovery of highly viscous and amorphous biogenic aerosol[1,2] has attracted attention due to the prospect for very slow kinetics governing chemical change in these systems.[3–5] While aqueous droplets with low viscosities establish equilibrium with the surrounding environment rapidly, the reduced translational mobility of molecules in high viscosity droplets reduces the rate of equilibration. This inevitably leads to reductions in heterogeneous reaction rates,[6,7] impedes hygroscopic growth,[8,9] and enhances ice nucleation.[10,11] In order to quantify and model these phenomena, an understanding of water diffusion within such aerosol particles is essential as water is often the most mobile component in a viscous aqueous solution.

The Stokes-Einstein relation describes the diffusivity of solutes as a function of viscosity. A number of experimental techniques have been developed[4,12–14] to measure

the viscosity of individual aerosol particles both in the field and in the laboratory. In particular, recent studies have examined the impact of chemical composition and oxidation state of a variety of organic compounds on viscosity spanning a dynamic range from 10^{-3} Pa·s to values above the glass transition of 10^{12} Pa·s.[15] Experimental techniques for measuring viscosity are important for improving our understanding of how chemical and environmental factors impact the phase state and heterogeneous reaction rates of ambient aerosol. Saccharides, in particular sucrose, have been used as model systems for validating new techniques to measure single aerosol viscosity[9,14] because they can undergo a change in viscosity of greater than 10 orders of magnitude between 0 – 100 % RH, allowing for the comparison of methods over a wide dynamic range. Recent chemical analyses on nascent sea spray aerosol have revealed that saccharides are enriched in aerosol relative to sea water concentrations,[16] and thus sucrose is an appropriate atmospherically relevant model chemical system.

However, application of the Stokes-Einstein relationship to aerosols using viscosity measurements alone has been shown to provide only a lower bound to the estimation of the diffusion coefficient because of the ability of water molecules to percolate through channels in viscous matrices.[15,17,18] Therefore, techniques which measure water diffusion independent from viscosity are necessary to accurately predict evaporation, condensation, and cloud activation processes.

The development of methods to measure slow water diffusion directly has been a challenge, and only in recent years several complementary methods have been reported.

Zhu *et al.* quantified maltose diffusion using Raman microscopy and isotopic labeling by compressing a non-deuterated and deuterated drop of maltose between two glass slides, creating an interface between the droplets.[19] The Raman C-D and C-H stretches were used to monitor the diffusion of the molecules across the interface as a function of temperature and humidity. Price *et al.* extended the method of Zhu to measure the diffusion coefficient for water in a sucrose-water disk by isotopically labeling the gas phase molecules and monitoring the substitution of D_2O for H_2O in the solution with Raman microscopy.[20]

However, compared to studying water diffusion of atmospheric aerosols on a substrate, contactless single particle techniques are preferred, because the aerosol is free from impacts of surface perturbations at concentrations above the solubility limit. In addition, single particle measurements are preferred over ensemble-averaged experiments, because composition and local chemical environments vary particles from particle to particle. Optical tweezers are one technique for spectroscopic studies of single, spherical particles from 1-10 μm in diameter that are trapped at the center of a tightly focused laser beam by a balance of photon gradient forces which are insensitive to charge state.[21] Scattering from the focusing laser is collected to provide high resolution size measurements using cavity enhanced features of the light scattering such as morphology dependent resonances,[22,23] as well as chemical identity from the Raman scattering or fluorescence. The response of a single particle to changes in humidity or ambient gaseous composition provides measurements of chemical kinetics,[24,25] and hygroscopicity.[26] For

example, Davies *et al.* combined the isotopic exchange technique with an aerosol optical tweezer for single-particle confinement[27] which reduced the sample size to less than 6 μm radius, speeding up the experimental timescales from weeks to hours. Isotopic tracer experiments have been carried out at a constant relative humidity (RH) leading to a constant size and solute concentration. Using Fick's second law of diffusion, Davies *et al.* modeled the time-dependent intensities of the ν(O-D) and ν(O-H) Raman peaks to quantify the diffusion coefficient as a function of concentration or water activity.[27]

The electrodynamic balance (EDB) is a single particle technique that offers similar advantages including contactless levitation. However, it is not limited by size or morphology, as the trapping potential depends solely on mass-to-charge ratio. EDBs have been used extensively to measure physicochemical properties of single aerosol particles such as evaporation rates[28–31] and nucleation,[32–36] and provide complementary results to optical tweezers. For example, Zobrist *et al* used an EDB to conduct water diffusion measurements by creating a step change in the RH and observing the change in particle size using Mie resonance spectroscopy.[37] The result was interpreted using a theoretical framework based on principles of mass transport by dividing the particle into a discrete number of shells, within which water molecules translationally move to establish equilibrium. The flux of water molecules between shells, along with dynamic adjustment to the time-steps and shell thickness, was calculated to extract a concentration-dependent diffusion coefficient. Under high viscosity conditions the particle was assumed as a core-shell phase state as the surface established equilibrium rapidly while the core remained

viscous, creating a non-linear radial concentration gradient. This led to the refractive index becoming a fit parameter along with the radius, decreasing the accuracy of the model at low RH. Despite differences in experimental setups, the isotope tracing model and mass transport model produce similar water diffusion coefficients in sucrose over a wide range of RH.[20,27,37]

The present work reports a new technique that combines the Raman spectroscopic isotope tracing method previously applied on single aerosol in optical tweezers by Davies *et al.*[27] with an RH-controlled EDB to trap single charged aerosol droplets for measuring water diffusion. A sucrose-H_2O microdroplet is trapped and equilibrated at a specific RH, and then exposed to D_2O at the same RH. Raman spectra of the droplet are acquired as a function of time, in order to assess the progression of D_2O diffusing into the droplet. D_2O was observed to eventually replace all H_2O, as indicated by complete disappearance of the ν(O-H) asymmetric stretch peak in the Raman spectrum. It is assumed that the entire droplet is irradiated with the laser and the total content of water remains constant throughout an experiment so that a volume-averaged Fickian diffusion model can be used to describe the exponential growth of the ν(O-D) Raman peak. In the following section, the experimental approach is described followed by measurements of the water diffusion coefficient in single charged sucrose-water droplets are reported over a range of RH conditions and compared with previous results using some of the alternative techniques described above.

3.2. Experimental

Water diffusion in single, charged sucrose-water microdroplets was studied using a D2O/H2O isotope exchange method in a new electrodynamic balance (EDB). Schematics of the experimental setup and optical layout are shown in Figure 3.1. The electrodynamic trap electrode geometry is based on the design of Schlemmer et al.[38] later characterized in detail by Trevitt et al.[39] The trap is composed of two conical endcap electrodes separated by 5.3 mm with a 2.5 mm axial channel for laser optical access. Eight concentric rod electrodes replace the ring electrode in a traditional Paul trap, allowing for optical access over a wide range of angles. Each rod is electrically isolated, however an external DC levitation voltage is applied to the two rods directly below the trap center to counterbalance the gravitational force of the trapped microdroplet. The AC voltage is applied to the endcap electrodes only, at typical values V_p = 1500 V and f = 150 Hz. During an experiment the levitation voltage is adjusted using an automated LabView feedback control loop for maintaining the droplet in the trap center, while the AC frequency is maintained approximately constant.

The trap is mounted on a DN63CF Conflat flange equipped with electrical feedthroughs as well as a 1/8" OD copper gas-line feedthrough for introducing humidified or dried air directly into the trap. The trap is built on two octagonal plates, and is isolated from the air in the chamber by a set of stainless steel plates outfitted with windows, serving to electrically shield the high voltage electrodes which may otherwise interfere with the trajectory of incoming charged droplets. The plates also isolate the

volume of air in the trap from the surrounding chamber, reducing the time for equilibration of the RH. The primary mounting structure is augmented by a secondary Teflon housing that provides a direct channel from the opening of the chamber. The droplet generator is located above the trap, without interacting with the larger volume of air in the chamber. An electronic shutter is located at the opening of the chamber that opens for the introduction of a new droplet. A piezoelectric droplet generator (Engineering Arts DE03) is connected to an electronic syringe pump for precise control of the production of the aqueous droplets. Filtered aqueous sucrose solution is aspirated into the capillary of the droplet generator from which single droplets approximately 40 μm diameter are generated on demand using computer-controlled pulse generation to drive the piezoelectric element. A charging ring located above the shutter inductively charges the droplets using a DC field. Occasionally multiple droplets are trapped simultaneously and the frequency of the AC is adjusted until all but one droplet are ejected.

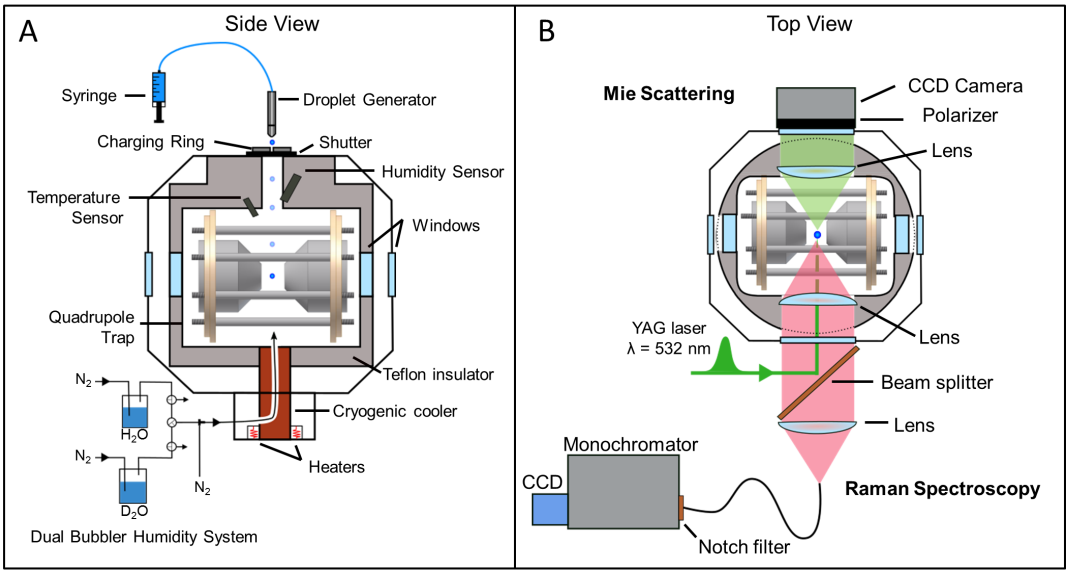

Figure 3.1. A) Experimental setup of the electrodynamic balance (EDB) apparatus contained in a secondary Teflon housing inside an environmental chamber and equipped with a droplet generator and dual bubbler RH control. B) Optical layout for a trapped droplet irradiated with a pulsed 532 nm laser. The forward Mie elastic scattering is collected on a CCD camera and the back-scattered Raman signal is passed through a beamsplitter and focused into a grating spectrometer.

The relative humidity in the trap is controlled with digital mass flow controllers (Alicat MC-500SCCM) by mixing N_2 with the humidified vapor headspace of a bubbler containing water. The humidified air is subsequently directed through copper tubing wrapped around and welded to a copper standoff in thermal contact with a Stirling free-piston coldhead cooler (Sunpower Cryotel CT) and resistive heaters, which serve to maintain a constant temperature and thermalize the air before entering the trap. However, the temperature control was not used in these experiments and the trap was maintained at the laboratory temperature, approximately 20-23° C. The temperature is recorded using a

temperature probe (Vaisala HMP60) with ±1° C accuracy. Two bubblers, one containing distilled H_2O and the other containing high purity D_2O (>99.8% D atom, Acros Organics), are arranged using 3-way valves as shown in Figure 3.1A so that air from one bubbler is selected to flow into the chamber while the other bubbler is exhausted. Experiments are carried out at constant RH by first trapping a single sucrose droplet in H_2O RH and allowing sufficient time for equilibration. Then D_2O vapor at the same RH is introduced to the chamber, replacing the gas-phase H_2O in the trap and eventually diffusing into the H_2O droplet. During each experimental run, the H_2O humidified air is initially directed into the chamber for droplet equilibration while the D_2O bubbler is exhausted to fill intermediate tubing lines, minimizing changes in RH during the gas transition in the trap. The relative humidity and temperature are monitored using a humidity probe (Vaisala HMP60) with ±3% RH accuracy located approximately 25 mm downstream of the RH flow. For each water diffusion measurement the relative humidity is maintained constant to ±1%, or within the error of the probe. When the chamber atmosphere is switched to D_2O, the humidity probe measurement must be corrected for the difference in equilibrium vapor pressure of D_2O versus H_2O[40] as shown in Eqn (1) where A = -0.30661, B = 9.14056, and C = 75.753 and T is in Celsius.

$$ln\left(\frac{p^0_{H_2O}}{p^0_{D_2O}}\right) = A + \frac{B}{C+T} \tag{3.1}$$

Two spectroscopic methods are used to characterize a trapped particle: Mie scattering for determining the particle size and Raman spectroscopy for chemical

analysis. Shown in Figure 3.1B the trapped droplet is irradiated with a focused 80 kHz, 532 nm Nd:YAG laser beam (RPMC Wedge XF). The elastic Mie scattering is collimated using an *f/2* lens with a solid angle of 24.5° centered at 45° in the forward-scattering direction and imaged onto a monochromatic CCD camera. The morphology of the trapped droplet is determined by the Mie scattering pattern. Spherical droplets exhibit evenly spaced bands and crystalline or amorphous solid particles exhibit an irregular pattern.[32] Figure 3.2 shows an example Mie image of a single droplet and the resulting angular intensity spectrum, previously demonstrated in the literature to follow closely with Mie theory.[23] The diameter of droplets in these experiments is significantly larger than the wavelength of light, allowing a geometric optics approximation to be applied. The intensity spectrum is processed using a fast Fourier Transform (FFT) to compute an average band spacing, $\Delta\theta$, (rad^{-1}). The band spacing is used in conjunction with the index of refraction, *n*, to calculate the particle radius*, r*, using Eqn (2):[41]

$$r = \frac{\lambda}{\Delta\theta}\left(\cos\left(\frac{\theta}{2}\right) + \frac{n\sin\left(\frac{\theta}{2}\right)}{\sqrt{1+n^2-2n\cos\left(\frac{\theta}{2}\right)}}\right)^{-1} \tag{3.2}$$

where λ is the laser wavelength (μm) and θ is the median scattering angle (rad). The parameterization of the index of refraction with concentration of sucrose is described further in the Results section.

The evolving chemical composition of the trapped droplet from H_2O to D_2O is analyzed using the intensity of the stretches ν(O-D) ~ 2500 cm^{-1} and ν(O-H) ~ 3400 cm^{-1}

in the Raman spectrum. The integrated intensity of these features allows calculation of the fractional concentration of D_2O in the sucrose droplet over time. The back-scattered Raman signal is collected using *f/2* optics, transmitted through the 532 nm laser edge beam splitter, and focused into a fiber optic cable coupled into a monochromator (Acton SpectraPro 275) with an open-electrode TE-cooled CCD detector (Horiba Syncerity). The spectrometer is equipped with a 600 g/mm grating with a 750 nm blaze for optimized quantum efficiency between 620-660 nm. The integration time for each spectrum is 30-120 s to achieve adequate signal-to-noise ratio. The LabView control and data acquisition program records the Mie and Raman spectra at a designated interval along with trap settings and conditions.

3.3 Results and Discussion

In this work, the time dependent fractional concentration of the ν(O-D) Raman peak is modeled using Fick's second law of diffusion to calculate the water diffusion coefficient in a sucrose microdroplet for a range of RH. The timescale for diffusion is highly dependent on the droplet radius and therefore an accurate size measurement is necessary for incorporation into the diffusion model. In order to calculate the droplet size from the angular intensity spectrum produced by the Mie scattering, the index of refraction was calculated as a function of sucrose concentration, which varies with water activity or RH. The method of parameterization of the index of refraction will be

presented, followed by a discussion of how the Raman spectra were analyzed to determine the rate of isotopic substitution as D_2O diffused into the suspended droplet. With these results, the sucrose-concentration-dependent water diffusion coefficients were calculated and modeled using a Vignes-type fit for comparison with the literature and validation of this method.

3.3.1 Parameterizations of the index of refraction

Calculation of the index of refraction for the sucrose droplet as a function of varying RH requires parameterization of the mass fraction solute (MFS) and density (ρ). The dependence of MFS on water activity, a_w, has been well studied for sucrose solutions and the treatment by Norrish[42] has been shown to correlate with experimental measurements over the entire RH range:

$$a_w = x_w \exp(k x_s^2) \tag{3.3}$$

where x_w and x_s are the mole fractions of water and solute, respectively, and k is an empirical constant equal to -6.47 for sucrose.[43] The density of a sucrose-water mixture can be taken as the volume additivity of pure component densities (VAD), with the pure component density of water, $\rho_w = 1000$ kg·m^{-3}, and sucrose,[44] $\rho_s = 1580.5$ kg·m^{-3} giving:

$$\frac{1}{\rho} = \frac{1-MFS}{\rho_w} + \frac{MFS}{\rho_s} \tag{3.4}$$

The refractive index of a sucrose solution varies with MFS and is parameterized using a linear fit with the refractive index for water, n = 1.33, at MFS(0) and n = 1.558 at

MFS(1).[45] The calculated index of refraction of the sucrose droplet at a given RH is then used in Eqn (2) to calculate the droplet diameter.

3.3.2 Diffusion of D_2O using Raman Spectroscopy

The coefficient for translational diffusion of water, D_w, as a function of water activity, or RH, is extracted using a solution to Fick's second law of diffusion as applied to a sphere.[46] Since the total amount of sucrose is constant throughout each experiment all spectra are normalized to the sucrose ν(C-H) peak at 2900 cm^{-1}, allowing for correction for fluctuations in spectral intensity due to low amplitude motions of the droplet in the laser beam. A seven-Gaussian fit is applied to the spectrum between 2000 – 3800 cm^{-1} to determine individual peak contributions and therefore calculations of relative abundances of chemical species present. Two Gaussians contribute to the O-D band, two Gaussians to the C-H stretch, one Gaussian to the weak C-H overtone peak *(α)*, two Gaussians to the O-H band, and a weak, broad Gaussian accounts for background signal. Figure 3.2B shows the contributions of the seven Gaussians for an example Raman spectra of a sucrose droplet approximately halfway through an isotope exchange experiment when distinct peaks from both H_2O and D_2O are present.

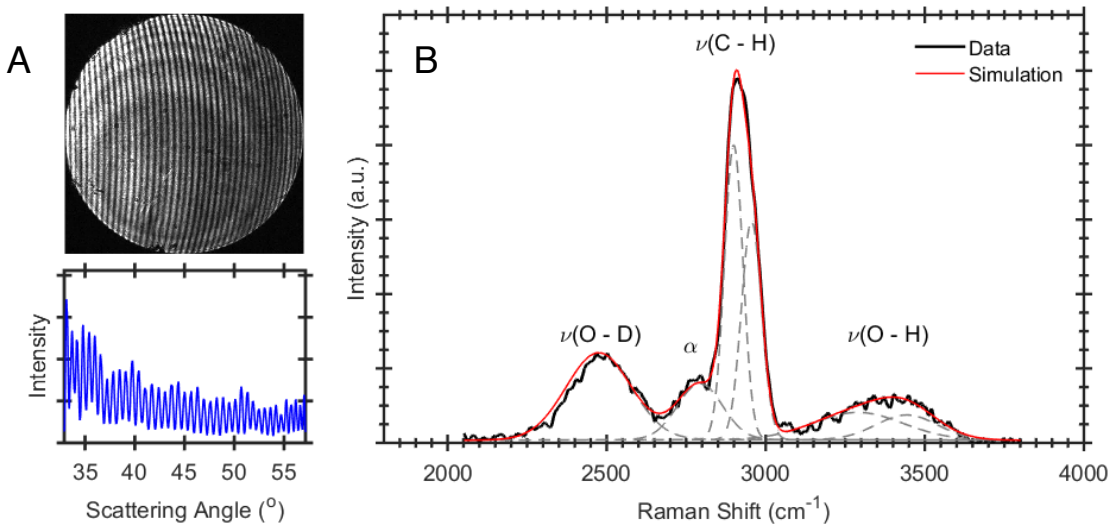

Figure 3.2. A) Mie scattering image collected on a CCD camera for a 54 μm sucrose droplet and the associated angular intensity spectrum used to calculate the droplet size. B) Representative Raman spectrum for a sucrose droplet undergoing isotope exchange contains overlapping vibrational peaks which are simulated with a series of Gaussian peaks shown as the sum (red) and individual peak contributions (grey dashed).

At a constant relative humidity, the total amount of water in the droplet is assumed to be constant and equal to the sum of the contributions from H_2O and D_2O. Figure 3.3A shows the progression of Raman spectra collected during an experiment, starting from the top where only the ν(O-H) is observed and over time the intensity of the ν(O-H) decays and the ν(O-D) grows in. The spectrum is decomposed using seven Gaussian peaks fitting as discussed earlier, from which the peak areas for O-D and O-H are used to calculate the fractional concentration of D_2O in the droplet:

$$\phi_{OD} = \frac{A_{OD}}{A_{OD} + \frac{1}{\sqrt{2}} A_{OH}} \tag{3.5}$$

where the O-D stretch located at 2500 cm^{-1} has a lower integrated intensity by a factor of $1/\sqrt{2}$ based on the difference in reduced mass.[47] When the gas manifold valves are rotated to switch from H_2O to D_2O, there is a time delay until the chamber is sufficiently filled with D_2O and the isotope exchange begins. Figure 3.3B shows the concentration fractions of D_2O and H_2O at 44% RH that are initially constant as the droplet equilibrates and then abruptly change from baseline values. It can be assumed that for a period of time, which is longer at lower humidities, the droplet is undergoing isotope exchange while the chamber atmosphere is a mixture of H_2O, HOD, and D_2O. During this time the vapor-liquid interface does not meet the condition that the gas-phase concentration of D_2O is constant, assumed by the diffusion model derived from Fick's second law. We therefore introduce a systematic approach for determining when constant D_2O RH is reached by fitting the time-dependent fractional concentration of OD with a three-parameter S-shaped curve where A, B, and C are empirically determined:

$$\phi_{OD} = \frac{1}{1+A\exp(-B+Ct)} \tag{3.6}$$

The time at the inflection point of the S-shaped fit is selected as $t = 0$ for D_2O diffusion and indicates the time at which D_2O vapor has sufficiently replaced the H_2O in the trapping volume, and only the successive O-D fractional concentration data are used in the calculations. The solution to Fick's second law of diffusion applied to a sphere is used to model the time-dependent concentration, ϕ, of the diffusing D_2O:[27]

$$\phi_{D_2O} = 1 - \left(\frac{6}{\pi^2}\right)\sum_{n=1}^{\infty}\frac{1}{n^2}\exp\left(-\frac{n^2\pi^2 D_w t}{a^2}\right) \tag{3.7}$$

where a is the particle radius and D_w is the translational diffusion constant. A three-term expansion of equation (3.7) with a single adjustable parameter is used to calculate D_w for each of the experimental runs at a different RH. The upper limit for diffusion coefficients measured using this technique is calculated as ~5 x 10^{-13} m^2s^{-1}. The sources of the upper limit include the rapid diffusion in the droplet sizes at high RH, the acquisition time required for adequate spectral signal-to-noise, and the time delay associated with fully replacing the composition of air in the trapping volume.[27]

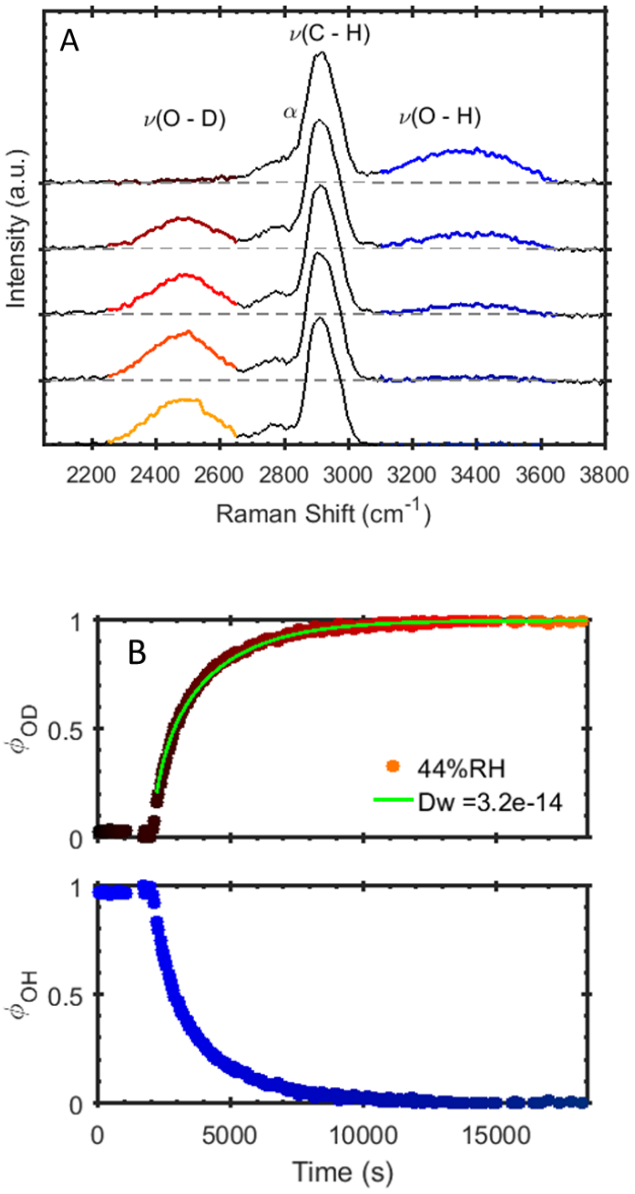

Figure 3.3. A) An example set of Raman spectra for a 54 µm sucrose droplet undergoing isotope exchange at 44% RH shows the decrease in peak intensity of the ν(O-H) at ~3400 cm^{-1} and the growth of the ν(O-D) at ~ 2900 cm^{-1}. B) The fraction of the water concentration of D_2O and H_2O in the droplet over time.

The water diffusion coefficients measured for sucrose-water droplets at RH between 26-54% at room temperature are shown in Figure 3.4. The RH is reported with absolute error of the probe, ±3 %, and the error in the D_w measurement is estimated as 50%, calculated from an uncertainty of ±20% in the model fit, ±1 μm uncertainty in the size calculation, differences in self-diffusion between H_2O and D_2O, the RH fluctuation (±1%) and temperature stabilization (± 1 ºC) over the course of an experiment. The results are compared with parameterizations from literature reported by Zobrist *et al.*,[37] Price *et al.*,[20] and Davies *et al.*[27] Our results agree well with the Vignes-type parameterization which describes the variation of the water diffusion coefficient, D_w, with composition in a binary mixture:[48]

$$D_w = \left(D^0_{w,w}\right)^{x_w}\left(D^0_{w,s}\right)^{(1-x_w)} \tag{3.8}$$

where x_w is the mole fraction of water, $D^0_{w,w}$ is the translational diffusion coefficient in pure water (2 x 10^{-9} m^2s^{-1}), and $D^0_{w,s}$ is the self-diffusion coefficient of water in pure solute. It was found in this work that the value for $D^0_{w,s}$ agreed well with the parameterized value, 1.9 x 10^{-27} m^2s^{-1}, reported by Davies *et al.*[27] There is also excellent agreement between the present results using the EDB and previous reports showing the viability of this method for quantifying the translational diffusion coefficient over a range of water activities. However, the agreement deviates when approaching at the high RH limit. At 54 % the timescale for diffusion is comparable to the turnover time for replacing the air in the chamber, allowing for isotopic exchange to occur rapidly in the droplet while exposed to an effectively lower D_2O concentration because the air is still a mixture

of H_2O and D_2O. The resulting D_w at high RH, approximately $1x10^{-13}$ m^2s^{-1}, is lower than the Vignes-type trend followed by the remaining experiments and serves as an upper bound to the dynamic range of the diffusion coefficients able to be quantified using this experimental setup.

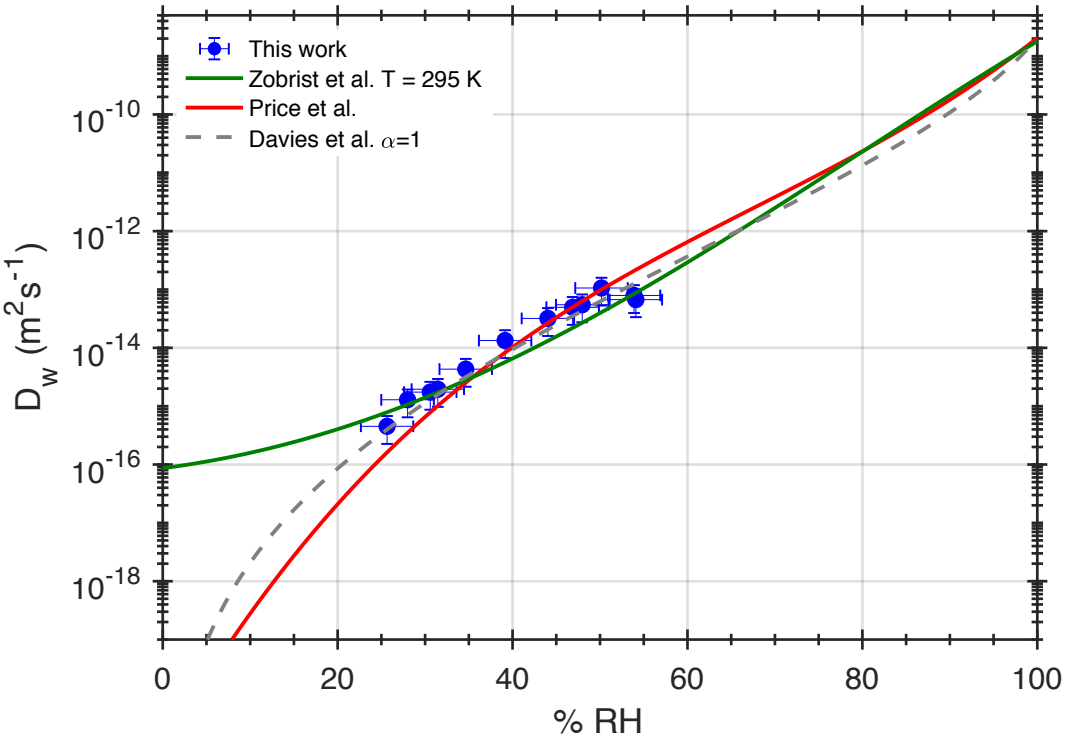

Figure 3.4. Calculated water diffusion coefficients in sucrose droplets at varying RH studied in this work compared with parameterizations provided by Zobrist *et al.*,[37] Price *et al.*[20] and Davies *et al.*[27]

The results in Figure 3.4 are consistent with measurements carried out using isotope exchange over 6 – 300 μm diameter samples which suggests there is not a significant impact of droplet size on the water diffusion coefficient in the 35 – 60 μm size range studied. The droplet diameters studied in this work were significantly larger than the <10 μm diameter droplets used by Zobrist *et al.*[37] and Davies *et al.*[27] and significantly smaller than the 200 – 300 μm diameter substrate-supported disks used by Price *et al.*[20] Figure 4 shows that the present data is in good agreement with other isotope exchange methods. It is suggested that the droplet size does not have a significant effect on the diffusion coefficient since a correlation between D_w and diameter across these different size ranges is not observed.

Figure 3.4 also shows that our results follow the trend of the isotope exchange methods from Davies *et al.* and Price *et al.* at low RH, but deviate from the mass transport model reported by Zobrist *et al.*[37] Different assumptions used in the isotope exchange and in mass transport models could explain the differences in the reported diffusion coefficients, as the predictions diverge as the glassy regime is approached at low (~25%) RH. When approaching the glass transition, the viscosity of a sucrose-water droplet increases over 10 orders of magnitude compared to the bulk.[14] Accordingly, the diffusion timescales for water lengthen to tens of hours to days at the associated high solute concentrations. The isotope exchange experiments are carried out at constant RH and therefore assume radial homogeneity of the solute concentration allowing for a single adjustable parameter in the diffusion model. The mass transport model, on the other hand,

describes size changes in association with stepwise changes in RH and translational movement of water through radial concentration gradients.[9] Interpretation of the diffusion in the mass transport model requires analysis of the concentration gradient, which is nonlinear at low RH, as well as the size and refractive index that also involve multiple inter-dependent fitted parameters. The mass transport method requires a complex numeric treatment in the analysis of low RH experiments, while the linearity of the concentration gradient at high RH simplifies the analysis and makes the mass transport method simpler. In comparison, as noted earlier, the rapid diffusion rates, data acquisition rates and the time constant for switching between an H_2O and D_2O environment limits the experimental method presented here at high RH.

Lastly, our results are compared with both charge-neutral particles in the case of the isotope-exchange measurements of Price *et al.*[20] and Davies *et al.*[27] and charged particles in the mass-transport measurements of Zobrist *et al.*[37] The comparison suggests that the surface charge density on the droplets in this work (<40 elementary charges/μm^2) do not significantly influence D_2O diffusion into droplets. If the charge state significantly impacted the diffusion of D_2O into the droplet the best agreement can be expected between the results conducted in EDBs, which is not the case and instead good agreement was found between the measurements in neutral and charged microdroplets using the isotope labeling technique. Our results can be understood in the context of studies on the influence of charge on both ice nucleation and efflorescence. Homogeneous ice nucleation rates of pure water droplets were measured in a temperature-controlled EDB

as a function of temperature and absolute charge where the authors concluded that while the temperature strongly influenced the nucleation rate, no correlation with the surface charge was observed over a range of ±200 charges/μm^2.[33] The authors analyzed charge droplets with 10x greater surface charge density compared to the droplets in the current work and no interference of the charge with nucleation was found, in agreement with the suggestion that excess charges are not interfering with bulk processes such as diffusion within a droplet. Other new studies measured the dependence of efflorescence relative humidity on the magnitude of the surface charge in sodium chloride microdroplets and found no relationships below 500 elementary charges/μm^2, and a strong correlation only appears when the droplet exceeds this threshshold.[36] Molecular dynamics simulations in their study show that only above this charge density threshold, the charges interact with dissolved ionic species to form stable critical cluster sizes necessary for overcoming the energetic nucleation barrier at RH higher compared to neutral droplets. In the present work, the sucrose droplets contain surface charge density significantly below the threshold suggested by Hermann *et al.*[36] to impact efflorescence behavior. Furthermore, the presence of dissolved ionic species was essential for charges to impact the efflorescence humidity, which could explain why we do not observe charge-induced phenomena in droplets without ionic species similar to previous works in EDBs.[33,49] Future experiments on single aerosols containing ionic species, such as ternary mixtures of sucrose, water, and inorganic salts, are planned to investigate further the role excess charge may have on the rate of diffusion.

3.4 Conclusions

The translational water diffusion coefficient was measured in single charged sucrose droplets as a model system for sea spray aerosol at humidities ranging from 26-54 % RH at room temperature. A new method has been presented for quantifying water diffusion using H_2O/D_2O isotope tracing measured with Raman spectroscopy of a single charged droplet trapped in a humidity-controlled EDB. The measured water diffusion coefficients-molar concentration relationship follows an exponential dependence, described as a Vignes-type parameterization. The data were compared with previous studies of the sucrose-water system using the isotope exchange technique on neutral samples and a mass transport method on charged droplets. The comparison between our results and other Raman spectroscopy based methods shows good agreement of water diffusion coefficients across a wide range of sample sizes and volumes, suggesting the D_w values are not size-dependent. The agreement of this work using charged droplets in an EDB with neutral particles in an optical trap suggests that charge does not play a significant role under the conditions studies.

The Raman spectroscopic technique for isotope exchange analysis is limited to particle sizes greater than 1μm because of the low signal to noise ratio. Improvement of the sensitivity of the optical setup would be of great value in extending the present measurements to smaller aerosols with diameters of 50-200 nm, which are the size population most efficient for cloud activation[50,51] and therefore of large climate relevance. Experimental modifications to control temperature and particle charge will

reduce uncertainties in the diffusion measurements and allow a more detailed examination of charge effects. Temperature control will also serve for further comparisons of the method over a range of atmospherically relevant temperatures with the temperature-dependent D_w measurements made using the mass transport method,[37] as well as extending these measurements to examine the effect of viscosity and chemical composition on ice nucleation.

The importance of the present measurements is demonstration of the ability to measure water diffusion independently from viscosity under atmospherically relevant conditions. The isotope exchange method for measuring water diffusion rates can be applied to a variety of chemical systems and complexity including ternary mixtures of atmospheric relevance, the influence of hygroscopic inorganic salts, and concentration-dependent effects of monovalent and divalent cations found in sea spray aerosols.

Chapter 3, in full, has been submitted for publication of the material as it may appear as "Water Diffusion Measurements of Single Charged Aerosol Using H_2O/D_2O Isotope Exchange and Raman Spectroscopy in an Electrodynamic Balance," Nadler, Katherine A.; Huang, Dao-Ling; Kim, Pyeongeun; Xiong, Wei; Continetti, Robert E, 2018. The dissertation author was the primary investigator and author of this paper.

3.5 Supplementary Information

Supplementary Information Accompanying: "Water Diffusion Measurements of Single Charged Aerosol Using H_2O/D_2O Isotope Exchange and Raman Spectroscopy in an Electrodynamic Balance"

Authors: Katherine A. Nadler,[1] Dao-Ling Huang, [1] Pyeongeun Kim, [1] Wei Xiong, [1] Robert E. Continetti[1]

[1]Department of Chemistry and Biochemistry, University of California San Diego

Journal: Physical Chemistry Chemical Physics

Contact: Robert E. Continetti, rcontinetti@ucsd.edu

The Raman spectra are fit using a 7-term Gaussian expansion of the form:

$$Fit = \sum_{i=1}^{7} a exp\left(-\frac{(b-x)^2}{c^2}\right) \quad \text{(S3.1)}$$

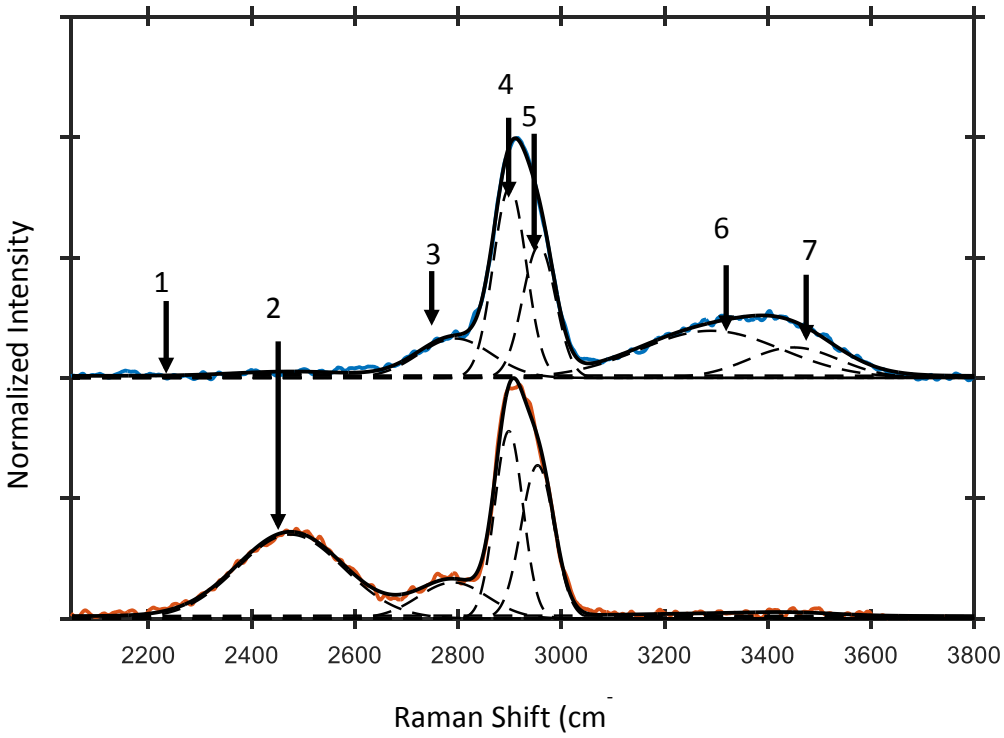

Figure 3.S1. Raman spectra collected during an isotope exchange experiment carried out at 50% RH at early (top) and late (bottom) time points. The spectra are deconstructed into 7 Gaussians as described in the manuscript, which are shown here individually.

Table 3.S1. Gaussian fit parameters for each of the 7 Gaussians in a single spectrum accompanying Figure S1 where *a*, *b,* and *c* follow Equation S1. The full dataset of fit parameters will be available in the Digital Collection.

Upper	Peak	a	b	c
	1	0.010	2915	2000
	2	0.017	2475	150
	3	0.164	2794	100
	4	0.791	2900	45
	5	0.549	2957	45
	6	0.196	3290	194
	7	0.127	3450	123

Lower	Peak	a	b	c
	1	0.012	2915	2000
	2	0.349	2475	145
	3	0.150	2790	95
	4	0.779	2898	39
	5	0.637	2954	45
	6	0.009	3290	200
	7	0.010	3450	120

The area of the ν(O-D), α, ν (C-H), and ν (O-H) peaks are calculated by the following equations:

$$Area_{OD} = Area_{Peak2} \tag{S3.2}$$

$$Area_{\alpha} = Area_{Peak3} \tag{S3.3}$$

$$Area_{CH} = Area_{Peak4} + Area_{Peak5} \tag{S3.4}$$

$$Area_{OH} = Area_{Peak6} + Area_{Peak7} \tag{S3.5}$$

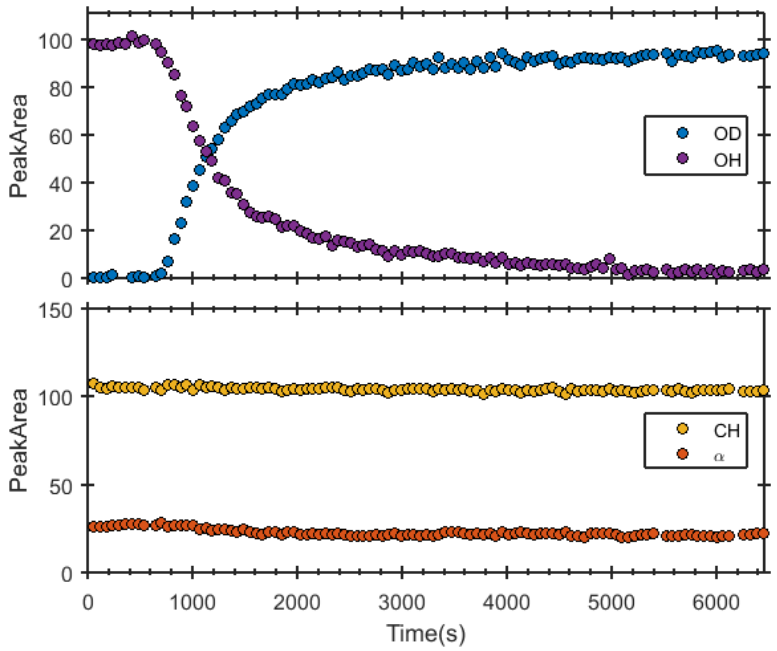

Figure 3.S2. Peak area calculations for an experiment carried out at 54% RH which shows the growth of the ν(O-D), decay of the ν(O-H), and the constant contributions for the ν(C-H) and α over time.

3.4 References

(1) Zobrist, B.; Marcolli, C.; Pedernera, D. A.; Koop, T. Do Atmospheric Aerosols Form Glasses? *Atmos. Chem. Phys.* 2008, *8* (17), 5221–5244.

(2) Orellana, M. V; Matrai, P. A.; Leck, C.; Rauschenberg, C. D.; Lee, A. M.; Coz, E. Marine Microgels as a Source of Cloud Condensation Nuclei in the High Arctic. *Proc. Natl. Acad. Sci. U. S. A.* 2011, *108* (33), 13612–13617.

(3) Virtanen, A.; Joutsensaari, J.; Koop, T.; Kannosto, J.; Yli-Pirila, P.; Leskinen, J.; Makela, J. M.; Holopainen, J. K.; Poschl, U.; Kulmala, M.; et al. An Amorphous Solid State of Biogenic Secondary Organic Aerosol Particles. *Nature* 2010, *467* (7317), 824–827.

(4) Jarvinen, E.; Ignatius, K.; Nichman, L.; Kristensen, T. B.; Fuchs, C.; Hoyle, C. R.; Hoppel, N.; Corbin, J. C.; Craven, J.; Duplissy, J.; et al. Observation of

Viscosity Transition in Alpha-Pinene Secondary Organic Aerosol. *Atmos. Chem. Phys.* 2016, *16* (7), 4423–4438.

(5) Shiraiwa, M.; Seinfeld, J. H. Equilibration Timescale of Atmospheric Secondary Organic Aerosol Partitioning. *Geophys. Res. Lett.* 2012, *39* (24), L24801.

(6) Davies, J. F.; Wilson, K. R. Nanoscale Interfacial Gradients Formed by the Reactive Uptake of OH Radicals onto Viscous Aerosol Surfaces. *Chem. Sci.* 2015, *6* (12), 7020–7027.

(7) Liu, P. F.; Li, Y. J.; Wang, Y.; Bateman, A. P.; Zhang, Y.; Gong, Z. H.; Bertram, A. K.; Martin, S. T. Highly Viscous States Affect the Browning of Atmospheric Organic Particulate Matter. *Acs Cent. Sci.* 2018, *4* (2), 207–215.

(8) Tong, H. J.; Reid, J. P.; Bones, D. L.; Luo, B. P.; Krieger, U. K. Measurements of the Timescales for the Mass Transfer of Water in Glassy Aerosol at Low Relative Humidity and Ambient Temperature. *Atmos. Chem. Phys.* 2011, *11* (10), 4739–4754.

(9) Bones, D. L.; Reid, J. P.; Lienhard, D. M.; Krieger, U. K. Comparing the Mechanism of Water Condensation and Evaporation in Glassy Aerosol. *Proc. Natl. Acad. Sci. U. S. A.* 2012, *109* (29), 11613–11618.

(10) Lienhard, D. M.; Huisman, A. J.; Krieger, U. K.; Rudich, Y.; Marcolli, C.; Luo, B. P.; Bones, D. L.; Reid, J. P.; Lambe, A. T.; Canagaratna, M. R.; et al. Viscous Organic Aerosol Particles in the Upper Troposphere: Diffusivity-Controlled Water Uptake and Ice Nucleation? *Atmos. Chem. Phys.* 2015, *15* (23), 13599–13613.

(11) Ignatius, K.; Kristensen, T. B.; Jarvinen, E.; Nichman, L.; Fuchs, C.; Gordon, H.; Herenz, P.; Hoyle, C. R.; Duplissy, J.; Garimella, S.; et al. Heterogeneous Ice Nucleation of Viscous Secondary Organic Aerosol Produced from Ozonolysis of Alpha-Pinene. *Atmos. Chem. Phys.* 2016, *16* (10), 6495–6509.

(12) Grayson, J. W.; Song, M.; Sellier, M.; Bertram, A. K. Validation of the Poke-Flow Technique Combined with Simulations of Fluid Flow for Determining Viscosities in Samples with Small Volumes and High Viscosities. *Atmos. Meas. Tech.* 2015, *8* (6), 2463–2472.

(13) Renbaum-Wolff, L.; Grayson, J. W.; Bertram, A. K. Technical Note: New Methodology for Measuring Viscosities in Small Volumes Characteristic of Environmental Chamber Particle Samples. *Atmos. Chem. Phys.* 2013, *13* (2), 791–802.

(14) Song, Y. C.; Haddrell, A. E.; Bzdek, B. R.; Reid, J. P.; Barman, T.; Topping, D. O.; Percival, C.; Cai, C. Measurements and Predictions of Binary Component Aerosol Particle Viscosity. *J. Phys. Chem. A* 2016, *120* (41), 8123–8137.

(15) Power, R. M.; Simpson, S. H.; Reid, J. P.; Hudson, A. J. The Transition from Liquid to Solid-like Behaviour in Ultrahigh Viscosity Aerosol Particles. *Chem. Sci.* 2013, *4* (6), 2597–2604.

(16) Jayarathne, T.; Sultana, C. M.; Lee, C.; Malfatti, F.; Cox, J. L.; Pendergraft, M. A.; Moore, K. A.; Azam, F.; Tivanski, A. V; Cappa, C. D.; et al. Enrichment of Saccharides and Divalent Cations in Sea Spray Aerosol During Two Phytoplankton Blooms. *Environ. Sci. Technol.* 2016, *50* (21), 11511–11520.

(17) Kumar, S. K.; Szamel, G.; Douglas, J. F. Nature of the Breakdown in the Stokes-Einstein Relationship in a Hard Sphere Fluid. *J. Chem. Phys.* 2006, *124* (21), 214501.

(18) Molinero, V.; Goddard, W. A. Microscopic Mechanism of Water Diffusion in Glucose Glasses. *Phys. Rev. Lett.* 2005, *95* (4), 045701.

(19) Zhu, L.; Cai, T.; Huang, J.; Stringfellow, T. C.; Wall, M.; Yu, L. Water Self-Diffusion in Glassy and Liquid Maltose Measured by Raman Microscopy and NMR. *J. Phys. Chem. B* 2011, *115* (19), 5849–5855.

(20) Price, H. C.; Murray, B. J.; Mattsson, J.; O'Sullivan, D.; Wilson, T. W.; Baustian, K. J.; Benning, L. G. Quantifying Water Diffusion in High-Viscosity and Glassy Aqueous Solutions Using a Raman Isotope Tracer Method. *Atmos. Chem. Phys.* 2014, *14* (8), 3817–3830.

(21) Hopkins, R. J.; Mitchem, L.; Ward, A. D.; Reid, J. P. Control and Characterisation of a Single Aerosol Droplet in a Single-Beam Gradient-Force Optical Trap. *Phys. Chem. Chem. Phys.* 2004, *6* (21), 4924–4927.

(22) Chylek, P.; Ramaswamy, V.; Ashkin, A.; Dziedzic, J. M. Simultaneous Determination of Refractive-Index and Size of Spherical Dielectric Particles from Light-Scattering Data. *Appl. Opt.* 1983, *22* (15), 2302–2307.

(23) Ray, A. K.; Souyri, A.; Davis, E. J.; Allen, T. M. Precision of Light-Scattering Techniques for Measuring Optical-Parameters of Microspheres. *Appl. Opt.* 1991, *30* (27), 3974–3983.

(24) Dennis-Smither, B. J.; Miles, R. E. H.; Reid, J. P. Oxidative Aging of Mixed Oleic Acid/Sodium Chloride Aerosol Particles. *J. Geophys. Res.* 2012, *117*, D20204.

(25) Dennis-Smither, B. J.; Marshall, F. H.; Miles, R. E. H.; Preston, T. C.; Reid, J. P. Volatility and Oxidative Aging of Aqueous Maleic Acid Aerosol Droplets and the Dependence on Relative Humidity. *J. Phys. Chem. A* 2014, *118* (30), 5680–5691.

(26) Cai, C.; Stewart, D. J.; Reid, J. P.; Zhang, Y. H.; Ohm, P.; Dutcher, C. S.; Clegg, S. L. Organic Component Vapor Pressures and Hygroscopicities of Aqueous Aerosol Measured by Optical Tweezers. *J. Phys. Chem. A* 2015, *119* (4), 704–718.

(27) Davies, J. F.; Wilson, K. R. Raman Spectroscopy of Isotopic Water Diffusion in Ultraviscous, Glassy, and Gel States in Aerosol by Use of Optical Tweezers. *Anal. Chem.* 2016, *88* (4), 2361–2366.

(28) Davies, J. F.; Haddrell, A. E.; Reid, J. P. Time-Resolved Measurements of the Evaporation of Volatile Components from Single Aerosol Droplets. *Aerosol Sci. Technol.* 2012, *46* (6), 666–677.

(29) Davies, J. F.; Miles, R. E. H.; Haddrell, A. E.; Reid, J. P. Influence of Organic Films on the Evaporation and Condensation of Water in Aerosol. *Proc. Natl. Acad. Sci. U. S. A.* 2013, *110* (22), 8807–8812.

(30) Miles, R. E. H.; Davies, J. F.; Reid, J. P. The Influence of the Surface Composition of Mixed Monolayer Films on the Evaporation Coefficient of Water. *Phys. Chem. Chem. Phys.* 2016, *18* (29), 19847–19858.

(31) Davies, J. F.; Miles, R. E. H.; Haddrell, A. E.; Reid, J. P. Temperature Dependence of the Vapor Pressure and Evaporation Coefficient of Supercooled Water. *J. Geophys. Res.* 2014, *119* (18), 10931–10940.

(32) Vortisch, H.; Kramer, B.; Weidinger, I.; Woste, L.; Leisner, T.; Schwell, M.; Baumgartel, H.; Ruhl, E. Homogeneous Freezing Nucleation Rates and Crystallization Dynamics of Single Levitated Sulfuric Acid Solution Droplets. *Phys. Chem. Chem. Phys.* 2000, *2* (7), 1407–1413.

(33) Kramer, B.; Hubner, O.; Vortisch, H.; Woste, L.; Leisner, T.; Schwell, M.; Ruhl, E.; Baumgartel, H. Homogeneous Nucleation Rates of Supercooled Water Measured in Single Levitated Microdroplets. *J. Chem. Phys.* 1999, *111* (14), 6521–6527.

(34) Stockel, P.; Vortisch, H.; Leisner, T.; Baumgartel, H. Homogeneous Nucleation of Supercooled Liquid Water in Levitated Microdroplets. *J. Mol. Liq.* 2002, *96–7*, 153–175.

(35) Tong, H. J.; Ouyang, B.; Nikolovski, N.; Lienhard, D. M.; Pope, F. D.; Kalberer, M. A New Electrodynamic Balance (EDB) Design for Low-Temperature Studies: Application to Immersion Freezing of Pollen Extract Bioaerosols. *Atmos. Meas. Tech.* 2015, *8* (3), 1183–1195.

(36) Hermann, G.; Zhang, Y.; Wassermann, B.; Fischer, H.; Quennet, M.; Ruhl, E. Charge Effects on the Efflorescence in Single Levitated Droplets. *J. Phys. Chem. A* 2017, *121* (36), 6790–6799.

(37) Zobrist, B.; Soonsin, V.; Luo, B. P.; Krieger, U. K.; Marcolli, C.; Peter, T.; Koop, T. Ultra-Slow Water Diffusion in Aqueous Sucrose Glasses. *Phys. Chem. Chem. Phys.* 2011, *13* (8), 3514–3526.

(38) Schlemmer, S.; Illemann, J.; Wellert, S.; Gerlich, D. Nondestructive High-Resolution and Absolute Mass Determination of Single Charged Particles in a Three-Dimensional Quadrupole Trap. *J. Appl. Phys.* 2001, *90* (10), 5410.

(39) Trevitt, A. J.; Wearne, P. J.; Bieske, E. J. Calibration of a Quadrupole Ion Trap for Particle Mass Spectrometry. *Int. J. Mass Spectrom.* 2007, *262* (3), 241–246.

(40) Salomon, M. *Thermodynamic Properties of Liquid H2O and D2O and Their Mixtures*; United States. National Aeronautics and Space Administration. "NASA Technical Note." Print.: Washington, D.C., 1969.

(41) Glantschnig, W. J.; Chen, S. H. Light-Scattering From Water Droplets in the Geometrical-Optics Approximation. *Appl. Opt.* 1981, *20* (14), 2499–2509.

(42) Norrish, R. S. An Equation for the Activity Coefficients and Equilibrium Relative Humidities of Water in Confectionery Syrups. *J. Food Sci. Technol.* 1966, *1*, 25–39.

(43) Chirife, J.; Ferro Fontan, C.; Benmergui, E. A. The Prediction of Water Activity in Aqueous Solutions in Connection with Intermediate Moisture Foods IV. Aw Prediction in Aqueous Non Electrolyte Solutions. *J. Food Technol.* 1980, *15*, 59–70.

(44) Lide, D. R. *CRC Handbook of Chemistry and Physics. 79th Ed.*; CRC Press Inc.: Boca Raton, FL, 1998.

(45) Halbout, J. M.; Tang, C. L. Phase-Matched 2nd-Harmonic Generation in Sucrose. *IEEE J. Quantum Electron.* 1982, *18* (3), 410–415.

(46) Moridnejad, A.; Preston, T. C. Models of Isotopic Water Diffusion in Spherical Aerosol Particles. *J. Phys. Chem. A* 2016, *120* (49), 9759–9766.

(47) Kohen, A.; Limbach, H. H. *Isotope Effects in Chemistry and Biology*; Taylor & Francis: Boca Raton, FL, 2010.

(48) Vignes, A. Diffusion in Binary Solutions - Variation of Diffusion Coefficient with Composition. *Ind. Eng. Chem. Fundam.* 1966, *5* (2), 189–199.

(49) Rzesanke, D.; Nadolny, J.; Duft, D.; Muller, R.; Kiselev, A.; Leisner, T. On the Role of Surface Charges for Homogeneous Freezing of Supercooled Water Microdroplets. *Phys. Chem. Chem. Phys.* 2012, *14* (26), 9359–9363.

(50) Komppula, M.; Lihavainen, H.; Kerminen, V. M.; Kulmala, M.; Viisanen, Y. Measurements of Cloud Droplet Activation of Aerosol Particles at a Clean Subarctic Background Site. *J. Geophys. Res.* 2005, *110*, D06204.

(51) Che, H. C.; Zhang, X. Y.; Zhang, L.; Wang, Y. Q.; Zhang, Y. M.; Shen, X. J.; Ma, Q. L.; Sun, J. Y.; Zhong, J. T. Prediction of Size-Resolved Number Concentration of Cloud Condensation Nuclei and Long-Term Measurements of Their Activation Characteristics. *Sci. Rep.* 2017, *7* (1), 5819.

CHAPTER 4: Water Diffusion Measurements of Ternary Mixtures in Single Charged Aerosol Using H_2O/D_2O Isotope Exchange

4.1 Introduction

Sea spray aerosols (SSA) are produced from breaking waves in the ocean and contribute a significant fraction of the natural aerosol in the atmosphere. SSA impact the climate by directly scattering and absorbing incoming solar radiation and through indirect processes by acting as efficient cloud condensation and ice nuclei, particularly over remote oceans far from terrestrial particle sources. However, the accuracy of global climate models in predicting radiative forcing of marine-derived aerosols is limited by our understanding of the microphysical properties, such as viscosity, which govern aerosol-cloud interactions.[1] The viscosity of aerosols impacts the diffusion rates of molecular components which affect the rate of hygroscopic growth.[2,3] Despite the complexity of ambient aerosol, laboratory studies on model systems are crucial for understanding of how mixed chemical systems impact climate relevant properties. Further, the expansion of simple model systems to incorporate ternary mixtures will lead

to improved parameterizations of component interactions on aerosol physicochemical properties.

The chemical composition of SSA consists of inorganic and organic compounds, where the fraction of organic mass can achieve >0.9 in submicron populations.[4] Analysis of the molecular identity of organic content has revealed significant amounts of long-chain fatty acids, short-chain fatty acids, free saccharides, poly- and oligo-saccharides, and siliceous material.[4–6] Although nascent SSA exhibit complex chemical compositions, phase states, and size, it is useful to perform laboratory measurements using simple model systems to better understand how chemical composition and humidity impact physicochemical properties.

Recently, the discovery of highly viscous and amorphous biogenic aerosol[7,8] has attracted attention due to slow kinetics governing chemical change in these systems.[9–11] This propelled the development of a number of experimental techniques for measuring viscosity in the aerosol phase[7,10,12–16] which is typically supersaturated with respect to the solubility limit and cannot be accessed using traditional methods.[17] The techniques have been deployed for measuring viscosity in a number of ambient and laboratory model systems and demonstrate high viscosity, semi-solid and glassy regimes can be accessed at low relative humidity (RH) and temperature. High viscosity has also been shown to reduce heterogeneous reaction rates,[18,19] impede hygroscopic growth,[14,20] and enhance ice nucleation.[21,22] which are directly related to its atmospheric impacts, such as its light scattering and absorption efficiency and CCN efficiency.

The viscosity of a number of binary model systems have been studied at controlled RH and temperature, including saccharides, alcohols, and fatty acids.[16,23,24] Results reveal an increase in viscosity with increased molecular weight, carbon chain length, and number of hydroxyl groups,[25] contributing to the database of organic compounds with atmospheric relevance. However, Song *et al.* showed that model predictions of the RH-dependent viscosity could not reproduce experimental results above 1 Pa s.[16]

A few viscosity measurements have been carried out on ternary mixture aerosol systems.[14,24,26] Power *et al.* shows that varying the molar ratio of sucrose to NaCl in a ternary mixture leads to a difference in viscosity by several orders of magnitude compared to the sucrose-water binary mixture alone.[14] The data are compared with model predictions using the Chenlo *et al.*[27] parameterization of viscosity with molality of NaCl and sucrose, the Norrish[28] parameterization for the water activity of sucrose, ADDEM model,[29,30] and the simple additivity mixing rules of Zandovskii-Stokes Robinson (ZSR).[31] The poor agreement between the model predictions and data are attributed to the sucrose molecules disproportionately increasing the viscosity by dominating the mechanical properties of the mixture. In another study, Marsh *et al.* investigated the temperature and RH-dependent viscosity for ternary citric acid-sucrose-water and $NaNO_3$-sucrose-water aerosol model systems, which similarly displayed a decrease in viscosity with the addition of a hygroscopic molecule due to the plasticizing effect of the water.[26] Increasing the complexity of model systems is important for testing the

application of mixing rules, and for providing data which are used to improve predictive models.

The mobility of molecular components in an aerosol is related to viscosity and significantly impacts the kinetics of evaporation and condensation processes,[14,32] as well as the extent of heterogeneous reactions.[33] Specifically water diffusion coefficients are important for modeling cloud activation as the translational movement of the water into the particle is necessary for growth to occur.[34] If the water mobility is severely limited, the aerosol may not achieve activation, which has significant climate implications. The Stokes-Einstein (S-E) relation is used to calculate the diffusion coefficient, *D,* from viscosity given by:

$$D = \frac{k_B T}{6\pi a \eta} \tag{4.1}$$

where k_B is Boltzmann's constant, T (K) is temperature, a is the radius of the diffusing species, and η is the dynamic viscosity (Pa·s). The S-E relation has been widely used for low viscosity, bulk liquid systems and therefore has been applied as a first approximation in aerosols using viscosity measurements. The relationship has shown good agreement for the sucrose diffusion coefficient in a sucrose-water matrix even at high viscosity in bulk solutions.[35] However, the general application of the Stokes-Einstein relationship to aerosols has been shown to under predict the diffusion coefficient and provides only a lower bound for small molecules, such as water, because of their ability to percolate through channels in viscous matrices.[24,36,37] Therefore, techniques which measure water

diffusion independent from viscosity are necessary to accurately predict evaporation, condensation, and cloud activation processes.

In recent years the diffusion coefficient of water in binary and ternary aerosol mixtures has been measured using new techniques which study single, levitated aerosol. The mass transport method uses optical tweezers or an electrodynamic balance (EDB) to trap single, micrometer-sized aqueous droplets and spectroscopically measure the size change in response to stepwise jumps in the relative humidity.[14,38,39] The kinetic response of water evaporating or condensing on the droplet becomes slow at high viscosity and is strongly dependent on the diffusion coefficient of water. The size response curves as a function of time were interpreted using a theoretical framework based on principles of mass transport. This treatment applies a numerical analysis that divides the particle into a discrete number of concentric shells, characterized by a solute concentration and diffusion coefficient. As the droplet responds to a jump in RH, a highly nonlinear radial concentration gradient forms because the aerosol liquid-air interface is assumed to reach equilibrium instantaneously while the center of the droplet remains at the initial water concentration. The timescales for the concentration gradient to diminish are related to the water diffusion coefficient, which is a strong function of concentration. Using an iterative approach that accounts for the average concentration of the neighboring shells, the value of D_w is inferred.[38,40] Approaching high viscosity, the numerical treatment for the retrieval of the diffusion coefficient must incorporate additional fitting parameters because the refractive index, necessary for the size calculation, also becomes a parameter that varies rapidly in the presence of the steep concentration gradient. At these low RH,

high viscosity regimes, an increase in the uncertainty by an order of magnitude reduces the accuracy of the diffusion measurements.[41] Nevertheless, the method has been applied to a number of binary and ternary chemical systems, highlighting the breakdown of the S-E relation by several orders of magnitude in citric acid, sucrose, and α-pinene SOA.[42]

Another technique called the Raman isotope tracer method measures the diffusion coefficient by tracking the translational movement of an isotopically-labeled molecule, measured by a change in intensity of vibrational peaks in the Raman spectrum. The method was first applied on substrate-deposited aqueous disks with D_2O as the tracer species for maltose and sucrose solutions.[43,44] Davies *et al.* then applied the isotopic exchange technique together with aerosol optical tweezers for single-particle levitation[45] reducing the sample size to less than 6 μm radius, speeding up the experimental timescales from weeks to hours. The optical tweezers isotopic tracer experiments were carried out at a constant RH, and therefore constant aerosol size and solute concentration. Fick's second law of diffusion applied to a sphere was used to model the time-dependent intensities of the ν(O-D) and ν(O-H) Raman peaks to quantify the diffusion coefficient as a function of concentration, or water activity, in sucrose, citric acid, sucrose/citric acid mixtures, and shikimic acid.[45] The results were modeled using a Vignes-type parameterization[46] describing the water diffusion coefficient, D_w, as a mass fraction-weighted exponential function dependent on the self-diffusion coefficient of water, 2 x 10^{-9} m^2/s, and the empirically determined self-coefficient in the limit of pure solute component, $D^0_{w,s}$ for different molecular compositions. In ternary mixtures of sucrose-

citric acid the $D^0_{w,s}$ was determined to be a log-linear function of mass fraction, allowing an effective mixed-solute $D^0_{w,s}$ to satisfy a Vignes fit without requiring an activity coefficient correction. The results presented by Davies *et al.*[45] suggest the practicality of applying the isotope tracer method in conjunction with a single particle confinement technique for measuring water diffusion in a variety of atmospherically-relevant viscous aerosols.

We present water diffusion measurements on ternary aqueous NaCl-sucrose and $CaCl_2$-sucrose mixtures using the isotope exchange method applied to single, charged microdroplets in an electrodynamic balance. The current database of available water diffusion measurements in binary and ternary mixtures is severely limited, which in turn propels the application of the S-E relation to new systems because no direct diffusion data are available. The results are interpreted using the application of Fick's second law of diffusion applied to a sphere for determining the concentration-dependent water diffusion coefficient and are modeled using a semi-empirical Vignes-type fit, as presented below following a discussion of the experimental technique.

4.2 Experimental

Water diffusion measurements on ternary mixtures of sucrose, water, and inorganic salt (NaCl and $CaCl_2$) were performed on single charged microdroplets trapped in a temperature and RH controlled electrodynamic balance (EDB). The experimental setup has been described previously[47] in detail and will be briefly outlined, followed by

an explanation of the parameterizations for density and refractive index used to analyze the spectroscopic measurements for calculating the concentration-dependent water diffusion coefficient.

The EDB allows trapping of single charged aerosol at the center of an electrodynamic trap for interrogation by a 532 nm laser allowing spectroscopic analysis of the aerosol morphology, size, and chemical composition over time. Shown in Figure 4.1A, the trap is composed of two conical endcap electrodes and eight concentric rod electrodes providing a wide optical access for laser irradiation and signal collection. The AC potential is applied to the endcap electrodes, typically V_p = 1500 V, f = 100 – 200 Hz, and a DC potential, typically 150 – 400 V, is applied to the two rod electrodes directly below the trap center to offset the gravitational force of the microdroplet. The remaining six rods are grounded, creating an effective quadrupolar electric field which tightly confines the microdroplet in space. The EDB is built on stainless steel octagonal plates for preservation of the optical access and is isolated from the surrounding air in the chamber by a set of stainless steel plates outfitted with windows. The primary mounting structure is augmented with a secondary Teflon housing which provides a channel from the droplet generator located above the chamber to the trap, and acts to further insulate the trapping volume humidity and temperature. An electronic shutter seals off the chamber from laboratory air and is opened to allow a new droplet to be trapped.

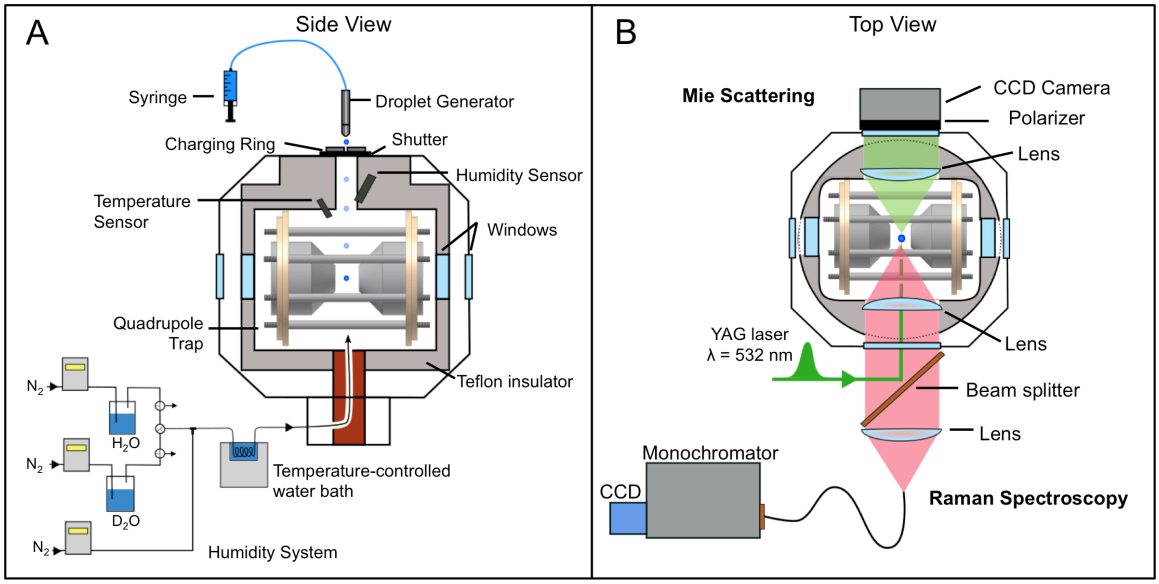

Figure 4.1. A) Experimental setup of the electrodynamic balance (EDB) apparatus contained in a secondary Teflon housing inside an environmental chamber and equipped with a droplet generator and dual bubbler RH control. B) Optical layout with a trapped droplet irradiated with a pulsed 532 nm laser and the forward Mie elastic scattering collected on a CCD camera and the back-scattered Raman is focused into a fiber optic cable mounted to a monochromator equipped with a CCD detector.

Aqueous solutions of 1:1 molar NaCl-sucrose and 1:1 molar $CaCl_2$-sucrose (Fisher Chemical for all compounds) were prepared using DI water. The solutions were filtered using a 0.05 µm PTFE syringe filter to remove undissolved precipitates and aspirated into the capillary of a piezoelectric droplet generator (Engineering Arts DEO3) equipped with a 67 µm diameter orifice (DH067). Single droplets are generated on-demand with computer-controlled drive electronics and are inductively charged upon generation from an electric field applied between a DC charging ring electrode and the electrically grounded capillary tip. Droplets are produced with an initial diameter of

approximately 67 μm and carry a surface charge density of approximately 10 – 30 elementary charges/μm^2. Stabilization of a single droplet at the center of the EDB is performed by adjusting the AC frequency until minimal harmonic oscillation motion is observed.

The relative humidity in the trap is controlled with digital mass flow controllers (Alicat MC-500SCCM) by mixing N_2 with the humidified vapor headspace of a bubbler containing water. The humidified air is directed through a copper coil submerged in a water bath, which is temperature-regulated by a water chiller (Neslab CFT-25), and subsequently guided into the chamber and flown vertically over the trapped droplet. Two bubblers, one containing distilled H_2O and a second containing high purity D_2O (>99.8% D atom, Acros Organics), are arranged using 3-way valves so that air from one bubbler is selected to flow into the chamber while flow lines from the second bubbler are equilibrated is exhausted. Experiments are carried out at constant RH by first trapping a single sucrose droplet in H_2O RH and allowing sufficient time for equilibration. Then D_2O vapor at the same RH is introduced to the chamber, replacing the gas-phase H_2O in the trap and eventually diffusing into the droplet to replace the condensed-phase H_2O. During each experimental run the H_2O humidified air is initially directed into the chamber for droplet equilibration while the D_2O bubbler is exhausted to fill intermediate tubing lines, reducing changes in RH during the gas transition in the trap. The relative humidity and temperature are monitored using a humidity probe (Vaisala HMP60) located approximately 25 mm downstream of the RH flow with ±1.5% RH and ±1 °C

accuracy, respectively. For each water diffusion measurement the relative humidity is maintained constant to ±1%, or within the error of the probe. A custom LabView control and data acquisition program monitors the trap settings and environmental conditions every 1 s. When the chamber atmosphere is switched to D_2O the humidity probe measurement must be corrected for the difference in equilibrium vapor pressure of D_2O versus H_2O[48] as shown in Eqn (4.1) where A = -0.30661, B = 9.14056, and C = 75.753 and T is in Celsius.

$$\ln\left(\frac{p^0_{H_2O}}{p^0_{D_2O}}\right) = A + \frac{B}{C+T} \tag{4.1}$$

The trapped droplet is continuously irradiated to provide spectroscopic characterization of size using Mie scattering and evolving chemical composition from H_2O to D_2O using Raman spectroscopy. Shown in Figure 1B, an 80 kHz 532 nm laser (RPMC Wedge XF) is reflected off of a broadband mirror and 532 nm laser edge beamsplitter and focused in the center of the trap; the elastic Mie scattering is collected over a solid angle of 24.5° centered at 45° in the forward-scattering direction relative to the laser propagation direction and imaged onto a monochromatic CCD camera at a rate of 30 Hz. The back-scattered Raman signal is collected using *f/2* optics, transmitted through a 532 nm laser edge beam splitter, and focused into a fiber optic cable coupled into a monochromator (Acton SpectraPro 275) outfitted with a 600 g/mm grating and an open-electrode TE-cooled CCD detector (Horiba Syncerity). The integration time for each Raman spectrum is 60-120 s to achieve adequate signal-to-noise ratio.

Mie theory is applied to calculate the size of spherical particles from the angular-resolved elastic scattering intensity with high accuracy.[49] When the particle radius is significantly larger than the laser wavelength, the geometric optics approximation may be used where the evenly spaced bands evident in the Mie angular intensity spectrum are processed via FFT to calculate the average angular spacing of the bands, $\Delta\theta$ (radian^{-1}), for determining the droplet radius, r:[50]

$$r = \frac{\lambda}{\Delta\theta}\left(\cos\left(\frac{\theta}{2}\right) + \frac{n\sin\left(\frac{\theta}{2}\right)}{\sqrt{1+n^2-2n\cos\left(\frac{\theta}{2}\right)}}\right)^{-1} \quad (4.2)$$

where λ is the laser wavelength (μm), n is the refractive index of the droplet, and θ is the median scattering angle (radian). The treatment of the refractive index parameterization for ternary mixtures is described in Section 4.3.2.

4.3 Results and Discussion

The RH-dependent water diffusion coefficient is calculated for ternary aerosol mixtures using isotope exchange from the quantification of the time-dependent D_2O concentration and droplet size. The timescales for diffusion into a sphere are dependent on radius, and an accurate calculation for the size using the geometric optics approximation requires parameterizations of index of refraction as a function of mass

fraction of the solutes. The treatments for binary mixture mass fraction solute with RH are introduced followed by descriptions for calculating the mass fraction and density of ternary mixtures Additionally, the aerosol density is used for calculating the predicted diffusion coefficients from viscosity *via* the Stokes-Einstein relation.

4.3.1 Parameterizations of the mass fraction and density

The calculation of the index of refraction as a function of varying RH requires parameterization of the mass fraction solute (MFS) and density (ρ). The dependence of MFS on water activity, a_w, has been well studied for binary sucrose aqueous solutions and the treatment by Norrish[3] has been shown to correlate with experimental measurements over the entire RH range:

$$a_w = x_w \exp(k x_s^2) \tag{4.3}$$

where x_w and x_s are the mole fractions of water and sucrose, respectively, and k is an empirical constant equal to -6.47 for sucrose.[420] The impact of the choice for mass fraction sucrose treatment is explored by comparison with the widely-used Aerosol Inorganic-Organic Mixtures Functional groups Activity Coefficients (AIOMFAC), a general thermodynamic activity coefficient model based on a modified Universal quasichemical Functional group Activity Coefficients (UNIFAC) functional group contribution model.[51,52] and verified with experimental data from wide range of

atmospheric inorganic and organic compounds. The density of the binary sucrose-water solution with mass fraction is calculated following Zobrist *et al.*:[38]

$$\rho_s = a + b_1 MFS + b_2 MFS^2 + b_3 MFS^3 + b_4 MFS^4 \quad (4.4)$$

where a = 0.9989, b_1 = 0.3615, b_2 = 0.02964, b_3 = -0.3186 and b_4 = 0.24191. The mass fraction of the binary NaCl-H_2O solution is calculated using AIOMFAC[51,52] and the density treatment is from an empirically-derived fit provided by Tang *et al.*[53]

$$\rho_{NaCl} = a + b_1 MFS + b_2 MFS^2 + b_3 MFS^3 + b_4 MFS^4 \quad (4.5)$$

where MFS is expressed in percent and a = 0.9971, b_1 = 7.41x10^{-3}, b_2 = -3.741x10^{-5}, b_3 = 2.252x10^{-6} and b_4 = -2.06x10^{-8}. The mass fraction of the binary $CaCl_2$-H_2O solution was also calculated using AIOMFAC.[51,52] Then, the ternary mixture density is calculated using the volume additivity rule described by Tang *et al.*[53] Figure 4.2 shows the difference between the Norrish and the AIOMFAC treatments for the MFS of sucrose as a function of RH in a binary aqueous mixture (A), which has been converted into molality (B), and the density of the ternary 1:1 molar ratio NaCl-sucrose-water mixture (C). It is worth noting that while the difference between the treatments in mass fraction solute, particularly below 30% RH, is less than 0.05, the conversion to molality results in a significant difference with the AIOMFAC because of the large molar mass of sucrose compared to water, predicting a higher molality of greater than 20 mol/kg below 20% RH where measurements in this study were conducted. The Norrish treatment was shown by

Power *et al.*[24] to best represent their sucrose viscosity measurements, and recently it was recognized by Rickards *et al.*[54] to yield excellent agreement for the modeling of viscosity when comparing numerous sucrose-MFS treatments. While numerous treatments of the equilibrium solution properties for sucrose are found in the literature,[54] the AIOMFAC was chosen for comparison due to the thermodynamic basis and extensive and rigorous validation with inorganic-organic mixed component experiments.[51]

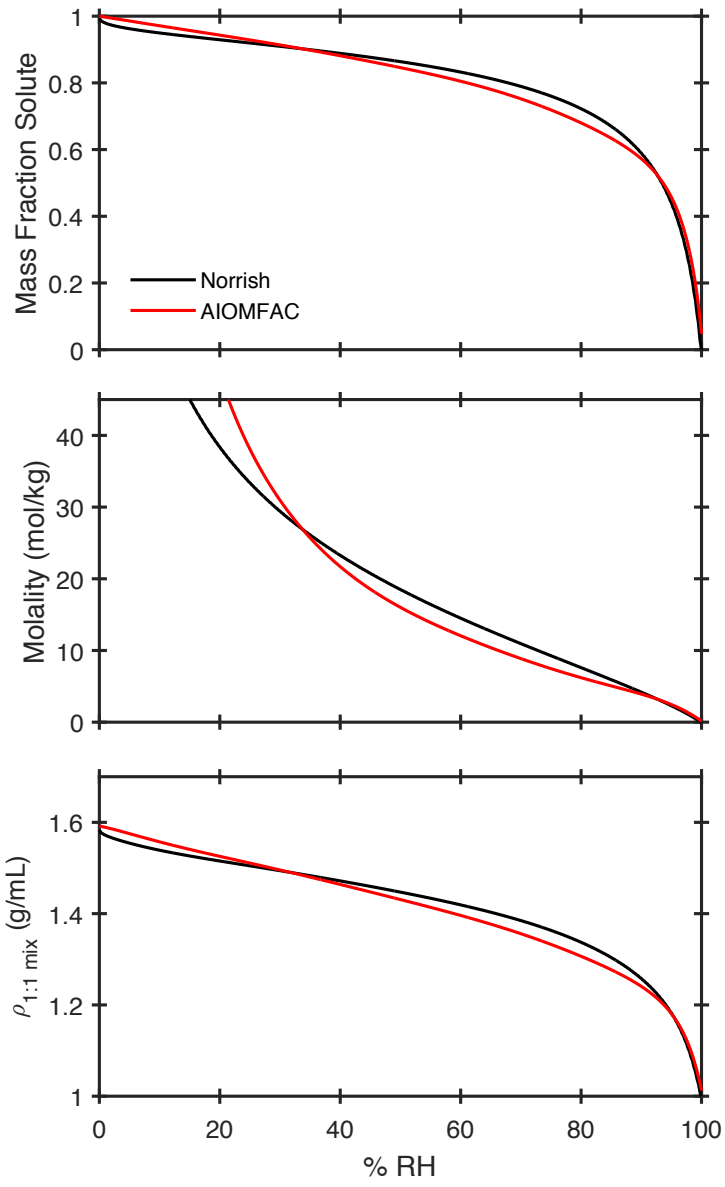

Figure 4.2. Comparison of the Norrish treatment[28] (black) and AIOMFAC calculations[52] (red) for (A) mass fraction solute as a function of % RH for the sucrose-water mixture, (B) molality of the sucrose-water mixture, and (C) the ternary 1:1 molar ratio NaCl-sucrose mixture.

In order to apply the S-E relation for the water diffusion coefficients in ternary NaCl-sucrose mixtures, the viscosity must be calculated. The kinematic viscosity, defined as the ratio between dynamic viscosity and density, was calculated for sucrose, NaCl, and varying mixing ratios by Chenlo *et al.*[27] and the parameterization has been extrapolated to concentrations achieved in aerosols.[14,20,24,54] The dynamic viscosity, hereafter referred to as viscosity, is calculated from the Chenlo parameterization and mixed solution density, shown in Figure 4.3, as a function of RH using the Norrish (black) and AIOMFAC (red) treatments for sucrose and AIOMFAC for NaCl. The binary sucrose-water viscosity is shown as a dashed line, compared with recent parameterizations determined from measurements by Song *et al.*[16] using holographic optical tweezers and Grayson *et al.,*[23] who compiled measurements from a number of sources and reported an empirical fit up to 10^9 Pa·s. The prediction for the ternary 1:1 molar NaCl-sucrose aqueous mixture are also shown (solid lines), and found to be several orders of magnitude lower in viscosity compared to binary sucrose mixtures. Power *et al.*[24] measured the viscosity using holographic optical tweezers coalescence and reported measurements of binary sucrose-H_2O and NaCl-H_2O mixtures, and molar ratios between 1:4 and 4:1 for NaCl-sucrose-H_2O ternary mixtures. of the results they obtained for the binary mixtures agreed well with the predictions of Chenlo *et al.* given the extrapolation to concentrations (>30 mol/kg) well beyond the values (4.5 mol/kg) of the original experiment. However, the ternary viscosity model using the Norrish and Chenlo treatments and ZSR[31] for estimating the water content of the mixture underpredicted the experimental measurements, with a deviation of greater than an order of magnitude at 40% RH.

Compared to other parameterizations of Starzak & Peacock[55] and Quintas *et al.*,[56] the Norrish and Chenlo combination provided the best agreement, although empirical best fit parameterizations were not provided. The viscosity parameterizations for the binary sucrose-water and ternary NaCl-sucrose-water mixtures are implemented in the S-E relation for the estimation of water diffusion coefficients and are compared to the direct measurements reported here.

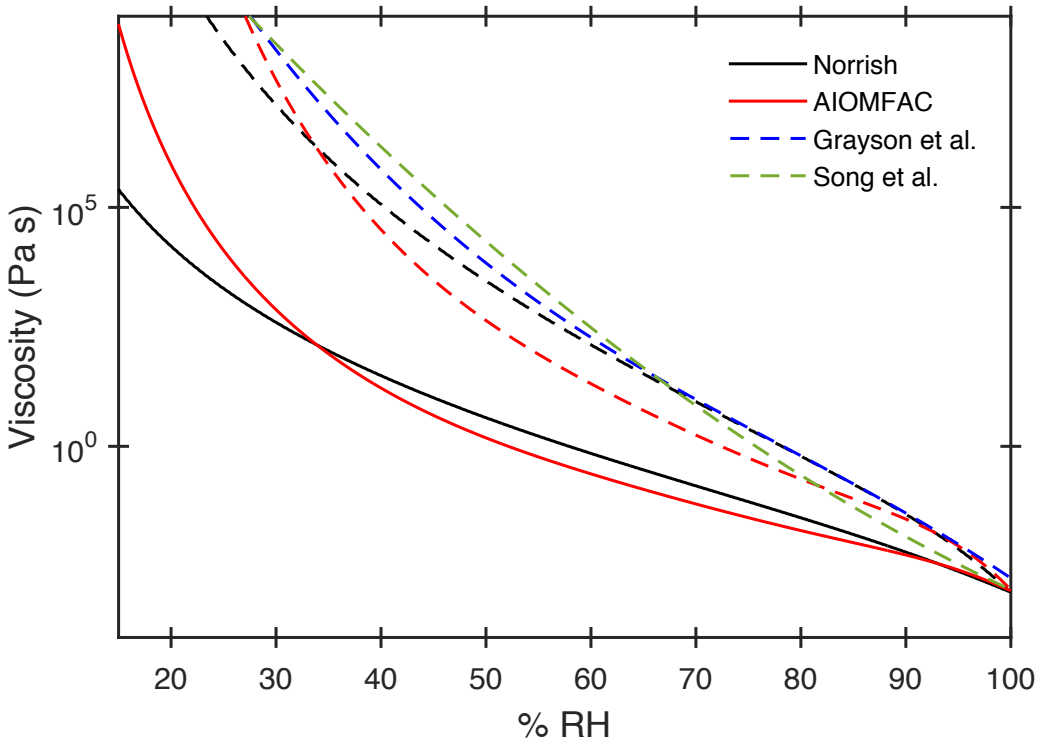

Figure 4.3. Parameterizations for viscosity of binary sucrose-water (all dashed lines) and 1:1 NaCl-sucrose mixture (solid) as a function of RH using the Norrish and AIOMFAC treatments, compared to the empirical parameterizations of Grayson *et al.*[23] (blue) and Song *et al.*[16] (green).

4.3.2 Parameterization of the index of refraction

The timescale for diffusion into a sphere is a function of size, measured experimentally by Mie scattering. To use the geometric optics approximation, shown in equation (4.3), for calculating the droplet radius, the refractive index needs to be parameterized as a function of RH. Literature parameterizations for the concentration-dependent index of refraction for binary sucrose-water,[20] NaCl-water,[53,57] and $CaCl_2$-water[58] aqueous solutions are used for the ternary mixtures by applying the molar refractive mixing rule[59]

$$n_{eff} = \sum_i \phi_i n_i \tag{4.7}$$

in which ϕ_i is the mass fraction and n_i is the refractive index in the binary mixture and i are the solute components. The variation in the size of a droplet over the course of an experiment was < 0.15 μm (1σ) and we estimate a conservative absolute uncertainty of ~1%, ± 0.5 μm caused by uncertainty in the index of refraction mixing rules.

4.3.3 Diffusion of D_2O using Raman Spectroscopy

The chemical composition of the droplet evolving from containing H_2O to D_2O is determined using the change in the Raman spectrum as a function of time. The diffusion of D_2O into the droplet is analyzed using the difference in the Raman intensities for the features that arise from the H_2O and D_2O vibrations at ν(O-H) ~ 3400 cm^{-1} and ν(O-D) ~

2500 cm^{-1}. Since the total amount of sucrose is constant throughout each experiment all spectra are normalized to the sucrose ν(C-H) feature at 2900 cm^{-1}, allowing for correction of fluctuations in spectral intensity due to low amplitude motions of the droplet in the laser beam. The normalized spectra are fit using a sum of Gaussian peaks between 2000 – 3800 cm^{-1} to model the contribution of individual species and are used to calculate the intensity of H_2O and D_2O in the droplet as a function of time. When the droplet is initially equilibrated with a pure H_2O humidified atmosphere there is no contribution from the ν(O-D). As the chamber becomes increasingly concentrated in D_2O vapor the ν(O-H) is observed to decrease in intensity and the ν(O-D) peak grows in. At a constant relative humidity, the total amount of water in the droplet is assumed to be constant and equal to the sum of the contributions from H_2O and D_2O as described in our previous study of binary sucrose-H_2O aerosol.[47]

Shown in Figure 4.4 are example spectra for NaCl/sucrose (A) and $CaCl_2$/sucrose (B) droplets during an isotope exchange experiment modeled using a seven-term and eight-term Gaussian expansion fit, respectively. Up to two Gaussians contribute to the O-H band, two Gaussians to the C-H stretch, one Gaussian to the weak C-H shoulder peak, two Gaussians to the O-H band, and a weak, broad Gaussian accounts for background signal.

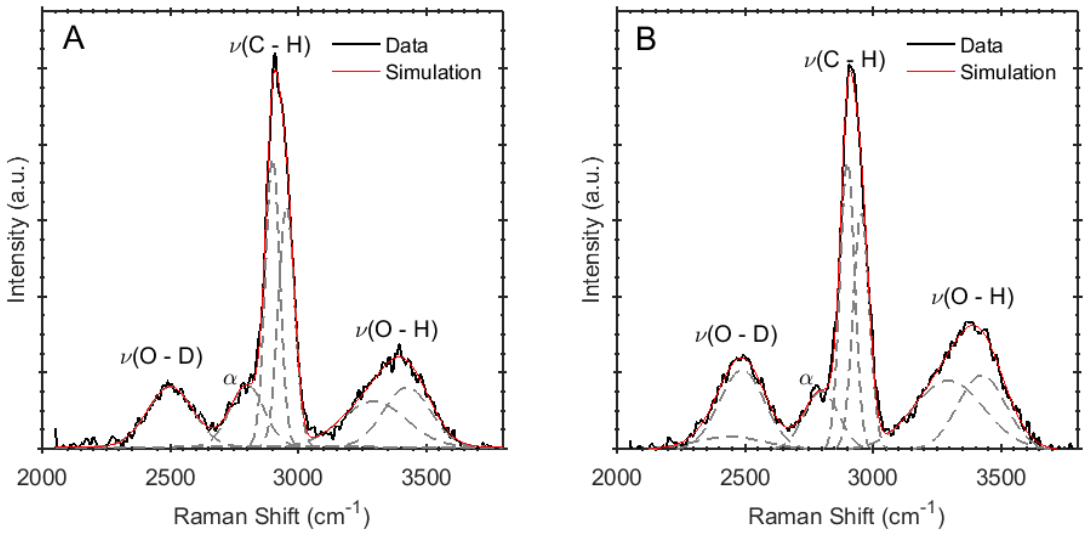

Figure 4.4. Raman spectra of a droplet undergoing isotope exchange for **A)** 1:1 NaCl-sucrose at 32% RH which is modeled using a summation of 7 Gaussians and **B)** 1:1 $CaCl_2$-sucrose at 31% RH which is modeled using a summation of 8 Gaussians.

The fractional concentration of D_2O in the droplet is calculated from the integrated intensity of the Gaussian fits for O-D and O-H peaks:

$$\phi_{\mathrm{OD}} = \frac{\mathrm{A_{OD}}}{\mathrm{A_{OD}} + \frac{1}{\sqrt{2}}\mathrm{A_{OH}}} \tag{4.8}$$

where the O-D stretch located at 2500 cm^{-1} has a lower integrated intensity by a factor of $1/\sqrt{2}$ based on the difference in reduced mass.[7] The solution to Fick's second law of diffusion applied to a sphere is used to model the time-dependent concentration, ϕ, of the diffusing D_2O:[45]

$$\phi_{OD} = 1 - \left(\frac{6}{\pi^2}\right)\sum_{n=1}^{\infty}\frac{1}{n^2}\exp\left(-\frac{n^2\pi^2 D_w t}{a^2}\right) \tag{4.9}$$

where a is the particle radius and D_w is the translational diffusion constant. A three-term expansion of equation (4.9) with a single adjustable parameter, $A = D_w/a^2$, is used to calculate D_w for each of the experimental runs at a different RH. The fractional concentration calculated a NaCl-sucrose droplet is shown in Figure 4.5 for (A) D_2O and (B) for H_2O as a function of time, modeled using equation (4.9) in green, with ±30 % estimated error in the adjustable A fit parameter indicated in shaded grey. The baseline at early times is when the droplet is initially equilibrated in H_2O RH for collection of reference Raman and Mie spectra prior to measurements of the translational diffusion.

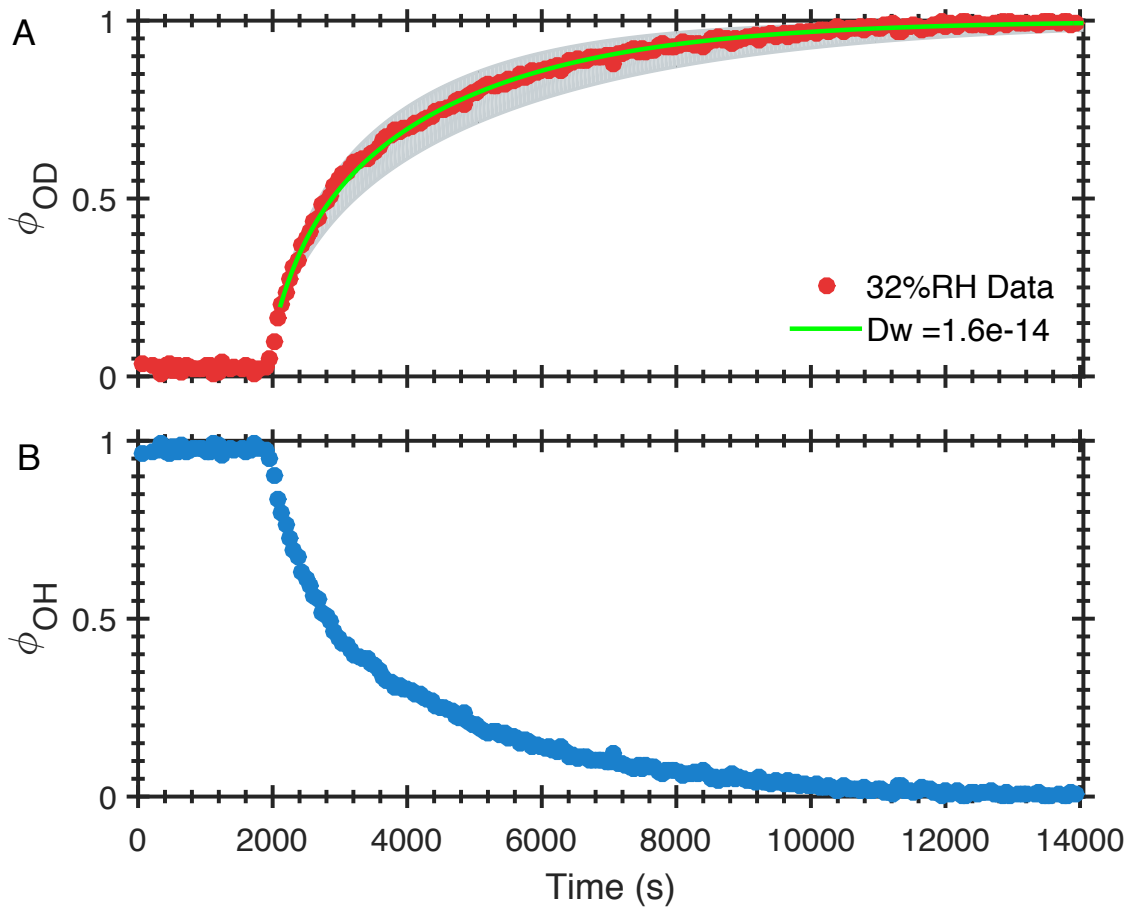

Figure 4.5. The fractional concentration of water in a 1:1 molar NaCl-sucrose droplet at 32% RH for (A) D_2O, the model in green, and the ±30% uncertainty in shaded grey, and of (B) H_2O over time.

When the gas manifold valves are rotated there is an unavoidable time delay until the chamber air has sufficiently turned over from H_2O and the D_2O partial pressure reaches a maximum. The approach for determining the time at which the chamber has sufficiently reached a constant gas-phase concentration of D_2O has been described

previously[47] and leads to an experimentally constrained upper limit of $2x10^{-13}$ m^2s^{-1} for the diffusion coefficients able to be studied using this method using the current apparatus.

4.3.4 NaCl-sucrose Ternary Mixture

The calculated water diffusion coefficients as a function of RH are shown in Figure 4.6. The data obtained in the current study are shown in red with error bars representing the uncertainty in the RH based on the probe manufacturer specifications (±1.5 %RH) and estimated ± 50% in the D_w based on the D_2O concentration fit and ±0.5 μm uncertainty in the size measurement from fluctuations during an the experiment and accuracy of the geometric optics approximation. Data are shown from this study (red squares) compared against the S-E predictions for the 1:1 NaCl-sucrose mixture using the Norrish and AIOMFAC sucrose MFS treatments (green dashed and purple dashed, respectively). Also shown for comparison are data from our previous study[47] on binary sucrose-water aerosol using this apparatus (grey circles), the sucrose Vignes fit (solid gray), and the S-E prediction of the sucrose based on the viscosity measurements of Grayson *et al.* (dashed grey). The Vignes-type fit (red) is described as:

$$D_w = (D^0_{w,w})^{x_w}\left(D^0_{w,s}\right)^{x_s} \tag{4.10}$$

where $D^0_{w,w}$ is the self diffusion of water equal to 2 x 10^{-9} m^2/s, $D^0_{w,s}$ is the diffusion of water in the limit of pure solute, and x_w and x_s are mole fractions of water and solute,

respectively. The solute in this case is the combination of NaCl and sucrose and a single value for $D^0_{w,s}$ = 1x10^{-22} m^2/s was found to best represent the 1:1 mixture data. The value for the combined $D^0_{w,s}$ has been previously suggested to be a linear relationship between the log($D^0_{w,s}$) of the individual components, here $D^0_{w,sucrose}$ and $D^0_{w,NaCl}$, and the mass fraction of the respective components.[18] While a similar analysis of the relationship between log($D^0_{w,s}$) and mass fraction of NaCl would require additional mixing ratios, our proposed value for the mixed-solute $D^0_{w,s}$ is five orders of magnitude greater than the literature value for the single solute component sucrose (1.9 x 10^{-27} m^2/s). The trend toward higher D_w with the addition of NaCl suggests the salt disrupts the strong hydrogen bonding network of concentrated sucrose molecules enabling water to have higher mobility. The hygroscopic properties of NaCl also lead to a higher concentration of water for a given RH compared to binary sucrose-water, leading to a lower viscosity based on the plasticizing effect of water, as seen by the higher D_w values compared to aqueous sucrose.

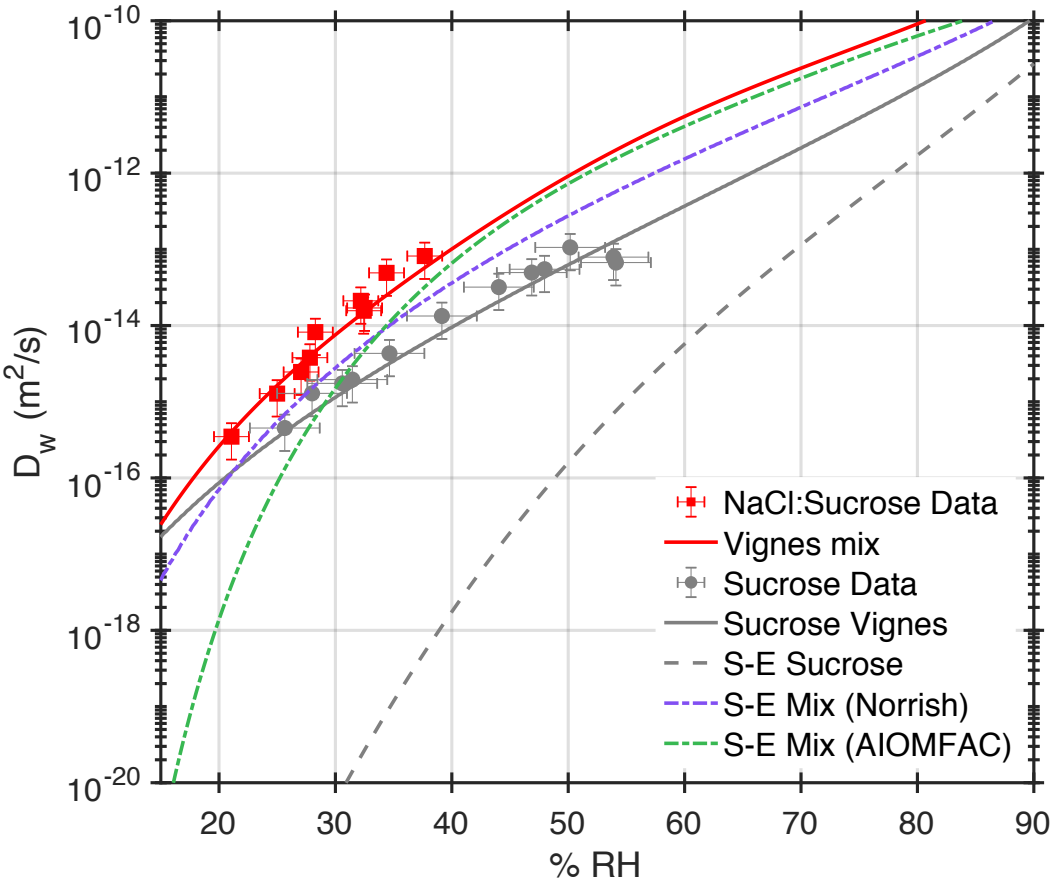

Figure 4.6. Relative humidity-dependent water diffusion coefficients for 1:1 molar NaCl-sucrose (red squares), and Vignes mixture fit (red), the S-E prediction for 1:1 mixture using the Norrish[28] treatment (purple dashed), and AIOMFAC[52] treatment (green dashed), compared with previous sucrose data[47] (grey circles), and sucrose Vignes fit[47] (grey solid), S-E prediction from Grayson *et al.*[23] viscosity data (grey dashed).

The comparison with the S-E relation shows better agreement for the 1:1 ternary NaCl-sucrose-H_2O mixture compared with the binary mixture, however the S-E prediction still lies more than an order of magnitude below the measurements. In the case of aqueous sucrose, the S-E relation underestimates the experimentally measured D_w

values by several orders of magnitude, even at the highest RH measured. This phenomenon has been reported for other chemical systems, suggesting the formation of dynamic heterogeneities caused by strong hydrogen-bonded networks and ability of small water molecules to diffuse through small volumes of the matrix.[37,45,60] It has been suggested in previous literature that the presence of ions in a concentrated sugar matrix also led to decoupling of diffusion and viscosity, where the ions show preference for solvation with water and can diffuse more easily through the water-rich domains.[60] In the context of comparisons with the single aerosol viscosity measurements of Power *et al.* reporting higher viscosity than predicted by models, the associated D_w values based on the S-E relation would be lower than the models shown in Figure 4.5. This would lead to a larger difference between the measurements and S-E predictions, highlighting the breakdown of the relation even for ternary systems and demonstrates the necessity of further direct diffusion measurements on a wider range of atmospherically-relevant chemical systems.

4.3.5 Ternary $CaCl_2$-sucrose ternary mixture

The results for the water diffusion coefficient as a function of RH in 1:1 molar ternary $CaCl_2$/sucrose single aerosol are shown in Figure 4.7. The data (red) are shown with an uncertainty of ± 50% and ±1.5 %RH as discussed for the NaCl-sucrose data. The results are fit with mass fraction-dependent Vignes fit similar to Section 4.3.4 where the solute is the combination of sucrose and $CaCl_2$, and shown with an S-shaped curve (black

dashed) to guide the eye for the sharp decrease in D_w. For comparison, the binary sucrose-water data[47] (grey circles), binary sucrose Vignes fit[45] (grey), and S-E sucrose predictions based on Grayson *et al.* data[23] (dashed grey) are shown. The measured diffusion coefficients in the ternary mixture are larger compared to binary aqueous sucrose values, which is again attributed to the increased hygroscopicity of the mixture and lowering of the viscosity due to greater water content.

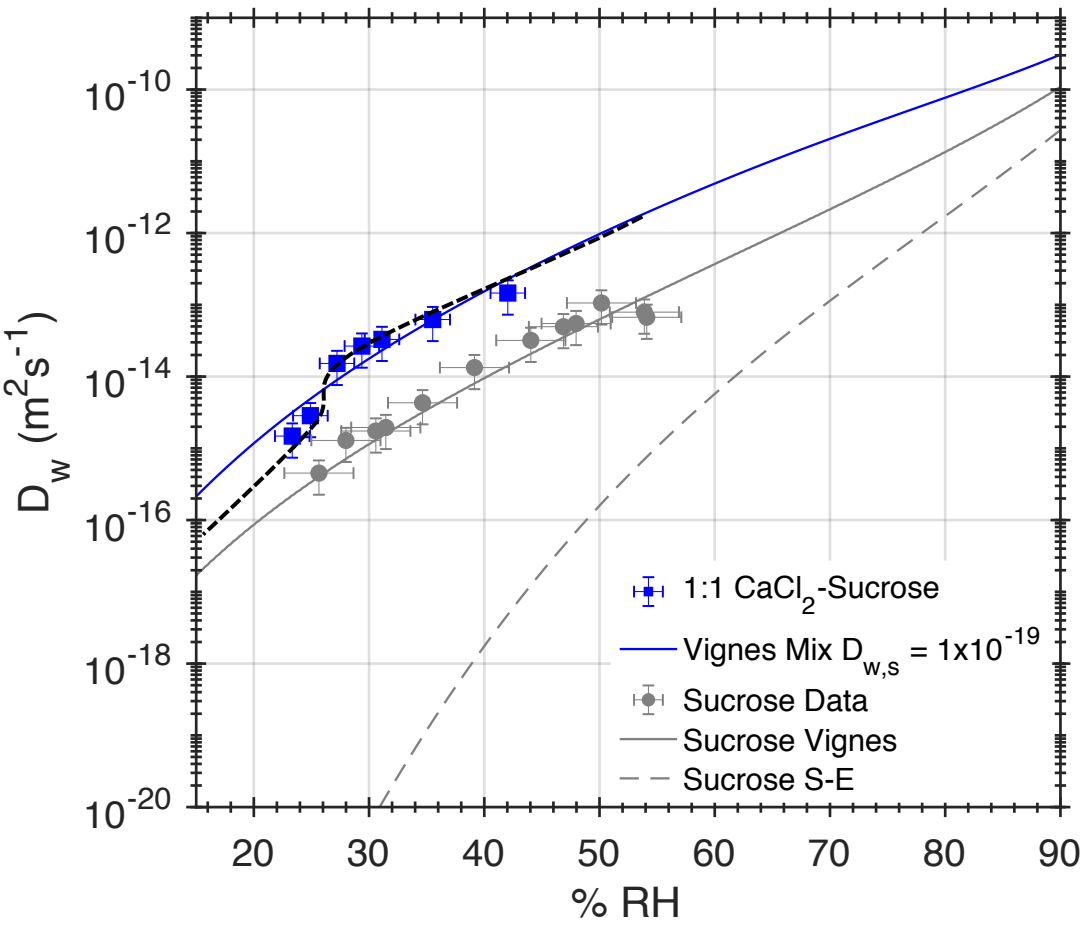

Figure 4.7. Water diffusion coefficients as a function of RH in 1:1 molar ternary $CaCl_2$-sucrose single aerosol (blue squares), mass fraction-based Vignes fit for the mixture (blue line) are shown with an S-curve (black dashed) to guide the eye, additionally shown for comparison with aqueous sucrose data[47] (grey circles), Vignes fit for sucrose[45] (grey), and S-E for sucrose[23] (dashed grey).

The data are modeled with Vignes-type fit as a function of the combined mass fraction of solute modeled from AIOMFAC as discussed in Section 4.3.1. The data give rise to an S-shape indicated by a steep decrease in D_w between 26-28% RH. The Vignes

fit is shown with an envelope of uncertainty, unlike the NaCl-sucrose data, because a single value does not adequately capture the S-shaped behavior apparent in the data. This behavior may be indicative of gel formation in the aerosol, although the effect is not as conclusive as previous literature showing a decrease in D_w over several orders of magnitude with RH in $MgSO_4$-water aerosol.[61] Calcium has been identified in marine-derived microgels[62] and is known to form gel structures in polysaccharides and proteins.[63,64] Calcium has also been demonstrated to interact with carbohydrates by binding to hydroxyl groups.[65] The S-shaped behavior at 26-28% RH indicates the onset of the formation of gel-like structures under high concentration conditions achieved at low RH. Gels have previously been modeled with percolation theory which assumes a mixture of media have distinct, different diffusion coefficients giving rise to a sharp decrease of the combined diffusion coefficient visualized in an S-shaped curve.[66] A physical model of the theory requires parameterizations of the volume fraction and packing fraction and is beyond the scope of this work. Additional studies examining the Ca^{2+} concentration dependence on water diffusion using a range of mixing ratios may reveal a stronger effect.

4.4 Conclusions

The concentration-dependent water diffusion coefficient in ternary mixtures of sucrose-NaCl-H_2O and sucrose-$CaCl_2$-H_2O in model aerosol were measured using isotope exchange in an electrodynamic balance for the first time. Mixed inorganic-

organic aerosol are prevalent in the atmosphere, particularly in marine environments, and understanding the physicochemical properties is crucial to understand their impacts on climate. Water diffusion measurements independent of viscosity are important for understanding when the Stokes-Einstein relation breaks down, and for improving the models used to predict the concentration and RH-dependent mobility of water in aerosol. There is a need to collect direct water diffusion measurements on model organic and mixed organic aerosol to better inform and improve models which incorporate diffusion for predicting aerosol growth, reaction kinetics, and phase state. We have shown that while the S-E relation underpredicts the water diffusion coefficient by many orders of magnitude in binary sucrose/water aerosol, the relation is in better agreement for the ternary sucrose-NaCl-H_2O mixture, suggesting that the hygroscopic NaCl component disproportionately impacts the water mobility compared to sucrose. While no viscosity data is currently available for the sucrose/$CaCl_2$/water system, the results indicate that the behavior of $CaCl_2$ can be described using a variation of percolation theory better than a single-solute diffusion coefficient in a Vignes-type parameterization. Future studies examining a range of molar ratios and additional carbohydrate systems can confirm this behavior.

The methodology of isotope tracing and Raman spectroscopy combined with an electrodynamic balance is a useful tool for studying the water diffusion coefficient in single, charged aerosols at controlled RH and temperature. The method has successfully been applied to ternary mixtures, allowing comparison to diffusion coefficients predicted using viscosity measurements and the Stokes-Einstein relation. Moreover, the method

enables a database of atmospherically-relevant binary and ternary chemical systems to be compiled, data which are currently severely lacking.[17] Expansion of a library of diffusion data will improve our understanding of how the physicochemical properties of aerosols, such as viscosity and chemical composition, impact climate-relevant water uptake and cloud activation behaviors.

Chapter 4, in part, is currently being prepared for publication of the material. Nadler, Katherine A.; Kim, Pyeongeun; Continetti, Robert E. The dissertation author was the primary investigator and author of this paper.

4.5 Supplementary Information

Supplementary Information accompanying "Water Diffusion Measurements of Ternary Mixtures in Single Charged Aerosol Using H_2O/D_2O Isotope Exchange"

Authors: Katherine A. Nadler, Pyeongeun Kim, [1] Robert E. Continetti[1]

[1]Department of Chemistry and Biochemistry, University of California San Diego

Contact: Robert E. Continetti, rcontinetti@ucsd.edu

4.5.1 Ternary 1:1 molar NaCl-sucrose-water mixture

All Raman spectra for ternary NaCl-sucrose-H_2O are fit between 2050 cm^{-1} – 4000 cm^{-1} using a 7-term Gaussian expansion of the form:

$$Fit = \sum_{i=1}^{7} aexp\left(-\frac{(b-x)^2}{c^2}\right) \quad \text{(S4.1)}$$

The area of the ν(O-D), α, ν (C-H), and ν (O-H) peaks are calculated by the following equations:

$$Area_{OD} = Area_{Peak2} \quad \text{(S4.2)}$$
$$Area_{\alpha} = Area_{Peak3} \quad \text{(S4.3)}$$
$$Area_{CH} = Area_{Peak4} + Area_{Peak5} \quad \text{(S4.4)}$$
$$Area_{OH} = Area_{Peak6} + Area_{Peak7} \quad \text{(S4.5)}$$

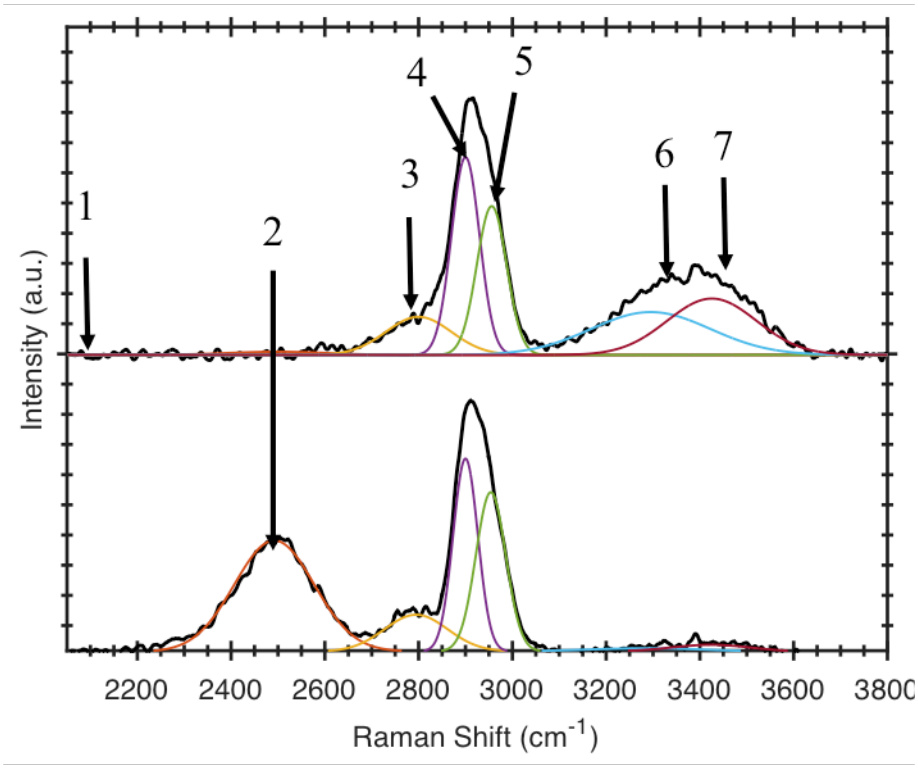

Figure 4.S1. Raman spectra of a 1:1 NaCl-sucrose droplet undergoing isotope exchange at 31% RH at early (top) and late (bottom) time points. The spectra are deconstructed into 7 Gaussians as described in the manuscript, which are shown here individually.

Table S4.1. Gaussian fit parameters for each of the 8 Gaussians in a single spectrum accompanying Figure S4.1 where *a*, *b,* and *c* follow Equation S4.6. The full dataset of fit parameters will be available in the Digital Collection.

Upper	Peak	a	b	c
	1	-0.004	2930.0	2000.0
	2	0.013	2500.0	150.0
	3	0.152	2800.0	99.1
	4	0.787	2900.0	42.4
	5	0.592	2955.9	45.0
	6	0.171	3295.0	180.0
	7	0.224	3425.4	134.7

Lower	Peak	a	b	c
	1	0.017	2915.0	2000.0
	2	0.442	2492.0	120.0
	3	0.146	2794.6	95.0
	4	0.767	2900.0	37.3
	5	0.633	2954.0	45.0
	6	0.013	3290.0	180.0
	7	0.027	3425.0	120.0

Data for the water diffusion coefficients in 1:1 molar NaCl-sucrose aerosols as a function of RH shown in Figure 4.6 in the main text were fit with a 3rd degree polynomial of the form:

$$D_w = a + b_1 RH + b_2 RH^2 + b_3 RH^3 \quad \text{(S4.6)}$$

Table 4.S2. Table of best-fit values for the 1:1 molar NaCl-sucrose mixture water diffusion coefficients.

a	b_1	b_2	b_3
-20.33	0.2847	-2.855E-03	1.17E-05

4.5.2 Ternary 1:1 molar $CaCl_2$-sucrose-water mixture

All Raman spectra for ternary $CaCl_2$-sucrose-H_2O are fit between 2050 cm^{-1} – 4000 cm^{-1} using a 8-term Gaussian expansion of the form:

$$Fit = \sum_{i=1}^{8} aexp\left(-\frac{(b-x)^2}{c^2}\right) \quad \text{(S4.7)}$$

The area of the ν(O-D), α, ν (C-H), and ν (O-H) peaks are calculated by the following equations:

$$Area_{OD} = Area_{Peak2} + Area_{Peak3} \quad \text{(S4.8)}$$
$$Area_{\alpha} = Area_{Peak4} \quad \text{(S4.9)}$$
$$Area_{CH} = Area_{Peak5} + Area_{Peak6} \quad \text{(S4.10)}$$
$$Area_{OH} = Area_{Peak7} + Area_{Peak8} \quad \text{(S4.11)}$$

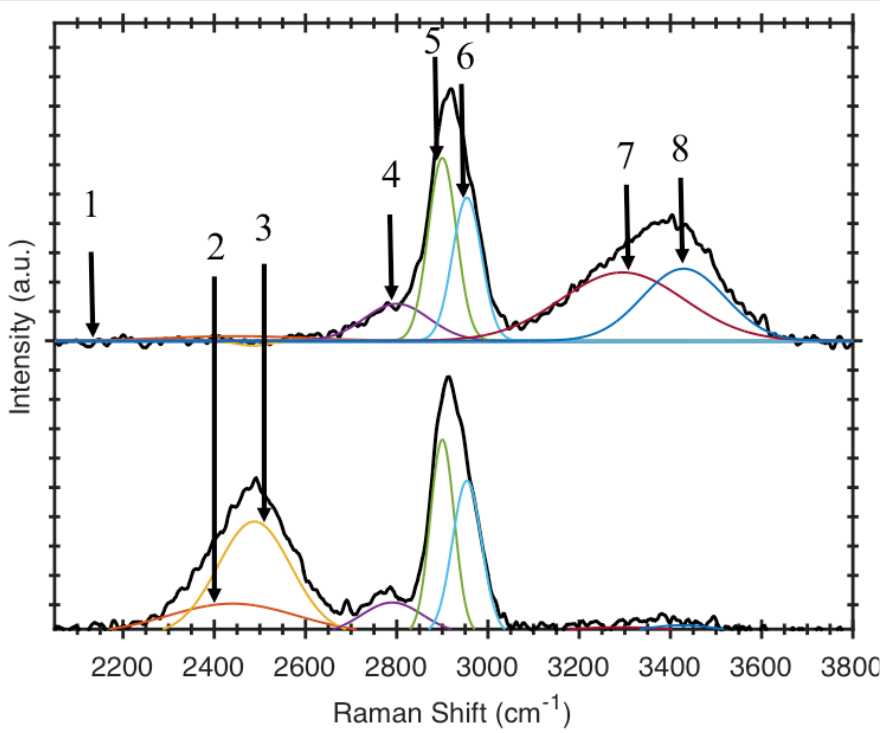

Figure 4.S2. Normalized Raman spectra of a 1:1 molar $CaCl_2$-sucrose droplet at 32% RH undergoing isotope exchange. The spectra is modeled with 8 Gaussian fits as shown.

Table 4.S3. Gaussian fit parameters for each of the 8 Gaussians in a single spectrum accompanying Figure S4.2 where *a*, *b,* and *c* follow Equation S4.7. The full dataset of fit parameters will be available in the Digital Collection.

Upper	Peak	a	b	c
	1	-0.005	2915.0	2000.0
	2	0.019	2450.0	220.0
	3	-0.020	2485.0	50.0
	4	0.151	2800.0	100.0
	5	0.748	2900.0	43.5
	6	0.585	2954.0	45.0
	7	0.280	3295.0	191.1
	8	0.295	0.0	128.5

Lower	Peak	a	b	c
	1	0.013	2930.0	2000.0
	2	0.125	2440.0	200.0
	3	0.460	2488.0	113.2
	4	0.129	2790.0	95.0
	5	0.796	2900.0	37.0
	6	0.627	2954.0	45.0
	7	0.028	3290.0	200.0
	8	0.036	3425.0	120.0

The water diffusion coefficient measurements in 1:1 molar $CaCl_2$-sucrose mixtures presented in Figure 4.7 in the main text were fit with a 2nd degree polynomial of the form:

$$D_w = a + b_1 RH + b_2 RH^3 \quad \text{(S4.12)}$$

Table S4.4. Table of best-fit values for the 1:1 molar $CaCl_2$-sucrose mixture water diffusion coefficients.

a	b_1	b_2
-9.83E-06	1.60E-03	-15.08

4.5 References

(1) Lee, L. A.; Pringle, K. J.; Reddington, C. L.; Mann, G. W.; Stier, P.; Spracklen, D. V.; Pierce, J. R.; Carslaw, K. S. The Magnitude and Causes of Uncertainty in Global Model Simulations of Cloud Condensation Nuclei. *Atmos. Chem. Phys.* **2013**, *13* (17), 8879–8914.

(2) Lienhard, D. M.; Huisman, A. J.; Krieger, U. K.; Rudich, Y.; Marcolli, C.; Luo, B. P.; Bones, D. L.; Reid, J. P.; Lambe, A. T.; Canagaratna, M. R.; et al. Viscous Organic Aerosol Particles in the Upper Troposphere: Diffusivity-Controlled Water Uptake and Ice Nucleation? *Atmos. Chem. Phys.* **2015**, *15* (23), 13599–13613.

(3) Lu, J. W.; Rickards, A. M. J.; Walker, J. S.; Knox, K. J.; Miles, R. E. H.; Reid, J. P.; Signorell, R. Timescales of Water Transport in Viscous Aerosol: Measurements on Sub-Micron Particles and Dependence on Conditioning History. *Phys. Chem. Chem. Phys.* **2014**, *16* (21), 9819–9830.

(4) Cochran, R. E.; Laskina, O.; Trueblood, J. V.; Estillore, A. D.; Morris, H. S.; Jayarathne, T.; Sultana, C. M.; Lee, C.; Lin, P.; Laskin, J.; et al. Molecular Diversity of Sea Spray Aerosol Particles: Impact of Ocean Biology on Particle Composition and Hygroscopicity. *Chem* **2017**, *2* (5), 655–667.

(5) Cochran, R. E.; Laskina, O.; Jayarathne, T.; Laskin, A.; Laskin, J.; Lin, P.; Sultana, C.; Lee, C.; Moore, K. A.; Cappa, C. D.; et al. Analysis of Organic Anionic Surfactants in Fine and Coarse Fractions of Freshly Emitted Sea Spray Aerosol. *Environ. Sci. Technol.* **2016**, *50* (5), 2477–2486.

(6) Cochran, R. E.; Jayarathne, T.; Stone, E. A.; Grassian, V. H. Selectivity Across the Interface: A Test of Surface Activity in the Composition of Organic-Enriched Aerosols from Bubble Bursting. *J. Phys. Chem. Lett.* **2016**, *7* (9), 1692–1696.

(7) Zobrist, B.; Marcolli, C.; Pedernera, D. A.; Koop, T. Do Atmospheric Aerosols Form Glasses? *Atmos. Chem. Phys.* **2008**, *8* (17), 5221–5244.

(8) Orellana, M. V; Matrai, P. A.; Leck, C.; Rauschenberg, C. D.; Lee, A. M.; Coz, E. Marine Microgels as a Source of Cloud Condensation Nuclei in the High Arctic. *Proc. Natl. Acad. Sci. U. S. A.* **2011**, *108* (33), 13612–13617.

(9) Virtanen, A.; Joutsensaari, J.; Koop, T.; Kannosto, J.; Yli-Pirila, P.; Leskinen, J.; Makela, J. M.; Holopainen, J. K.; Poschl, U.; Kulmala, M.; et al. An Amorphous Solid State of Biogenic Secondary Organic Aerosol Particles. *Nature* **2010**, *467* (7317), 824–827.

(10) Jarvinen, E.; Ignatius, K.; Nichman, L.; Kristensen, T. B.; Fuchs, C.; Hoyle, C. R.; Hoppel, N.; Corbin, J. C.; Craven, J.; Duplissy, J.; et al. Observation of Viscosity Transition in Alpha-Pinene Secondary Organic Aerosol. *Atmos. Chem. Phys.* **2016**, *16* (7), 4423–4438.

(11) Shiraiwa, M.; Seinfeld, J. H. Equilibration Timescale of Atmospheric Secondary Organic Aerosol Partitioning. *Geophys. Res. Lett.* **2012**, *39* (24), L24801.

(12) Bateman, A. P.; Belassein, H.; Martin, S. T. Impactor Apparatus for the Study of Particle Rebound: Relative Humidity and Capillary Forces. *Aerosol Sci. Technol.* **2014**, *48* (1), 42–52.

(13) Grayson, J. W.; Song, M.; Sellier, M.; Bertram, A. K. Validation of the Poke-Flow Technique Combined with Simulations of Fluid Flow for Determining Viscosities in Samples with Small Volumes and High Viscosities. *Atmos. Meas. Tech.* **2015**, *8* (6), 2463–2472.

(14) Bones, D. L.; Reid, J. P.; Lienhard, D. M.; Krieger, U. K. Comparing the Mechanism of Water Condensation and Evaporation in Glassy Aerosol. *Proc. Natl. Acad. Sci. U. S. A.* **2012**, *109* (29), 11613–11618.

(15) Renbaum-Wolff, L.; Grayson, J. W.; Bertram, A. K. Technical Note: New Methodology for Measuring Viscosities in Small Volumes Characteristic of Environmental Chamber Particle Samples. *Atmos. Chem. Phys.* **2013**, *13* (2), 791–802.

(16) Song, Y. C.; Haddrell, A. E.; Bzdek, B. R.; Reid, J. P.; Bannan, T.; Topping, D. O.; Percival, C.; Cai, C. Measurements and Predictions of Binary Component Aerosol Particle Viscosity. *J. Phys. Chem. A* **2016**, *120* (41), 8123–8137.

(17) Reid, J. P.; Bertram, A. K.; Topping, D. O.; Laskin, A.; Martin, S. T.; Petters, M. D.; Pope, F. D.; Rovelli, G. The Viscosity of Atmospherically Relevant Organic Particles. *Nat. Commun.* **2018**, *9* (1), 956.

(18) Davies, J. F.; Wilson, K. R. Nanoscale Interfacial Gradients Formed by the Reactive Uptake of OH Radicals onto Viscous Aerosol Surfaces. *Chem. Sci.* **2015**, *6* (12), 7020–7027.

(19) Liu, P. F.; Li, Y. J.; Wang, Y.; Bateman, A. P.; Zhang, Y.; Gong, Z. H.; Bertram, A. K.; Martin, S. T. Highly Viscous States Affect the Browning of Atmospheric Organic Particulate Matter. *Acs Cent. Sci.* **2018**, *4* (2), 207–215.

(20) Tong, H. J.; Reid, J. P.; Bones, D. L.; Luo, B. P.; Krieger, U. K. Measurements of the Timescales for the Mass Transfer of Water in Glassy Aerosol at Low Relative

Humidity and Ambient Temperature. *Atmos. Chem. Phys.* **2011**, *11* (10), 4739–4754.

(21) Lienhard, D. M.; Huisman, A. J.; Krieger, U. K.; Rudich, Y.; Marcolli, C.; Luo, B. P.; Bones, D. L.; Reid, J. P.; Lambe, A. T.; Canagaratna, M. R.; et al. Viscous Organic Aerosol Particles in the Upper Troposphere: Diffusivity-Controlled Water Uptake and Ice Nucleation? *Atmos. Chem. Phys.* **2015**, *15* (23), 13599–13613.

(22) Ignatius, K.; Kristensen, T. B.; Jarvinen, E.; Nichman, L.; Fuchs, C.; Gordon, H.; Herenz, P.; Hoyle, C. R.; Duplissy, J.; Garimella, S.; et al. Heterogeneous Ice Nucleation of Viscous Secondary Organic Aerosol Produced from Ozonolysis of Alpha-Pinene. *Atmos. Chem. Phys.* **2016**, *16* (10), 6495–6509.

(23) Grayson, J. W.; Evoy, E.; Song, M.; Chu, Y.; Maclean, A.; Nguyen, A.; Upshur, M. A.; Ebrahimi, M.; Chan, C. K.; Geiger, F. M.; et al. The Effect of Hydroxyl Functional Groups and Molar Mass on the Viscosity of Non-Crystalline Organic and Organic–Water Particles. *Atmos. Chem. Phys.* **2017**, *17* (13), 8509–8524.

(24) Power, R. M.; Simpson, S. H.; Reid, J. P.; Hudson, A. J. The Transition from Liquid to Solid-like Behaviour in Ultrahigh Viscosity Aerosol Particles. *Chem. Sci.* **2013**, *4* (6), 2597–2604.

(25) Rothfuss, N. E.; Petters, M. D. Influence of Functional Groups on the Viscosity of Organic Aerosol. *Environ. Sci. Technol.* **2017**, *51* (1), 271–279.

(26) Marsh, A.; Petters, S. S.; Rothfuss, N. E.; Rovelli, G.; Song, Y. C.; Reid, J. P.; Petters, M. D. Amorphous Phase State Diagrams and Viscosity of Ternary Aqueous Organic/Organic and Inorganic/Organic Mixtures. *Phys. Chem. Chem. Phys.* **2018**, *20* (22), 15086–15097.

(27) Chenlo, F.; Moreira, R.; Pereira, G.; Ampudia, A. Viscosities of Aqueous Solutions of Sucrose and Sodium Chloride of Interest in Osmotic Dehydration Processes. *J. Food Eng.* **2002**, *54* (4), 347–352.

(28) Norrish, R. S. An Equation for the Activity Coefficients and Equilibrium Relative Humidities of Water in Confectionery Syrups. *J. Food Sci. Technol.* **1966**, *1*, 25–39.

(29) Topping, D. O.; McFiggans, G. B.; Coe, H. A Curved Multi-Component Aerosol Hygroscopicity Model Framework: Part 1 - Inorganic Compounds. *Atmos. Chem. Phys.* **2005**, *5*, 1205–1222.

(30) Topping, D. O.; McFiggans, G. B.; Coe, H. A Curved Multi-Component Aerosol Hygroscopicity Model Framework: Part 2 - Including Organic Compounds. *Atmos.*

Chem. Phys. **2005**, *5*, 1223–1242.

(31) Stokes, R. H.; Robinson, R. A. Interactions in Aqueous Nonelectroylte Solutions I. Solute-Solvent Equilibria. *J. Phys. Chem.* **1966**, *70* (7), 2126-.

(32) Rothfuss, N. E.; Marsh, A.; Rovelli, G.; Petters, M. D.; Reid, J. P. Condensation Kinetics of Water on Amorphous Aerosol Particles. *J. Phys. Chem. Lett.* **2018**, *9* (13), 3708–3713.

(33) Marshall, F. H.; Miles, R. E. H.; Song, Y.-C.; Ohm, P. B.; Power, R. M.; Reid, J. P.; Dutcher, C. S. Diffusion and Reactivity in Ultraviscous Aerosol and the Correlation with Particle Viscosity. *Chem. Sci.* **2016**, *7* (2), 1298–1308.

(34) Mikhailov, E.; Vlasenko, S.; Martin, S. T.; Koop, T.; Pöschl, U. Amorphous and Crystalline Aerosol Particles Interacting with Water Vapor: Conceptual Framework and Experimental Evidence for Restructuring, Phase Transitions and Kinetic Limitations. *Atmos. Chem. Phys.* **2009**, *9* (24), 9491–9522.

(35) Price, H. C.; Mattsson, J.; Murray, B. J. Sucrose Diffusion in Aqueous Solution. *Phys. Chem. Chem. Phys.* **2016**, *18* (28), 19207–19216.

(36) Kumar, S. K.; Szamel, G.; Douglas, J. F. Nature of the Breakdown in the Stokes-Einstein Relationship in a Hard Sphere Fluid. *J. Chem. Phys.* **2006**, *124* (21), 214501.

(37) Molinero, V.; Goddard, W. A. Microscopic Mechanism of Water Diffusion in Glucose Glasses. *Phys. Rev. Lett.* **2005**, *95* (4), 045701.

(38) Zobrist, B.; Soonsin, V.; Luo, B. P.; Krieger, U. K.; Marcolli, C.; Peter, T.; Koop, T. Ultra-Slow Water Diffusion in Aqueous Sucrose Glasses. *Phys. Chem. Chem. Phys.* **2011**, *13* (8), 3514–3526.

(39) Lienhard, D. M.; Huisman, A. J.; Bones, D. L.; Te, Y. F.; Luo, B. P.; Krieger, U. K.; Reid, J. P. Retrieving the Translational Diffusion Coefficient of Water from Experiments on Single Levitated Aerosol Droplets. *Phys. Chem. Chem. Phys.* **2014**, *16* (31), 16677–16683.

(40) Lienhard, D. M.; Huisman, A. J.; Krieger, U. K.; Rudich, Y.; Marcolli, C.; Luo, B. P.; Bones, D. L.; Reid, J. P.; Lambe, A. T.; Canagaratna, M. R.; et al. Viscous Organic Aerosol Particles in the Upper Troposphere: Diffusivity-Controlled Water Uptake and Ice Nucleation? *Atmos. Chem. Phys.* **2015**, *15* (23), 13599–13613.

(41) Rickards, A. M. J.; Song, Y. C.; Miles, R. E. H.; Preston, T. C.; Reid, J. P. Variabilities and Uncertainties in Characterising Water Transport Kinetics in

Glassy and Ultraviscous Aerosol. *Phys. Chem. Chem. Phys.* **2015**, *17* (15), 10059–10073.

(42) Marshall, F. H.; Miles, R. E. H.; Song, Y. C.; Ohm, P. B.; Power, R. M.; Reid, J. P.; Dutcher, C. S. Diffusion and Reactivity in Ultraviscous Aerosol and the Correlation with Particle Viscosity. *Chem. Sci.* **2016**, *7* (2), 1298–1308.

(43) Zhu, L.; Cai, T.; Huang, J.; Stringfellow, T. C.; Wall, M.; Yu, L. Water Self-Diffusion in Glassy and Liquid Maltose Measured by Raman Microscopy and NMR. *J. Phys. Chem. B* **2011**, *115* (19), 5849–5855.

(44) Price, H. C.; Murray, B. J.; Mattsson, J.; O'Sullivan, D.; Wilson, T. W.; Baustian, K. J.; Benning, L. G. Quantifying Water Diffusion in High-Viscosity and Glassy Aqueous Solutions Using a Raman Isotope Tracer Method. *Atmos. Chem. Phys.* **2014**, *14* (8), 3817–3830.

(45) Davies, J. F.; Wilson, K. R. Raman Spectroscopy of Isotopic Water Diffusion in Ultraviscous, Glassy, and Gel States in Aerosol by Use of Optical Tweezers. *Anal. Chem.* **2016**, *88* (4), 2361–2366.

(46) Vignes, A. Diffusion in Binary Solutions - Variation of Diffusion Coefficient with Composition. *Ind. Eng. Chem. Fundam.* **1966**, *5* (2), 189–199.

(47) Nadler, K. A.; Huang, D.-L.; Kim, P.; Xiong, W.; Continetti, R. E. Water Diffusion Measurements of Single Charged Aerosol Using H2O/D2O Isotope Exchange and Raman Spectroscopy in an Electrodynamic Balance. *Phys. Chem. Chem. Phys.* **2018**, *Submitted.*

(48) Salomon, M. *Thermodynamic Properties of Liquid H2O and D2O and Their Mixtures*; United States. National Aeronautics and Space Administration. "NASA Technical Note." Print.: Washington, D.C., 1969.

(49) Ray, A. K.; Souyri, A.; Davis, E. J.; Allen, T. M. Precision of Light-Scattering Techniques for Measuring Optical-Parameters of Microspheres. *Appl. Opt.* **1991**, *30* (27), 3974–3983.

(50) Glantschnig, W. J.; Chen, S. H. Light-Scattering From Water Droplets in the Geometrical-Optics Approximation. *Appl. Opt.* **1981**, *20* (14), 2499–2509.

(51) Zuend, A.; Marcolli, C.; Luo, B. P.; Peter, T. A Thermodynamic Model of Mixed Organic-Inorganic Aerosols to Predict Activity Coefficients. *Atmos. Chem. Phys.* **2008**, *8* (16), 4559–4593.

(52) Zuend, A.; Marcolli, C.; Booth, A. M.; Lienhard, D. M.; Soonsin, V.; Krieger, U.

K.; Topping, D. O.; McFiggans, G.; Peter, T.; Seinfeld, J. H. New and Extended Parameterization of the Thermodynamic Model AIOMFAC: Calculation of Activity Coefficients for Organic-Inorganic Mixtures Containing Carboxyl, Hydroxyl, Carbonyl, Ether, Ester, Alkenyl, Alkyl, and Aromatic Functional Groups. *Atmos. Chem. Phys.* **2011**, *11* (17), 9155–9206.

(53) Tang, I. N. Thermodynamic and Optical Properties of Mixed-Salt Aerosols of Atmospheric Importance. *J. Geophys. Res.* **1997**, *102* (D2), 1883–1893.

(54) Rickards, A. M. J.; Song, Y.-C.; Miles, R. E. H.; Preston, T. C.; Reid, J. P. Variabilities and Uncertainties in Characterising Water Transport Kinetics in Glassy and Ultraviscous Aerosol. *Phys. Chem. Chem. Phys.* **2015**, *17* (15), 10059–10073.

(55) Starzak, M.; Peacock, S. D. Water Activity Coefficient in Aqueous Solutions of Sucrose - A Comprehensive Data Analysis. *Zuckerindustrie* **1997**, *122* (5), 380–387.

(56) Quintas, M.; Brandão, T. R. S.; Silva, C. L. M.; Cunha, R. L. Rheology of Supersaturated Sucrose Solutions. *J. Food Eng.* **2006**, *77* (4), 844–852.

(57) Tan, C. Y.; Huang, Y. X. Dependence of Refractive Index on Concentration and Temperature in Electrolyte Solution, Polar Solution, Nonpolar Solution, and Protein Solution. *J. Chem. Eng. Data* **2015**, *60* (10), 2827–2833.

(58) Tan, C.-Y.; Huang, Y.-X. Dependence of Refractive Index on Concentration and Temperature in Electrolyte Solution, Polar Solution, Nonpolar Solution, and Protein Solution. *J. Chem. Eng. Data* **2015**, *60*, 30.

(59) Cai, C.; Miles, R. E. H.; Cotterell, M. I.; Marsh, A.; Rovelli, G.; Rickards, A. M. J.; Zhang, Y. H.; Reid, J. P. Comparison of Methods for Predicting the Compositional Dependence of the Density and Refractive Index of Organic-Aqueous Aerosols. *J. Phys. Chem. A* **2016**, *120* (33), 6604–6617.

(60) Corti, H. R.; Frank, G. A.; Marconi, M. C. Diffusion−Viscosity Decoupling in Supercooled Aqueous Trehalose Solutions. *J. Phys. Chem. B* **2008**, *112* (41), 12899–12906.

(61) Price, H. C.; Mattsson, J.; Zhang, Y.; Bertram, A. K.; Davies, J. F.; Grayson, J. W.; Martin, S. T.; O'Sullivan, D.; Reid, J. P.; Rickards, A. M. J.; et al. Water Diffusion in Atmospherically Relevant α-Pinene Secondary Organic Material. *Chem. Sci.* **2015**, *6* (8), 4876–4883.

(62) Chin, W.-C.; Orellana, M. V.; Verdugo, P. Spontaneous Assembly of Marine

Dissolved Organic Matter into Polymer Gels. *Nature* **1998**, *391* (6667), 568–572.

(63) Verdugo, P. Polymer Gel Phase Transition in Condensation-Decondensation of Secretory Products. In *Responsive Gels: Volume Transitions II*; Springer-Verlag: Berlin/Heidelberg, 1993; pp 145–156.

(64) Ching, S. H.; Bhandari, B.; Webb, R.; Bansal, N. Visualizing the Interaction between Sodium Caseinate and Calcium Alginate Microgel Particles. *Food Hydrocoll.* **2015**, *43*, 165–171.

(65) Bugg, C. E. Calcium Binding to Carbohydrates. Crystal Structure of a Hydrated Calcium Bromide Complex of Lactose. *J. Am. Chem. Soc.* **1973**, *95* (3), 908–913.

(66) Murata, T.; Lee, M. S.; Tanioka, A. An Application of Percolation Theory to the Electrolyte Penetration through Porous Water-Swollen Cellulose Triacetate Membrane. *J. Colloid Interface Sci.* **1999**, *220* (2), 250–254.

Appendix A

A.1 Tabulated data of diffusion measurements

Experiments described in Chapter 3 and 4 measure the water diffusion coefficient in in single, charged aerosol composed of binary and ternary mixtures using isotope exchange and Raman spectroscopy in an electrodynamic balance at room temperature.

Table A.1 Experimental values for single sucrose-water diffusion measurements reported in Figure 3.4.

% RH	± %RH	T (°C)	r (m)	A	D_w (m^2/s)	± D_w (m^2/s)
25.7	2	23.1	1.95E-05	1.17E-05	4.5E-16	2.3E-16
28.0	2	22.9	1.86E-05	3.68E-05	1.3E-15	6.4E-16
30.6	2	23.5	1.94E-05	4.59E-05	1.7E-15	8.7E-16
31.5	2	22.4	2.02E-05	4.70E-05	2.0E-15	9.8E-16
34.6	2	21.6	2.26E-05	8.36E-05	4.3E-15	2.2E-15
39.1	2	21.1	2.60E-05	1.95E-04	1.3E-14	6.7E-15
44.0	2	22.3	2.71E-05	4.30E-04	3.2E-14	1.6E-14
46.9	2	22.4	1.98E-05	1.25E-03	5.0E-14	2.5E-14
48.0	2	20.3	2.69E-05	7.46E-04	5.5E-14	2.7E-14
50.2	2	23.5	2.81E-05	1.33E-03	1.1E-13	5.3E-14
53.9	2	22.4	2.37E-05	1.39E-03	7.9E-14	4.0E-14
54.1	2	23.0	2.38E-05	1.17E-03	6.7E-14	3.4E-14

Table A.2. Tabulated data from Figure 4.4 of 1:1 molar NaCl/sucrose water diffusion measurements.

% RH	± %RH	T (°C)	r (m)	A	D_w (m^2/s)	± D_w (m^2/s)
21.1	1.5	23.3	2.41E-05	5.90E-06	3.5E-16	1.7E-16
25.0	1.5	23.2	2.50E-05	2.02E-05	1.3E-15	6.4E-16
27.0	1.5	23.6	2.51E-05	3.85E-05	2.5E-15	1.2E-15
27.8	1.5	22.5	2.18E-05	7.86E-05	3.8E-15	1.9E-15
28.3	1.5	24.3	2.02E-05	1.99E-04	8.2E-15	4.1E-15
32.2	1.5	24	2.63E-05	3.01E-04	2.1E-14	1.1E-14
32.4	1.5	22.6	2.03E-05	3.74E-04	1.6E-14	7.8E-15
32.5	1.5	24.1	2.53E-05	2.62E-04	1.7E-14	8.5E-15
34.4	1.5	22.9	2.09E-05	1.11E-03	4.9E-14	2.5E-14
37.7	1.5	24.1	2.21E-05	1.65E-03	8.2E-14	4.1E-14

Table A.3. Tabulated data from Figure 4.7 of 1:1 molar $CaCl_2$/sucrose water diffusion measurements.

% RH	± %RH	T (°C)	r (m)	A	D_w (m^2/s)	± D_w (m^2/s)
23.3	23.4	1.5	2.51E-05	1.51E-15	1.5E-15	2.32E-05
24.9	23.5	1.5	2.82E-05	2.91E-15	2.9E-15	3.53E-05
27.2	23.1	1.5	3.66E-05	1.55E-14	1.5E-14	1.12E-04
29.4	24.4	1.5	2.46E-05	2.71E-14	2.7E-14	4.34E-04
31.1	23.4	1.5	2.51E-05	3.35E-14	3.3E-14	5.15E-04
35.5	22.8	1.5	2.73E-05	6.34E-14	6.2E-14	8.27E-04
42.0	22.7	1.5	2.97E-05	1.48E-13	1.5E-13	1.64E-03

A.2 LabView Data Acquisition (DAQ) Programs

The instrument description found in Chapter 2 describes the application of custom LabView software for communicating with an assortment of CCD detectors, instruments, and sensors. The user interface panels for controlling the EDB apparatus are described in Figures A.2.1 and A.2.2.

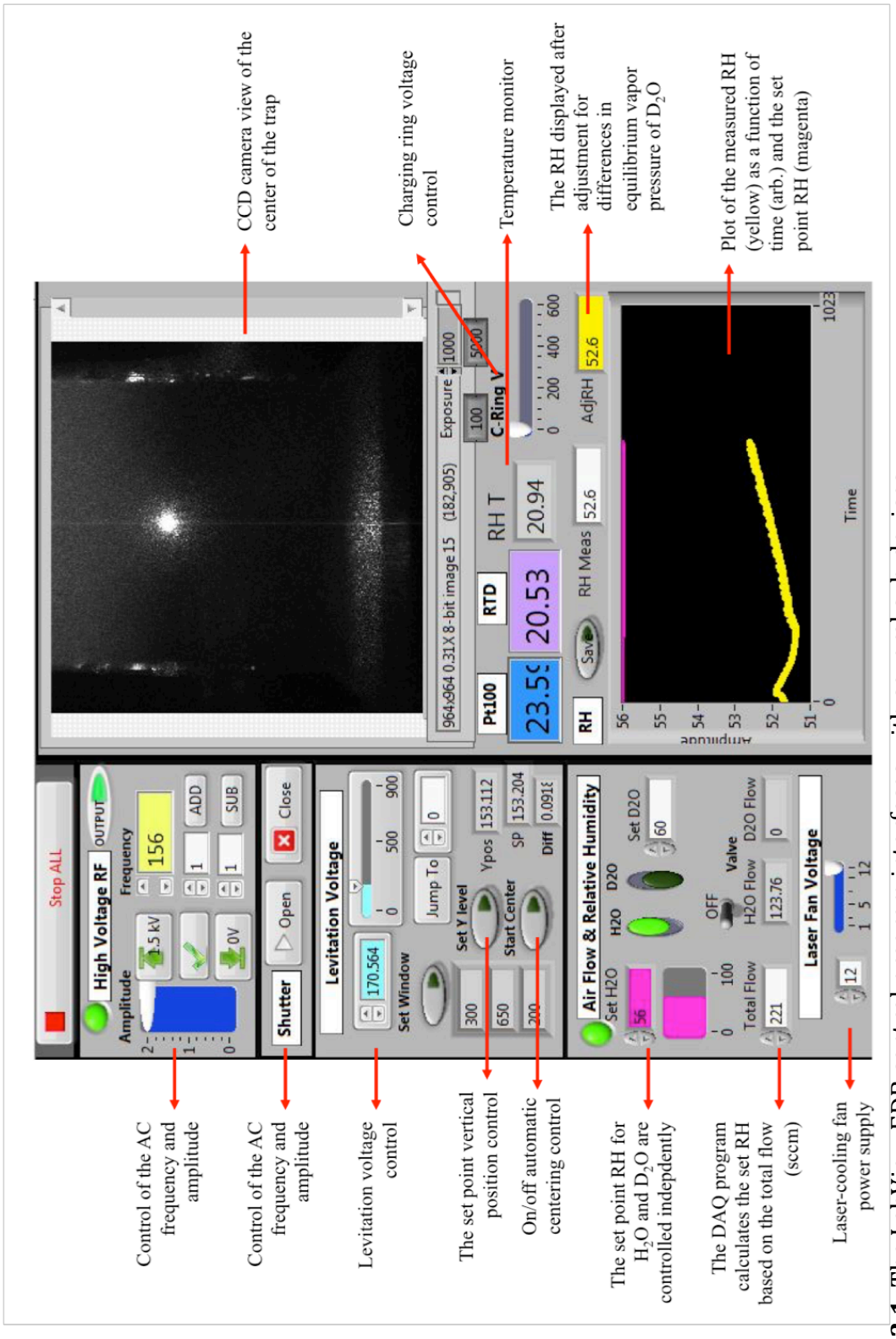

Figure A.2.1. The LabView EDB control program interfaces with several sub-devices.

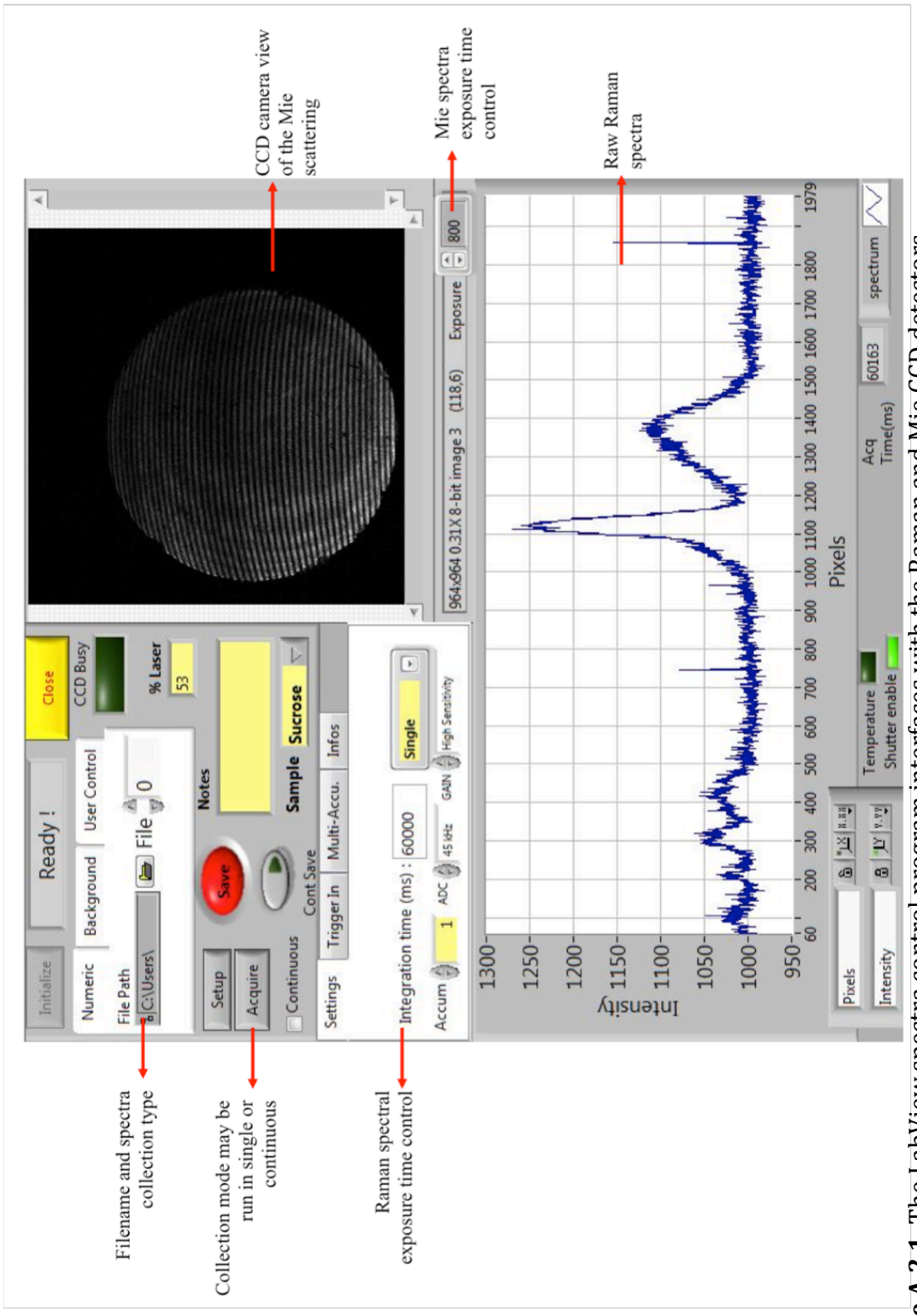

Figure A.2.1. The LabView spectra control program interfaces with the Raman and Mie CCD detectors.